Study on Inductively Coupled Sine-Gordon Equations as a Model for Intrinsic Josephson Junctions toward Terahertz Electromagnetic Radiation

Liu Feng

June 2015

Study on Inductively Coupled Sine-Gordon Equations as a Model for Intrinsic Josephson Junctions toward Terahertz Electromagnetic Radiation

Liu Feng

Doctoral Program in Materials Science and Engineering

Submitted to the Graduate School of
Pure and Applied Sciences
in Partial Fulfillment of the Requirements
for the Degree of Doctor of Philosophy in
Engineering

at the
University of Tsukuba

Table of Contents

List of Figures

Symbols list

Ψ: macroscopic superconductivity wave function
φ: phase of superconductivity
γ: gauge invariant phase difference
γ_l: gauge invariant phase difference at *l*-th insulating layer
$\mathbf{B}$: magnetic field
B^y_{sl}: magnetic field at *l*-th superconducting layer in a stack of IJJs
B^y_l: magnetic field at *l*-th insulating layer in a stack of IJJs
E: electric field
E^z_l: electric field at *l*-th insulating layer
H_{sl}: energy density stored in *l*-th superconducting layer
H_{bl}: energy density stored in *l*-th insulating layer
ε_c: dielectric constant of the insulating layer
λ: London penetration depth
λ_J: Josephson penetration depth
$\bar{c}$: Swihart velocity
Z: surface impedance of a Josephson junctions stack
ϕ: phase of the plasma oscillation
ω_J: Josephson plasma frequency
$\mathbf{A}$: vector potential
J_s: supercurrent
Φ_0: flux quanta
Δ: Laplace operator along lateral directions
λ_{ab}: London penetration depth along the c axis
λ_c: Lodon penetration depth along the *ab* plane
s: thickness of superconducting layer in the superconductor/insulator/supercondutor model
d: thickness of insulating layer in the superconductor/insulator/superconductor model
ζ: inductive coupling constant

β: normalized conductance along c axis

V: voltage

J_c: critical current density

$L(L_x, L_y)$: length of the Josephson junction or length of junction in the x/y direction

ω: angular frequency of the Josephson plasma oscillation

γ_l^s: static phase term

J_m: m-th Bessel function

H_m: m-th Hankel function

T_c: critical temperature

Q: quality factor

P_{dis}: ohmic dissipation power per unit length due to plasma oscillation

P_r: radiation power per unit length

I_c: critical current

S: area of cylindrical crystal

σ: standard deviation of Gaussian distribution

1 Introduction

Generation of electromagnetic (EM) waves is considered as one of the most highly developed scientific and technological fields and their applications are ubiquitous in our daily life, for example one uses microwaves for long-distance communication and employs x-rays for medical imaging. In this thesis we focus on the EM waves in the terahertz (THz) band, which lie between the microwaves and visible lights and have many unique applications ranging from safety checks, imaging to radar [1,2]. But until the time of writing, the EM waves in THz band still lack an efficient and compact generator.

The Josephson effect in Josephson junctions consisted of a blocking layer sandwiched by two superconducting electrodes provides us a unique method to excite EM waves with high frequencies [3–9]. In the presence of a biased voltage, the super-current oscillates at a frequency proportional to the voltage according to the ac Josephson relation, for example 1mV corresponds to 0.48THz. Collective excitations of cooper pairs and EM waves known as Josephson plasma are excited. At the edges of the junction, part of the Josephson plasma radiates into free space. Nevertheless the power radiated from a single junction is in range of picowatts which is too small for practical applications. Artificial array of Josephson junctions were tried first, but the frequency cannot reach the THz region due to the small superconducting gap in the conventional superconductors and the radiation power remains limited as the non-uniformities among artificial junctions [10–16]. Intrinsic Josephson effects were observed in cuprate high-T$_c$ superconductor $Bi_2Sr_2CaCu_2O_{8+\delta}$ (BSCCO) [17]. Compared with conventional low-temperature Josephson junctions the intrinsic Josephson junctions (IJJs) have the following advantages. First, the superconducting energy gap is large (60meV) which in principle can cover the whole THz range. Second, the junctions are homogeneous in atomic scale which favors coherent THz radiation. These merits make IJJs fantastic candidates as sources for powerful EM radiation in THz band. As a matter of fact, many experimental attempts for excitation of THz radiation from IJJs were made, for example by quasiparticle injection along the in-plane direction of BSCCO sample [18, 19] and by biasing a voltage on a BSCCO sample with step-like geometry [20]. There were theoretical studies focusing on possible THz radiation from IJJs by driving Josephson vortices [21–24]. It is also proposed that the THz EM radiation can be excited by sandwiching a narrow BSCCO mesa with gold electrodes under bias voltage [25].

An experimental breakthrough was achieved in 2007. By applying c-axis bias voltage, experimentalists successfully excited coherent THz radiation from a rectangular mesa mounted on the top of a substrate of a single crystal of BSCCO [26]. The radiation frequency and bias voltage obey the ac Josephson relation, and the strong radiation happens at cavity frequencies determined by the lateral size of the mesa [26]. The significant experimental discovery showed the potential to pave a practical way for strong radiation sources of THz band in a compact and solid device based on superconductivity. The breakthrough raises many interesting questions, such as why injected dc energy can be transformed into intense EM radiation without applying magnetic fields, and how can a large number of junctions ~ 600 be synchronized.

The experimental breakthrough inspired intensive discussion from both experimental and theoretical sides [27, 33, 37–46, 48–50]. Lin and Hu investigated the phase dynamics of IJJs under bias current in terms of sine-Gordon equations with strong inductive coupling [8, 27]. They proposed a novel π phase kink state, which explains successfully experimental results mentioned above. In the π kink state, $\pm\pi$ kinks in gauge-invariant phase difference in IJJs are developed in in-plane directions and arrange themselves alternatingly along the c direction. The uniform bias current and cavity modes are coupled by the π phase kink, which allows a large supercurrent flow into the system at the cavity resonances, and a part of dc energy is converted to EM radiation from the mesa edge [8, 27]. Experimentally, THz radiations were observed from IJJs with cylindrical geometry [42] as discussed theoretically [37, 41] and in the high bias region [43]. It is also found that the radiation power from IJJs can be enhanced by controlling the temperature distribution of the mesa sample [45].

From application perspective, the radiation power ($\sim$ 10 nW) in the present experimental design is still too weak to be practically useful. There are several possible reasons, first the system may not be synchronized to a uniform state efficiently and secondly the radiation power may be limited by the small radiation area of the system.

In this thesis, we mainly discuss three aspects of THz radiation from IJJs [48–50]. First we propose to synchronize the system to the π phase kink state by preparing its initial phase, which can be done by applying non-uniform bias voltage or making use of thermal fluctuations. It is found that the system can be driven into the π phase kink state efficiently from several initial phase configurations. The time before entering the π phase kink state is shorter when the starting phase is further away from the uniform configuration. Secondly we derive a general solution especially valid for high cavity modes and weak or moderate inductive couplings, which can enhance injection of dc energy and convert it to EM radiation. This state evolves into the π phase kink state at large inductive couplings. Thirdly we study a long BSCCO cylinder embedded in a dielectric material. A maximal radiation power is reached when the dielectric constant of wrapping material is tuned. The maximal condition is met where the radiation power equals the dissipation caused by Josephson plasma, which yields the optimal dielectric constant of wrapping material in terms of properties of BSCCO single crystal.

Chapter 2 starts with a brief review of the history on superconductivity. We derive the dc and ac Josephson relations by solving Schrodinger equations when two superconductors are weakly coupled. The phase dynamic of a short junction is investigated by the RCSJ (resistively and capacitively shunted junction) model then. At the end of this chapter the sine-Gordon equation for a single Josephson junction is given and the artificial array of Josephson junctions is also discussed.

In Chapter 3 the discovery of IJJs based on a layered high $\mathrm{T_c}$ cuprate superconductor BSCCO is introduced. The experimental efforts devoted to exciting THz radiation based on BSCCO single crystals are discussed include the experimental breakthrough in 2007. At the end of this chapter a summary of current situation of THz radiation based on BSCCO mesa is given.

In Chapter 4, the inductively coupled sine-Gordon equations are derived based on the Larangian of IJJs first, which composes a good model for the phase dynamics of IJJs. Then we discuss the proper boundary condition for the coupled sine-Gordon equations depend on the experimental setup. At last the π phase kink state discovered by Lin and Hu is introduced and its related phase dynamics are discussed. The far-field radiation patterns for a cylindrical mesa associated with π phase kink state are calculated based equivalence principle. These patterns are believed to be useful for understanding the resonant modes of the system and thus has a direct relevance to application.

In Chapter 5, we propose an efficient way to synchronize the system to the π phase kink state by preparing the initial phase configuration. Two kinds of initial phase configurations are investigated like random ones and several typical ordered one. The relation between the initial phase configurations and final states is investigated. The system with nonuniform distribution of conductance and critical current is also discussed.

We propose a general solution valid for small and medium inductive couplings in chapter 6. It is characterized by a structure in phase difference varying in lateral directions around $\pm\pi/2$ in form of cavity mode and an alternating configuration along the c direction similar to the π phase kink state. Compared with the π kink, the static term in phase difference of the present solution does not saturate to π and 0 at the sample edges. The present solution can enhance injection of dc energy into IJJs and covert it to THz EM radiation. This solution evolves smoothly into the π phase kink state at large inductive coupling and low cavity modes.

In Chapter 7, we propose to use a long BSCCO cylinder wrapped by a dielectric material to increase the radiation power from IJJs. First we investigate the cavity and the quality factor of the system according to Maxwells equations. Then we analyze the phase dynamics associated with π kink state in this system. At last, we give the optimal dielectric constant for radiation power in terms of the property of the superconductive single crystal and also the optimal radiation power.

Finally the summary is given in Chapter 8.

2 Josephson Junctions

2.1 Superconductivity

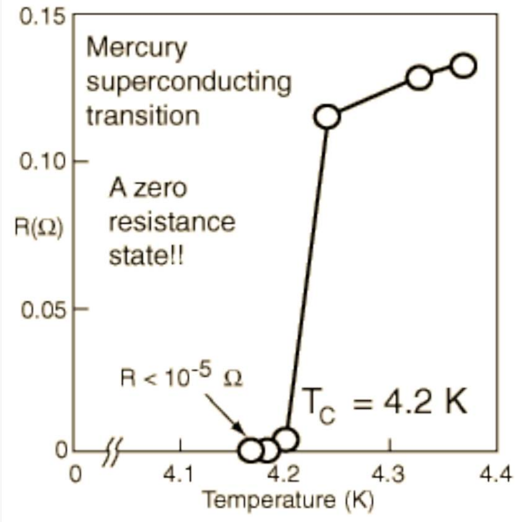

Figure 2.1: Resistivity of mercury suddenly dropped to zero at 4.2K [After H. K. Onnes, Commun. Phys. Lab. 12, 120 (1911)]

Superconductivity is a fantastic phenomenon observed in several metals and ceramic materials. When these materials are cooled below a characteristic critical temperature T_c, exactly zero electrical resistance and expulsion of magnetic fields occur in these materials. The phenomena of the disappearance of resistivity in metals below the critical temperature were first discovered by Kamerlingh Onnes [51] in 1911 at Leiden laboratory, just 3 years after he had liquified helium first, which gave him the refrigeration technique required to reach temperature of a few degrees Kelvin. The next great milestone in understanding superconductor occurred in 1933. Meissner and Ochsenfeld discovered that an expulsion of a magnetic field from a superconductor during its transition to the superconducting state, which indicates that the superconductivity cannot be simply understood as perfect conductivity [52]. Perfect conductivity and perfect diamagnetism are most two important characteristics in superconductors, which are also the principles to identify the superconducting states in experiments. One mainstream in the field of superconductivity is seeking superconductors that have higher T_c [53]. The first metal shown to be superconductor is mercury with T_c = 4.2K. In subsequent decades after the great discovery other superconducting metals, alloys and compounds were discovered. In 1941, niobium-nitride was found to be a superconductor at 16K. In 1953 vanadium-silicon displayed superconductive properties at 17.5K. In 1973, Nb_3Ge with T_c = 23.1K was added to the list. This alloy keeps the record of highest T_c until 1986 when cuprate superconductors were found. In 1986, a remarkable breakthrough discovery was made in the field of superconductivity. Bednorz and Müller, researchers at the IBM Research Laboratory in Rüschlikon, Switzerland, created a brittle ceramic compound that superconducts at the highest temperature then known: 30K [54]. The parent material for this superconductor is an insulator that had not been considered as a possible high T_c superconductor candidate before, however upon doping carriers the superconductivity set in. This breakthrough

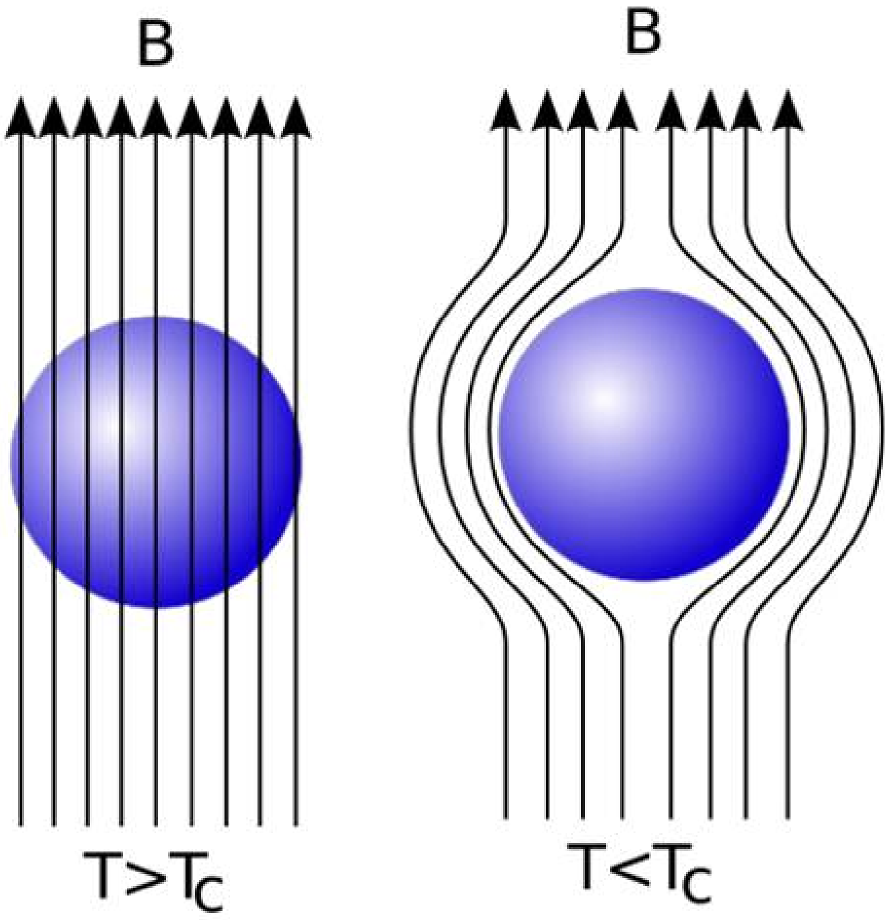

Figure 2.2: Schematic diagram of exclusion of magnetic flux from interior of superconductor.

triggered a blossom of cuprate superconductors, and the T_c is boosted to above 100K. The first superconductor working in liquid nitrogen is YBCO [55] and later BSCCO [56]. The world record of T_c of 164K for the time of writing is HgBaCaCuO [57,58] under 30GPa pressure. These cuprate superconductors all have the profoundly layered structure with superconductivity in the CuO layers.

MgB_2 is found to be superconductor by Akimistus's group with $T_c = 39K$ in 2001 [59]. Later it was confirmed that two bands contribute to the superconductivity. After that, the research on multi-band superconductors thrived and new phenomena unique to multi-band superconductors are discovered.

In 2008, it was found surprisingly that iron pnictide becomes superconductor below $26K$ by doping by Hosono's group [60] as usually one believes that superconductivity competes with magnetic order and thus magnetic element like Fe would destroy the superconductivity. The iron based superconductors are also found to be multi-bands superconductors.

The endeavor towards understand the origin of superconductivity started just after the discovery of superconductivity. In 1993, F. Londo and H. London proposed two equations which describe the microscopic electric and magnetic fields of superconductors [61,62]. These two equations can explain the perfect diamagnetism. And then Ginzburg and Landau proposed that the superconductivity can be described by a macroscopic complex wave function $|\Phi|e^{i\phi}$ [63]. The Ginzburg-Landau theory examines the macroscopic properties a superconductor with the aid of the general thermodynamic arguments.

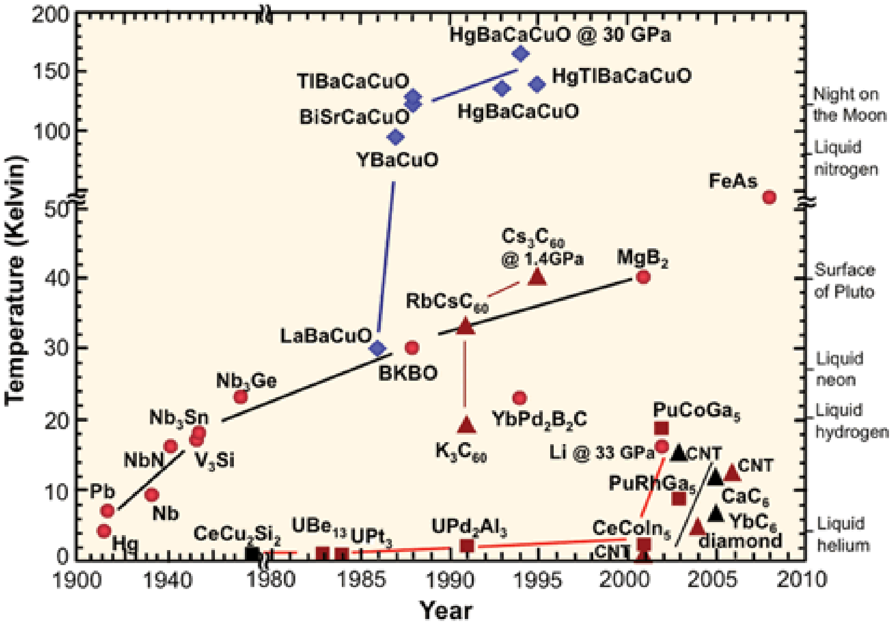

Figure 2.3: Timeline of superconductor and their critical temperature. Image courtesy of Department of Energy-Basic Energy Sciences (https://www.sc.doe.gov/bes/BES.html).

The first widely-accepted theoretical understanding of the microscopic origin of superconductivity was advanced by Bardeen, Copper and Schrieffer and their theory is later know as the BCS theory [64, 65]. The theory describes the superconductivity as a microscopic effect caused by a condensation of pairs of electrons into a boson-like state. It was also demonstrated that the GL theory can be derived from BCS theory near T_c and the complex wave functions correspond to the superconductivity energy gap [66].

Another significant theoretical milestone came in 1962 when Josephson, a graduate student at Cambridge University, figured out that electrical current would flow between two superconductors - even when they are divided by a non-superconducting material or insulator [3–5]. This tunneling phenomenon is today known as the "Josephson effect" and has been applied to electronic devices such as the SQUID, electronic oscillators and so on.

2.2 Josephson junction

The Josephson effect is the phenomenon of electric current across two weakly coupled superconductors that are separated by a very thin insulating barrier associated with coherent quantum tunneling of Cooper pairs (Figure 2.4). This setup, two superconductors coupled by a weak link that can be an insulating region, a normal metal, or a short, narrow constriction, is named as Josephson junction. The spontaneous (at zero bias voltage) dc current across the junction is the Josephson current.

The Josephson effect is related to many interesting and nonlinear phenomena. For example, when a Josephson junction is irradiated by a microwave, plateaus of constant voltage called Shapiro steps occur in the IV characteristics when the voltage is an integral multiple of $\omega\hbar/2e$ with ω the angular frequency of the microwave, $\hbar$ Planck's constant and e the charge of one electron [67]. The Shapiro steps can be used as voltage standard as the separations of plateaus of constant voltage are equal [68]. In the reverse process, the Josephson effect provides a unique way to excite high-frequency electromagnetic wave by applying a bias voltage to the Josephson junctions.

There are two kinds of Josephson effect i.e. dc Josephson effect and ac Josephson effect. Let us see the dc

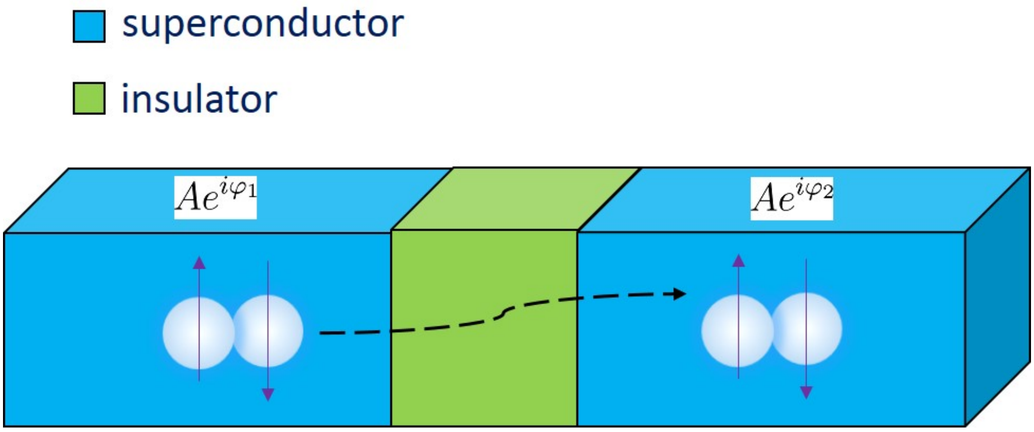

Figure 2.4: Schematic view of a Josephson junction. The cooper pair tunnels through the barrier without a bias voltage.

Josephson effect first. A macroscopic system in a superconducting state can be expressed by a single wave function $\Psi = Ae^{-i\varphi}$ with A a positive real number. When the two superconductors get close enough, Cooper pairs tunnels through the barrier between them, which makes the bilateral superconductors couple with each other weakly. The effective wave functions of two subsystems should satisfy the following wave equations

$$i\frac{\partial\Psi_1}{\partial t} = H_1\Psi_1 + k\Psi_2, \tag{2.1}$$

$$i\frac{\partial\Psi_2}{\partial t} = H_1\Psi_2 + k\Psi_1, \tag{2.2}$$

Where k is the coupling coefficient and $\Psi_1 = \sqrt{n_{s1}}e^{-i\gamma_1}$ and $\Psi_2 = \sqrt{n_{s2}}e^{-i\gamma_2}$ and n_s is the number of Cooper pair. Suppose that the two subsystems are identical and both at zero potential ($n_{s1} = n_{s2}, H_1 = H_2 = 0$) and take Ψ_1 and Ψ_2 into the wave Eqs.(2.1) and (2.2) we can obtain

$$\frac{\partial n_{s1}}{\partial t} = \frac{2k}{\hbar}\sin(\varphi_2 - \varphi_1), \tag{2.3}$$

$$\frac{\partial n_{s2}}{\partial t} = \frac{2k}{\hbar}\sin(\varphi_1 - \varphi_2), \tag{2.4}$$

$$\frac{\partial\varphi_1}{\partial t} = -k\sqrt{\frac{n_{s2}}{n_{s1}}}\cos(\varphi_2 - \varphi_1), \tag{2.5}$$

$$\frac{\partial\varphi_2}{\partial t} = -k\sqrt{\frac{n_{s1}}{n_{s2}}}\cos(\varphi_1 - \varphi_2), \tag{2.6}$$

Considering the charges of Copper pair are $2q$ the current density J can be expressed as

$$J = 2q\frac{\partial n_{s1}}{\partial t} = J_c \sin\varphi, \tag{2.7}$$

where $J_c = 4qkn_s/\hbar$ and $\varphi = \varphi_2 - \varphi_1$. Eq. (2.7) is the dc Josephson effect which means without a bias voltage a super current valued from $-J_c$ to J_c tunnels through the barrier between the superconductor electrodes. Then let us see the ac Josephson effect. If we apply a bias voltage V to a Josephson junction, the potential change is $-2qV$ when a Cooper pair tunnels from one superconductor to the other one. Then the Eqs.(2.1) and (2.2) can be written as

$$i\frac{\partial\Psi_1}{\partial t} = qV + k\Psi_2, \tag{2.8}$$

$$i\frac{\partial\Psi_2}{\partial t} = -qV + k\Psi_1. \tag{2.9}$$

Take Ψ_1 and Ψ_2 into this equation, we obtain

$$i\frac{\partial(\varphi_1 - \varphi_2)}{\partial t} = \frac{2qV}{\hbar}. \tag{2.10}$$

Eq. (2.10) is the ac Josephson relation which means the phase difference between two superconductor electrodes can be tuned by a bias voltage. For example, $1mV$ dc bias voltage can generate the oscillation of phase with 0.48THz. A more tractable derivation based on microscopic theory was given by Ambegaokar and Baratoff [69], and later by Larkin and Ovchinnikov [70].

2.3 RCSJ model

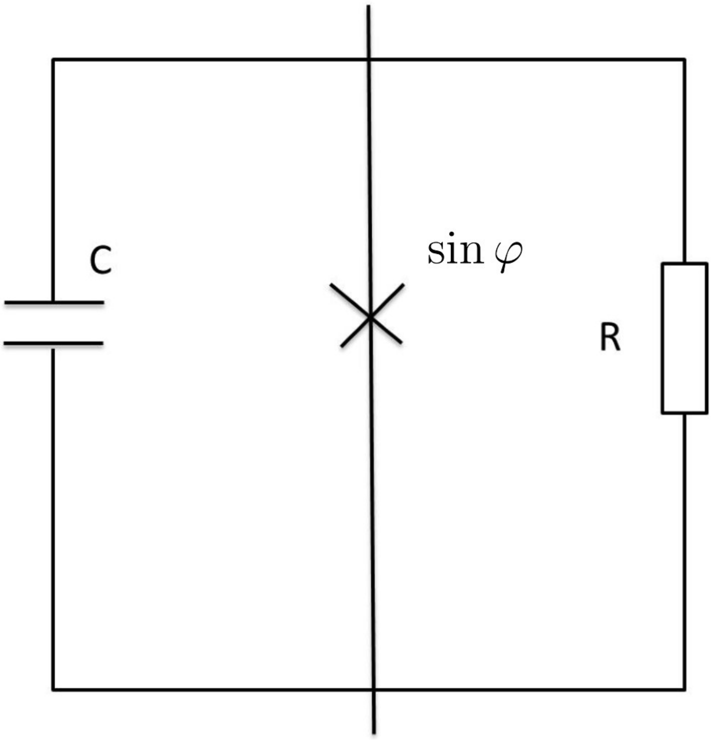

Figure 2.5: Equivalent circuit of RCSJ model, which consists three parts the resistor, the shunted junctions and the capacitor.

Although Eq. (2.7) suffices to characterize the zero voltage dc properties of a weak link, for finite voltage situations involving the ac Josephson effect, a more complete description is required. The RCSJ (resistive and capacitively shunted junction) model provides a simple picture for the phase dynamics in a short Josephson junction under bias voltage V when the penetration depth of magnetic field can be neglected. In the RCSJ model the Josephson junction is described approximately by an ideal one following Eq. (2.7), shunted by a resistance R for the dissipation in the finite voltage regime and a capacitance C reflecting the geometric shunting capacitance between the two electrodes, as schematically shown in Figure 2.5. Within the RSCJ model, the time dependence of the phase difference φ between two superconducting electrodes can obtained by equating the bias current to the total junction current as follows

$$J_{ext} = J_c \sin\varphi + V/R + C\frac{dV}{dt}. \tag{2.11}$$

Eliminating V from Eq. (2.10), we obtain phase dynamic equation in form of a second-order differential equation

$$\frac{d^2\varphi}{d\tau^2} + \frac{\beta'}{\omega_J}\frac{d\varphi}{d\tau} + \sin\varphi = \frac{J_{ext}}{J_c}, \tag{2.12}$$

where the dimensionless time variable $\tau = \omega_J t$ is used with $\omega_J = \sqrt{2qJ_c/\hbar C}$ and $\beta' = 1/RC$. Eq. (2.12) can be understood as the equation of motion of a classical particle in a washboard potential $\cos\varphi$ tilted by the external current with mass $(\hbar/2q)^2C$ and the viscous drag represented by the conductivity β'. The I-V characteristic of a Josephson junction under bias voltage can be obtained by solving Eq. (2.12) numerically. With applied a current below I_c, the system shows zero voltages. For the small C, the inertia is dominated by the viscous drag which means that the voltages increases continually with current beyond the critical current and approaches the linear current-voltage line given by the conductivity. For the large C, the I-V characteristic becomes hysteretic due to the inertial effect. When the applying current exceeds critical current, the voltage jumps discontinuously from zero to a finite value. In the process of decreasing current the voltage remains limited even below the critical current and becomes zero at a retrapping current.The I-V characteristic for different ratios of ω_j and β' obtained by the numerical simulation of Eq. (2.12) is shown in Figure 2.6.

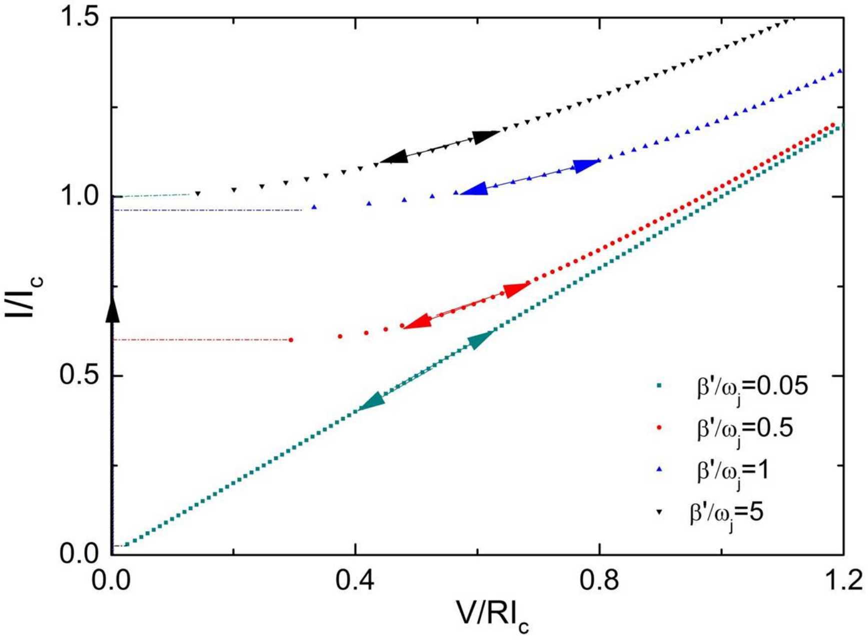

Figure 2.6: I-V characteristic for different values of β' obtained by numerical simulation, arrows indicate the direction of current sweeping.

2.4 Sine-Gordon equation

When a Josephson junction that has one or more dimensions longer than the penetration depth of the magnetic field produced by Josephson current, the Josephson currents in the EM fields should be taken into account which leads to the sine-Gordon equation. First we should introduce the gauge-invariant phase difference that takes the effect of the coupling of the change to the vector potential, whose definition is given by

$$\gamma = \varphi_1 - \varphi_2 - \frac{2e}{\hbar}\int \mathbf{A}\cdot d\mathbf{s} \tag{2.13}$$

with **A** the vector potential and integration over the insulating barrier. The derivation of sine-Gordon equation for a long Josephson junction is given as follows. Let us consider a Josephson junction with two dimensions (along y direction is uniform). The coordinate system is set as that the electrode surfaces are parallel to the x direction and the tunnel current is along z direction. The thickness of the insulator barrier between two superconducting electrodes is d and the penetration depth of the magnetic field is λ. From the Maxwell's equation that

$$\nabla \times \mathbf{E} = -\frac{1}{c}\frac{\partial \mathbf{B}}{\partial t}, \tag{2.14}$$

and integrate this equation along the direction z we obtain

$$\frac{\partial E_z}{\partial x} = \frac{2\lambda + d}{d}\frac{1}{c}\frac{\partial B_y}{\partial t}, \tag{2.15}$$

where the magnetic field extends into the superconductor with penetration depth λ on the both sides and electric field is negligible except in the barrier. Then from the Maxwell's equation for the displacement current we have

$$\frac{\partial B_y}{\partial x} = \frac{4\pi}{c}J_z + \frac{\varepsilon_c}{c}\frac{\partial E_z}{\partial t}, \tag{2.16}$$

where J_z is the tunneling current and ε_c is the dielectric constant of the insulator barrier. Then combining the time derivative of Eq. (2.15) with Eq. (2.16) we arrive at

$$\left(\frac{\partial^2}{\partial x^2} - \frac{1}{\bar{c}^2}\frac{\partial^2}{\partial t^2}\right)V = \frac{4\pi}{c^2}(2\lambda + d)\frac{\partial J_z}{\partial t}, \tag{2.17}$$

where $V = E_z d$ is the voltage across the barrier, and

$$\bar{c}^2 = \frac{c^2}{\varepsilon(1 + 2\lambda/d)}. \tag{2.18}$$

As $\lambda \gg d$ the asymmetry between E and B make the Josephson junction a "slow-wave" structure [71].

More generally we can rewrite Eq. (2.17) in terms of the phase difference γ with applying the dc and ac Josephson relation as

$$\left(\frac{\partial^2}{\partial x^2} - \frac{1}{\bar{c}^2}\frac{\partial^2}{\partial_t^2}\right)\gamma = \frac{\sin\gamma}{\lambda_J^2}, \tag{2.19}$$

where λ_J is the Josephson penetration depth given by

$$\lambda_J = \left[\frac{c\Phi_0}{8\pi^2 J_c(2\lambda + d)}\right]^{1/2} \tag{2.20}$$

with typical value $\sim$ 1mm for Josephson junctions made of conventional low-temperature superconductors. Eq. (2.19) is usually referred as the *sine*-Gordon equation.

Besides the tunneling current, normal ohmic current and external current can also be included which leads to the perturbed sine-Gordon equation

$$\left(\frac{\partial^2}{\partial x^2} - \frac{1}{\bar{c}^2}\frac{\partial^2}{\partial_t^2}\right)\gamma = \frac{1}{\lambda_J^2}(\sin\gamma - \sigma\frac{\Phi_0\partial_t\gamma}{J_c} - \frac{J_{ext}}{J_c}). \tag{2.21}$$

There are several important solutions to the sine-Gordon equations such as the small amplitude plasma solution

$$\gamma(x, t) = A\exp(\mathrm{i}(\mathrm{kx} - \omega\mathrm{t})) \tag{2.22}$$

and the soliton solution [72–74]

$$\gamma = 4 \arctan \exp \left(\frac{\mathrm{x - ut}}{\sqrt{1 - u^2}} \right), \tag{2.23}$$

corresponding to a rotating of γ from 0 to 2π. The derivation of soliton solution is given as follows [72–74]. We focus on the solution towards the positive direction of x axis

$$\gamma = \gamma(x - ut), \tag{2.24}$$

where u is a constant propagation velocity. Then the equation can be simplified into

$$\frac{d^2\gamma}{d\xi^2} = \frac{\sin\gamma}{1 - u^2}. \tag{2.25}$$

Integrating Eq. (2.25) one obtains

$$\frac{d\gamma}{d\xi} = \sqrt{\frac{2(E - \cos\gamma)}{1 - u^2}}, \tag{2.26}$$

where E is the integration constant. For $E = 1$ we have the soliton solution.

2.5 Electromagnetic radiation based on Josephson junctions

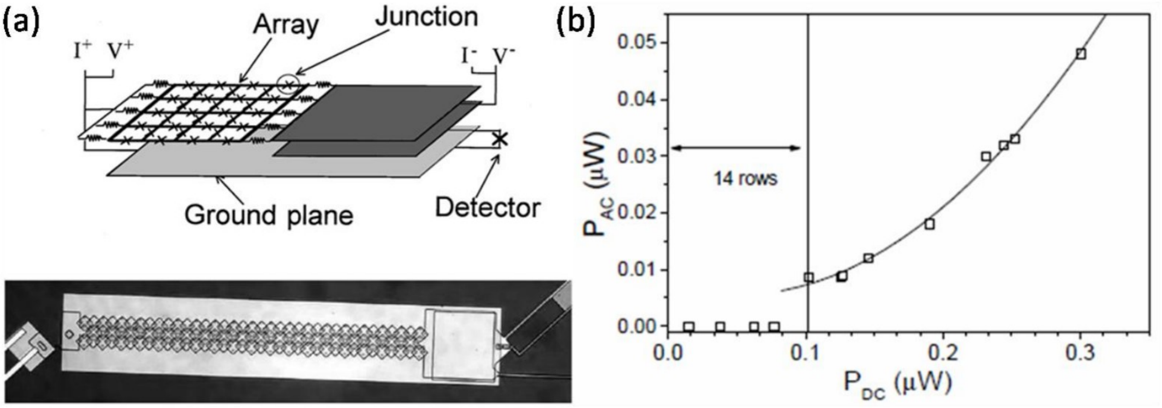

Figure 2.7: (a) Sketch of a typical sample (top). The quare array, to the left, is capacitively coupled to a detector circuit, on the right. A ground plane underlies the entire structure. Picture of a 3×36 array (bottom). The length of the array is about $470\mu m$. (b) Detected ac power P_{AC} as a function of the dc input power P_{DC} for a 3×36 array (open squares). If all the non-zero voltage junctions are on the same dynamical state (resonant step, in this case), the input dc power is proportional to the number of these junctions. No output power is measured below 14 active rows. The solid line the best quadratic fit f or the data above 14 rows. For the units used in the plot, $P_{\mathrm{ac}} = 0.007 - 0.07P_{\mathrm{dc}} + 0.7P_{\mathrm{dc}}^2$. [After P. Barbara *et al*, Physical Review Letters 82, 1963-1966 (1999).]

It has been noticed that the Josephson effect can be used for exciting EM wave especially at high frequencies since its discovery [3–6]. The first observation of EM radiation from single junctions was confirmed in 1960s. In 1965, a resonant radiation at the Fiske steps [75] was detected by Yanson *el al* [76] and Langenberg *el al* [77]. Later then, it is reported that the radiation can also be caused by the motions of solitons [78]. The radiation power in these experiments is in a range of pW that is too small for useful applications.

It is natural to integrate many Josephson junctions into an array, and intense radiation can be expected when the synchronization of junctions array is achieved (Figure 2.7). One tried to align the junctions on a plane and connect to each other to form a two-dimensional network of junctions [10–15] or simply stack up junctions [16]. Due to the small superconductive gap of the conventional superconductor and the non-uniformities among junctions, the observed frequency is below THz range and radiation power is also limited.

Synchronization is hard to be achieved in these kinds of an artificial array of Josephson junctions. One proposed that the junctions can be synchronized to a uniform state by making using of electromagnetic coupling with attaching all the junctions to a common resonator. As demonstrated by Barbara *el al* [15], the observed radiation energy is about 0.1μW at the frequency 150 GHz (Figure 2.7).

3 Intrinsic Josephson junctions

3.1 Intrinsic Josephson effects in cuprate high T$_c$ superconductors

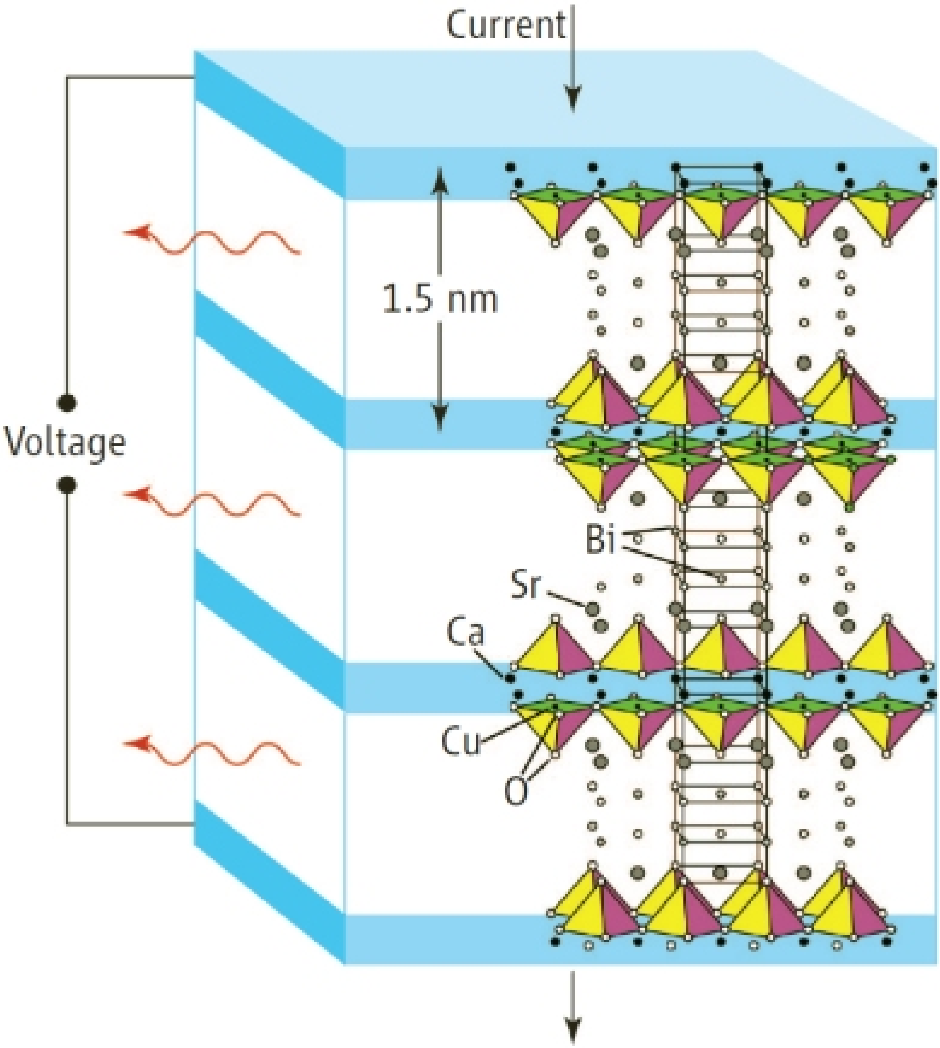

Figure 3.1: Crystal structure of BSCCO. Blue part indicate the superconducting layers and between them are the insulating ones (http://physicsworld.com/).

In 1992, the intrinsic Josephson effects were discovered in cuprate high T$_c$ superconductor BSCCO by Kleiner *et al* [17] which gives new possibilities to the development of electromagnetic devices using cuprate superconductors. Due to the big asymmetry of coherence length of superconducting state between the direction parallel to the CuO_2 layers ($\sim$ 15Å) and the direction perpendicular to the layers($\sim$ 1Å), the amplitude of order parameter of superconducting state is large in the CuO_2 double layers but very small in the BiO and SrO layers, which renders BSCCO a stack of Josephson junctions intrinsically. The superconductivity mainly takes place on CuO layer, while other components seem to provide carriers. The crystal structure of BSCCO is shown in Figure 3.1. A BSCCO single crystal of, say, 1 μm in thickness has about 600 Josephson junctions each having a thickness of 15Å. As each of the junctions can be either in the superconducting state or normal resistive state depending on the bias current, there are many branches in the I-V characteristics [17].

The IJJs in cuprate high-T_c superconductor BSCCO provides a nice candidate to achieve strong, coherent THz radiation. Compared with conventional superconductors the BSCCO has large superconductivity gap that can cover the whole range of THz band in principle. Furthermore, the IJJs in BSCCO are homogeneous at atomic scale guaranteed by the high quality of the crystal that make the coherent radiation possible. Once the synchronization among junctions is established, the radiation power is proportional to the square number of junctions, for example a typical 1.5-μm-thick BSCCO mesa contains about 1000 junctions, and thus enabling power to be theoretically enhanced by a factor $\sim 10^6$ relative to a single junction.

3.2 Experimental efforts towards THz radiation from IJJs

The EM radiation from IJJs was first observed experimentally by Kleiner *et al*(1992, 1994) [17, 79] based on BSCCO single crystal with a sample of 30 μm in lateral dimensions and 3 μm in the stack direction under a bias voltage perpendicular to stack direction. The ac Josephson relation is confirmed in IJJs in this experiment. The EM radiation in THz band from IJJs based on BSCCO single crystal was first reported by Batov *el al* in 2006 [20] with the step-like geometry. The observed radiation frequency is 0.5 THz, and the power is in an order of pW. The radiation is weak here due to the radiation only takes place from a single junction.

3.2.1 Breakthrough in exciting THz radiation

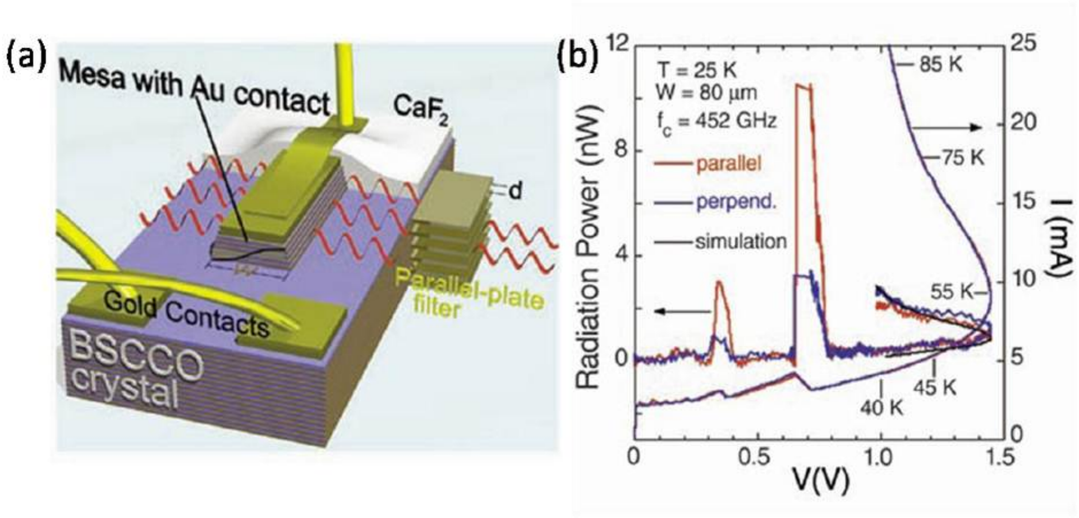

Figure 3.2: (a) Schematic of the BSCCO mesa. (b) I-V characteristics and radiation power of the 80 μm mesa. The voltage dependence of the current (right vertical axis) and the radiation power (left vertical axis) at 25 K for parallel and perpendicular settings of the filter with 0.452THz cut-off frequency are shown for decreasing bias in zero applied magnetic field. Polarized Josephson emission occurs near 0.71 and 0.73 V, and unpolarized thermal radiation occurs at higher bias. The black solid line is a simulation of the thermal radiation. [After L. Ozyuzer *el al*, Science 318, 1291-12936(2007).]

In 2007, an experimental breakthrough was achieved by an international team from Argonne National Lab of US and University of Tsukuba of Japan where a coherent THz EM waves were observed successfully from the IJJs based on a BSCCO single crystal mesa under a dc bias voltage, see Figure 3.2. The maximum radiation power detected is about 20 nW, and the radiation frequency is about 0.6 THz. The bias voltage and frequency follow the ac Josephson relation and the frequency where intense radiation happens equals one of the cavity modes determined by the lateral size of the mesa

$$f_0 = c/2W\sqrt{\varepsilon} \tag{3.1}$$

with W the width of the mesa.

3.2.2 Progress after the breakthrough

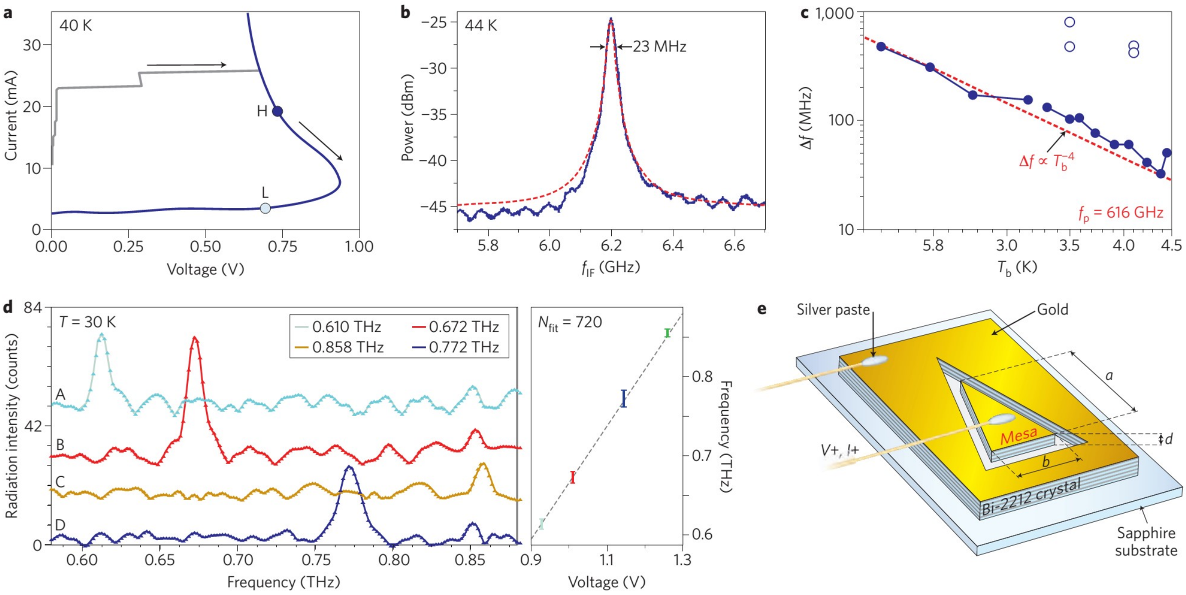

Figure 3.3: (a) I-V curve of a 50-μm-wide mesa at 40 K. Emission is observed at two working points for the same voltage (that is, resonance frequency): one at a high current bias, H, the other at a low current bias, L (ref. [44]). (b), Emission line from a 50-μ-wide mesa at 44 K operated in the high-bias regime at a current of 16.3 mA (ref. [44]). The spectrum was obtained using heterodyne mixing with a local oscillator frequency of 605.75 GHz. The green dashed line represents a fit to a Lorentzian line profile. (c) Temperature dependence of the linewidth in the high-bias (solid symbols, see a) and low-bias regimes (open symbols). The red line indicates a fit $\Delta f \approx T_b^{-4}$, where T_b is the cryostat temperature. The linewidth in the high-bias regime is about a factor of ten smaller than that in the low-bias regime. (d), Voltage tunability of the emission from a resonator in the shape of an acute isosceles triangle (shown schematically in e) in the high-bias regime at a cryostat temperature of 30 K (ref. [81]). [after U. Welp *et at*, Nature Photonics, 7, 702 (2013).]

This breakthrough is just the beginning of the exciting field. There are still many challenges, and questions remained. For example, it is still not clear for that how a large number of junctions about 600 can be synchronized to a uniform and how a uniform dc current can transfer energy into a spatially non-uniform cavity mode efficiently. Koshelev and Bulaevskii proposed that a modulated critical current breaks the symmetry that enables efficient coupling into the cavity modes [33]. Lin and Hu found a naturally formed π phase kink state, which can explain the important experimental result mentioned above [8, 27]. The π phase kink state has been confirmed by innumerous simulations then. Besides the theoretical studies, the THz radiations from BSCCO mesa have been observed from various geometries like cylindrical ones [42] and triangular ones [80, 81]. In the present experimental setup, the Joul heating due to ohmic dissipation is severe, because the dissipation is proportional to the volume of BSCCO mesa while the heat removal only occurs at the interface between the mesa and the substrate. Although the sample is immersed in the liquid helium, the temperature of the sample is still much higher than the ambient temperature, and almost reaches T_c due to the strong self-heating effect when the current is large. The heating modifies the IV curves into an s-shape and even drives part of the mesa into the normal state. Wang *et al* observed the THz radiation from BSCCO mesa in the high bias region which has the same resonance condition as low bias one [43,44]. The effect of Joule heating is not always detrimental as one would expect, but experiments suggest that the thermal effect may play a decisive role. It is found that the radiation power may be enhanced if one controls the temperature distribution of the sample [45,46]. The observed radiation power remains limited in these experiments which is about 30 nW and not enough for practical applications. The possible reasons are as follows, first the system may be not driven into a uniform state efficiently where only partial junctions are in resonant states and secondly the radiation area is too small in the present experimental setup which restraints the radiation power.

4 Inductively coupled sine-Gordon equations

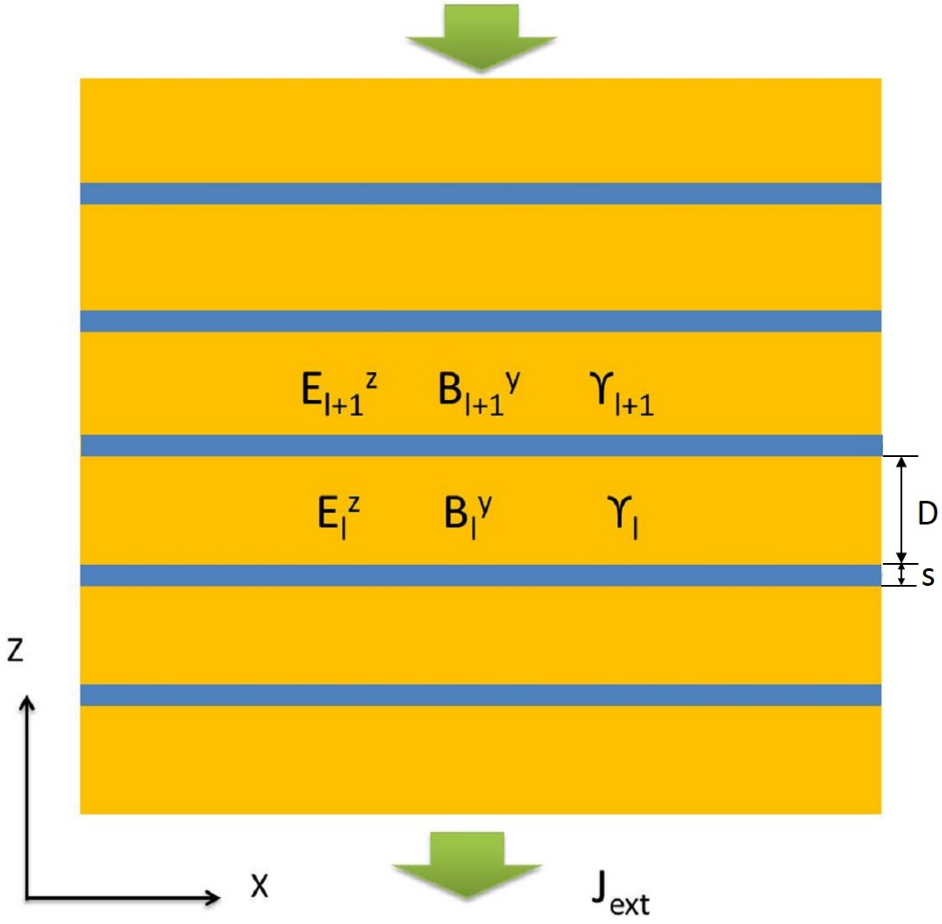

Figure 4.1: Schematic view of a stack of IJJs. The blue/yellow area denotes superconducting/insulating layers.

The theory on mechanism of superconductivity in the strongly correlated electron system like BSCCO has not been established well up to date. One convenient phenomenological model of layered superconductor is proposed by Lawrence and Doniach which assumes a Josephson coupling between different layers [82]. The geometry we consider is plot in Figure 4.1. According to the Lawrence-Doniach model, the energy density stored in the superconductive layer is given as [39]

$$H_{sl} = \frac{1}{8\pi}\int_{l(s+D)+D}^{(l+1)(s+D)} [\lambda_s^2(\nabla\times B_{sl}^{y2})_x^2 + B_{sl}^{y2}]dz, \tag{4.1}$$

where the first term is the supercurrent energy, second term is the magnetic energy, λ_s is the penetration depth and B_{sl}^y is the magnetic field in the lth superconductive layer. The energy stored in the insulating layer is given by the sum of EM energy and Josephson coupling as

$$H_{bl} = \frac{1}{8\pi}\int_{l(s+D)}^{l(s+D)+D}\left(B_l^{y2} + \varepsilon_c E_l^{z2}\right)dz + \frac{\Phi_0}{2\pi c}J_c(1-\cos\gamma_l), \tag{4.2}$$

where E_l^z (B_l^y) is the electric (magnetic) field in the l-th insulating layer and their variation along z direction will be neglected in following discussion, J_c is the critical current, ε_c is the dielectric constant of the insulating layer, Φ_0 is the quantum flux given as $\Phi_0 = hc/2e$ and γ_l is the gauge-invariant phase difference in the l-th layer defined as

$$\gamma_l = \phi_{l+1} - \phi_l - \frac{2\pi}{\phi_0}\int_{l(s+D)}^{l(s+D)+D} A_l^z dz \tag{4.3}$$

with A_l^z the vector potential. As in high T$_c$ superconductor the penetration depth λ_s is much larger than the thickness of insulating layer D and superconducting layer s, the magnetic field in the superconductive layer can be written approximately as [39]

$$B_{sl}^y(z) \approx \frac{[(s-z)B_l^y + zB_{l+1}^y]}{s}. \tag{4.4}$$

Then the total energy of the system can be obtained as

$$\begin{aligned} H &= \sum_l (H_{sl} + H_{bl}) \\ &= \sum_l \frac{D}{8\pi}\left[(2\zeta+1)B_l^{y2} - \zeta(B_{l+1}^y B_l^y + B_l^y B_{l-1}^y) + \varepsilon_c E_l^{z2}\right] + \frac{\Phi_0}{2\pi c}J_c(1-\cos\gamma_l) \end{aligned} \tag{4.5}$$

with $\zeta \equiv \lambda_s^2/sD$ the inductive coupling constant. If one takes the derivative of Eq. (4.3) one obtains the relation between the gauge-invariant phase difference and the magnetic field in y direction as

$$\frac{\Phi_0}{2\pi D}\partial_x \boldsymbol{\gamma}_l = \mathbf{M}\mathbf{B}_y, \tag{4.6}$$

where the relation $J_l = c\Phi_0\partial_x\gamma_l/2\lambda_s^2$ and the Maxwell equation $\partial_z B_l^y = 4\pi J_l^x/c$ are used, $\boldsymbol{\gamma} = (\gamma_1, \gamma_2, ..., \gamma_N)^T$, $\mathbf{B}_y = (B_1^y, B_2^y, ..., B_N^y)^T$ with N the number of junctions and M is inductive coupling matrix given as

$$\begin{pmatrix} 2\zeta+1 & -\zeta & 0 & \cdots & & 0 & -\zeta \\ -\zeta & 2\zeta+1 & -\zeta & 0 & \cdots & & 0 \\ 0 & \ddots & \ddots & \ddots & 0 & \cdots & \\ \cdots & 0 & -\zeta & 2\zeta+1 & -\zeta & 0 & \cdots \\ & \cdots & 0 & \ddots & \ddots & \ddots & 0 \\ 0 & & \cdots & 0 & -\zeta & 2\zeta+1 & -\zeta \\ -\zeta & 0 & & \cdots & 0 & -\zeta & 2\zeta+1 \end{pmatrix}, \tag{4.7}$$

with the periodic boundary condition along c direction adopted here as we are interested in uniform state as discussed later. Rewriting Eq. (4.5) in terms of Eq. (4.6) and the ac Josephson relation $\partial_t\boldsymbol{\gamma} = 2e\mathbf{E_z}D/\hbar$, one obtains the energy density in the following compact form as

$$H = \frac{1}{2}(\mathbf{M}^{-1}\partial_x\boldsymbol{\gamma}^T\partial_x\boldsymbol{\gamma} + \partial_t\boldsymbol{\gamma}^T\partial_t\boldsymbol{\gamma}) + \sum_l(1-\cos\gamma_l), \tag{4.8}$$

where the dimensionless units are used which are summarized in Table 4.1, the first term is the total magnetic energy, the second term is the total electric energy and the last term is the total Josephson coupling energy. The corresponding Lagrangian to Eq. (4.8) is given as

$$L = \frac{1}{2}(\mathbf{M}^{-1}\partial_x\boldsymbol{\gamma}^T\partial_x\boldsymbol{\gamma} + \partial_t\boldsymbol{\gamma}^T\partial_t\boldsymbol{\gamma}) - \sum_l(1-\cos\gamma_l). \tag{4.9}$$

Quantities	Dimensionless Units	Gaussian Units	SI Units
Lentgth	x	$\lambda_c x$	$\lambda_c x$
Time	t	t/ω_p	t/ω_p
Conductance	β	$c\sqrt{\varepsilon_c}\beta/4\pi\lambda_c$	$c\sqrt{\varepsilon_c\varepsilon_0}\beta/\lambda_c$
Electric field	E	$\Phi_0\omega_p E/2\pi cd$	$\Phi_0\omega_p E/2\pi d$
Voltage	V	$\Phi_0\omega_p V/2\pi c$	$\Phi_0\omega_p V/2\pi$
Magnetic field	B	$\Phi_0 B/2\pi\lambda_c d$	$\Phi_0 B/2\pi\lambda_c d$
Poynting Vector	$E \times B$	$\Phi_0^2\omega_p EB/16\pi^3 d^2 d\lambda_c$	$\Phi_0^2\omega_p EB/4\pi^2\mu_0 d^2\lambda_c$
Current	J	$J_c\Phi_0/8\pi^2\lambda_c^2 d$	$\Phi_0/2\pi\lambda_c^2 d\mu_0$
Impedance	Z	$Z/\sqrt{\varepsilon_c}$	$Z/\sqrt{4\pi\varepsilon_c\varepsilon_0}$

Table 4.1: Conversion of quantities among dimensionless, Gaussian and SI unit. Here λ_c and λ_{ab} are the penetration depth along the *ab* plane and c axis; ε_c is the dielectric constant along c direction; c is the light velocity in vacuum; ε_0 is the dielectric constant of vacuum; $\omega_p = c/\lambda_c\sqrt{\varepsilon_c}$ is the Josephson plasma frequency. $J_c = c\Phi_0/8\pi^2\lambda_c^2 D$ is the critical current density. For BSCCO single crystal, $\lambda_c = 200\mu m$, $\lambda_{ab} = 0.4\mu m$, $\varepsilon_c = 10$, $s = 0.3nm$, $D = 1.2nm$. Then $\lambda_s = \sqrt{sd/(s+d)^2\lambda_a b} = 0.16\mu m$. The the dimensionless parameter is then $\beta = 0.02$.

If one takes the energy coming from external current into account, the Lagrangian takes the form

$$L = \frac{1}{2}(\mathbf{M}^{-1}\partial_x\boldsymbol{\gamma}^T\partial_x\boldsymbol{\gamma} + \partial_t\boldsymbol{\gamma}^T\partial_t\boldsymbol{\gamma}) - \sum_l(1-\cos\gamma_l) + J_{\text{ext}}\sum_l\gamma_l, \tag{4.10}$$

with J_{ext} the external current in unit of J_c. Resorting to the Euler-Lagrangian formula $\partial L_l/\partial\gamma_l = d\partial L_l/dt\partial(\partial_t\gamma_l)$, one obtains the following equation

$$\mathbf{M}^{-1}\partial_x^2\boldsymbol{\gamma} = \partial_t^2\boldsymbol{\gamma} + \sin\boldsymbol{\gamma} - J_{\text{ext}}\mathbf{I}. \tag{4.11}$$

If one adds the ohmic current as perturbation, the inductively coupled sine-Gordon equations are arrived

$$\partial_x^2\boldsymbol{\gamma} = \mathbf{M}(\partial_t^2\boldsymbol{\gamma} + \beta\partial_t\boldsymbol{\gamma} + \sin\boldsymbol{\gamma} - J_{\text{ext}}\mathbf{I}) \tag{4.12}$$

with β the dimensionless conductance. For three dimensional case, the inductively coupled sine-Gordon equations are written as

$$\Delta\boldsymbol{\gamma} = \mathbf{M}(\partial_t^2\boldsymbol{\gamma} + \beta\partial_t\boldsymbol{\gamma} + \sin\boldsymbol{\gamma} - J_{\text{ext}}\mathbf{I}) \tag{4.13}$$

where Δ is the Laplace operator in lateral directions and $\mathbf{I} = (+1, +1, +1, +1, ...)^T$ the unit vector; the coupling matrix $(\mathbf{M})_{l,l-1} = (\mathbf{M})_{l,l+1} = -\zeta$, $(\mathbf{M})_{l,l} = 1 + 2\zeta$ and zero otherwise with $\zeta \equiv (\lambda_{ab}/s)^2$ the inductive coupling (λ_{ab} the penetration depth in the c direction and s the period of IJJs lattice in c-direction); the lateral length and time are scaled by the penetration depth in the ab-plane λ_c and the inverse of intrinsic plasma frequency $\omega_c = c/\lambda_c\sqrt{\varepsilon_c}$ (ε_c the dielectric constant of BSCCO) respectively; $\beta \equiv 4\pi\sigma_c\lambda_c/c\sqrt{\varepsilon_c}$ is the normalized c-axis conductivity of BSCCO sample and J_{ext} is the external current normalized by the critical current J_c

4.1 Boundary conditions

Now we have obtained the inductively coupled sine-Gordon equations which composes a good model for the phase dynamics of IJJs, to obtain a complete solution of phase state we also need the boundary conditions supplemented to the coupled equations which gives the connection between the IJJs and the external world.

For the boundary condition along c direction, we adopt the periodic one as we are interested in the uniform state and the external current has already been taken into account in the present phase gauge.

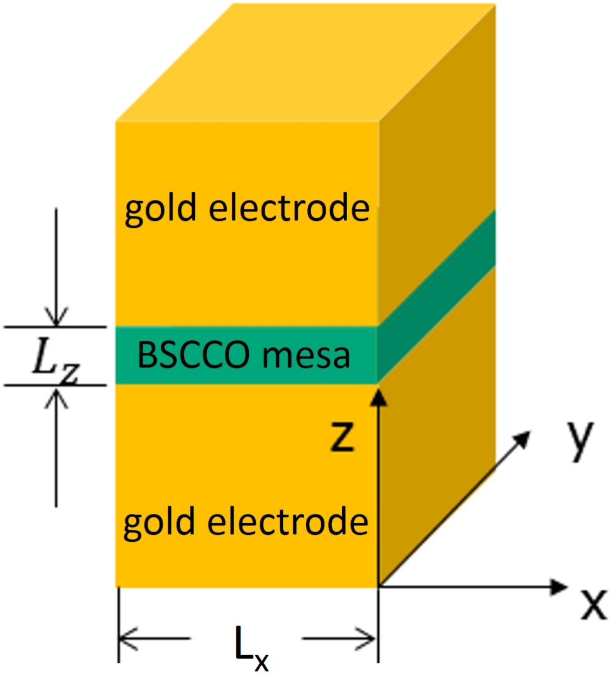

Figure 4.2: Schematic view of a stack of IJJs sandwiched by two gold electrodes.

For the boundary condition along x direction, as discussed by R. Kleiner a stack of IJJs forms a cavity mode in most cases [83]. There are two kinds of boundary conditions for a cavity system generally, namely the perfect-electric-conductor (PEC) boundary condition and the perfect-magnetic-conductor (PMC) boundary condition. For the PEC (PMC) boundary condition, the electric (magnetic) fields perpendicular to the edges of mesa reaches zero at the boundaries. The question here we need to answer is which boundary condition matches the situation of experimental setup. The schematic figure of experimental setup is shown in Figure 4.2, where a thin mesa about $1\mu m$ is sandwiched by two gold electrodes. As the thickness of BSCCO mesa is much smaller than the wavelength of EM field inside the mesa, the impedance at the edges is very large $Z \sim \lambda/L_z$ [33], thus the magnetic field along y direction is almost zero compared with electric field in z direction, which leads to the PMC boundary condition.

The detailed derivation is given as follows [33]. We have electric field and magnetic field of the whole space in Fourier form as

$$\mathbf{E}(\mathbf{r}) = \int \frac{d^3k}{(2\pi)^3}\mathbf{E}(\mathbf{k})e^{-i\mathbf{k}\cdot\mathbf{r}},\ \mathbf{B}(\mathbf{r}) = \int \frac{d^3k}{(2\pi)^3}\mathbf{B}(\mathbf{k})e^{-i\mathbf{k}\cdot\mathbf{r}}. \tag{4.14}$$

Then based on the Maxwell equations $\nabla\cdot\mathbf{E}(\mathbf{r}) = 0$ and $\nabla\times\mathbf{E}(\mathbf{r}) = ik_\omega\mathbf{B}(\mathbf{r})$, we obtain the relation between the electric field in z direction and the magnetic field in y direction as

$$k_xE_x + k_zE_z = 0 \tag{4.15}$$

$$ik_\omega B_y = -ik_xE_z + ik_zE_x, \tag{4.16}$$

which just gives the following expression

$$B_y(\mathbf{k}) = -\frac{\varepsilon_d k_\omega}{\sqrt{\varepsilon_d k_\omega^2 - k_z^2}}E_z(\mathbf{k}) \tag{4.17}$$

with applying the relation $k_x = \sqrt{\varepsilon_d k_\omega^2 - k_z^2}$, ε_d the dielectric constant in unit of ε_c and $k_\omega = \omega = 2\pi/\lambda$. Then we apply inverse Fourier transformation to Eq. (4.17) with the help of convolution theorem, we have

$$B_y(\mathbf{r}) = -\int_{-\infty}^{\infty} dz' U(z-z') E_z(L,z'), \tag{4.18}$$

where $U(z) = \varepsilon_d k_\omega J_0(\varepsilon_d k_\omega z)/2$ is the inversed Fourier transformation of $\varepsilon_d k_\omega / \sqrt{\varepsilon_d k_\omega^2 - k_z^2}$. As $L_z \ll \lambda$ and the screen effect of gold electrodes, the electric field in z direction is zero outside mesa and $E_z(L,z') \approx E_z(L,0)$ inside the meas. In this situation, one has the magnetic field in y direction in terms of electric field in z direction as

$$B_y(L,0) = \frac{L_z k_\omega}{2} E_z(L,0) \sim \frac{L_z}{\lambda} E_z(L,0), \tag{4.19}$$

which just gives the almost infinitely large impedance at the edges of mesa $Z = E_z/B_y \sim \lambda/L_z$. Thus one can take the PMC boundary condition as a good approximation for the present experimental setup.

4.2 McCumber state

Eq. (4.12) has a trivial running solution, which is given as [8, 27]

$$\gamma = \omega t + A_0 \sin(\omega t + \varphi) \tag{4.20}$$

with $A_0 \sim 1/\omega^2$. For this so called McCumber state, most current runs from the ohmic channel and only a very small partial of current runs from superconductive channel. For the typical applied frequency in THz range, $\omega \sim 10$, only 1% current is the superconducting one. For this solution, most external energy becomes Joule heating and no strong radiation and cavity resonance phenomenon can be expected.

4.3 π phase kink state

In 2008, a new solution to the coupled sine-Gordon equations has been found [8, 27] which can explain the important features in the previous experimental observation for THz radiation from IJJs based on BSCCO mesa [26]. Considering the cavity relation of radiation frequency and the plasma oscillation should be uniform in c axis [26], the general form of π phase kink solution [8, 27] for the coupled sine-Gordon equations is given by

$$\gamma_l(\mathbf{r},t) = \omega t + A g(\mathbf{r}) e^{i\omega t} + (-1)^l \gamma^s(\mathbf{r}), \tag{4.21}$$

where the first term is the rotating phase accounting for the finite dc bias voltage; the second term stands for the cavity term of plasma oscillation, where A is the complex amplitude, $g(\mathbf{r})$ is the cavity mode of electric field in the c direction which is complex for the open system, and the frequency ω is given by the bias voltage based on the ac Josephson relation; the third term is the π phase kink which carries the strong interjunction coupling via the l dependence.

Inserting Eq. (4.21) into Eq. (4.13) and omitting higher harmonics for $|A| \ll 1$ we arrive at the following equation

$$-k^2 A g e^{i\omega t} + f_l \triangle \gamma^s = \frac{1}{2}(Ag - ie^{i\omega t}) \cos\gamma^s - 2\zeta f_l (e^{i\omega t} - iAg) \sin\gamma^s + \beta\omega + i\beta\omega A e^{i\omega t} - \omega^2 A e^{i\omega t} - J_{\mathrm{ext}}. \tag{4.22}$$

By separately balancing those terms which are constant, proportional to $e^{i\omega t}$, and proportional to f_l, the Eq. (4.22) is reduced to three coupled equations at a given frequency

$$J_{\mathrm{ext}} = \beta\omega + \frac{\int \mathrm{Re(Ag)} \cos\gamma^s \mathrm{d}\Omega}{2\int d\Omega}, \tag{4.23}$$

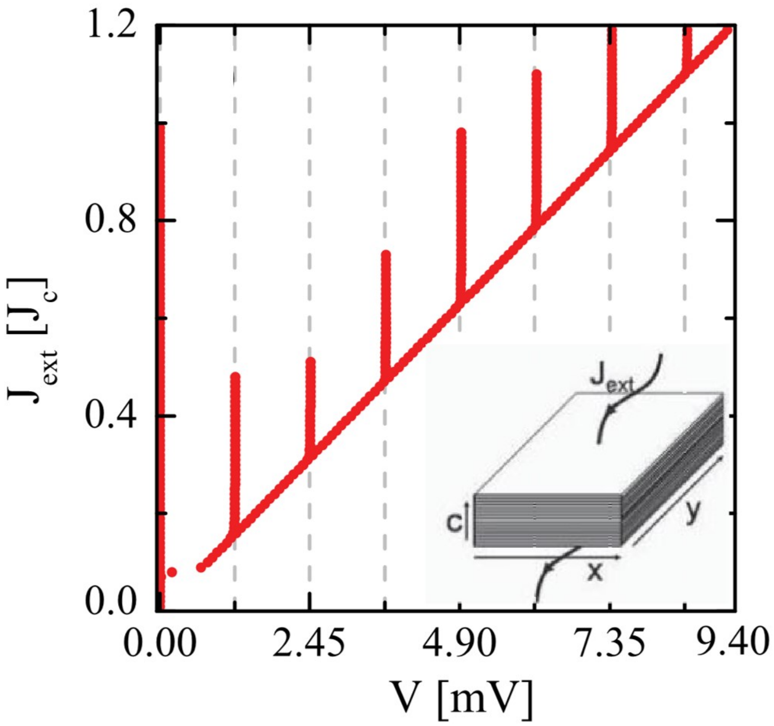

Figure 4.3: Simulated IV characteristics under the perfect magnetic conductor boundary condition for rectangular mesa with $L_x = 80\mu m$ and $\beta = 0.02$. The vertical dashed lines correspond to the voltage at cavity resonances. [After Shizeng Lin and Xiao Hu, Physical Review Letter 100, 247006(2008).]

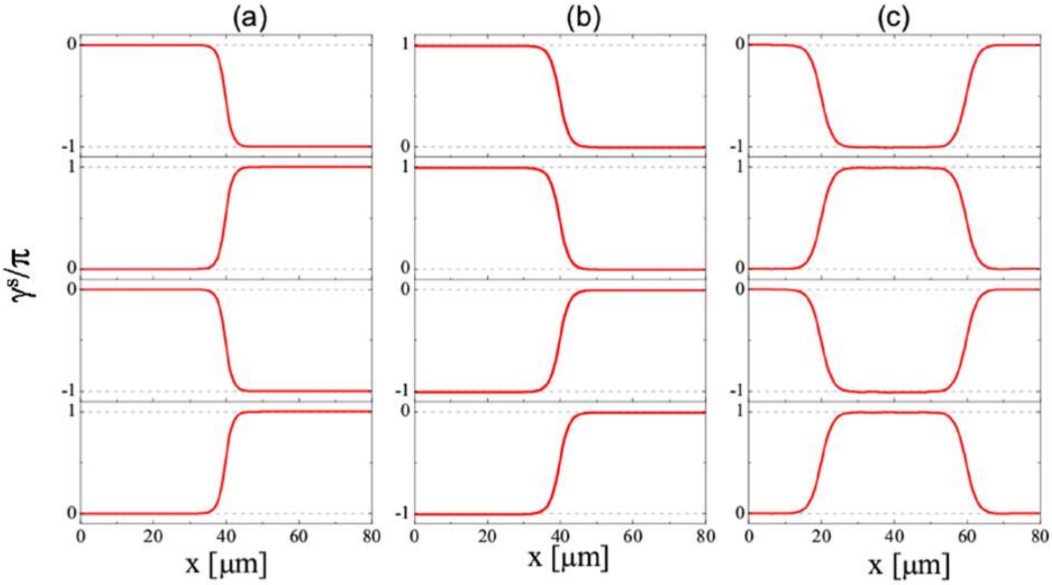

Figure 4.4: Typical configurations of the static term in the phase difference: (a) period of 2 layers and (b) period of 4 layers, corresponding to the first current step, and (c) corresponding to the second current step. [After Shizeng Lin and Xiao Hu, Physical Review Letter 100, 247006(2008).]

$$A = \frac{\int g^* \cos\gamma^s d\Omega}{2i(\omega^2 - k^2 - i\omega\beta) \int |g|^2 d\Omega}, \tag{4.24}$$

$$\triangle\gamma^s = 2\zeta \mathrm{Im(Ag)} \sin\gamma^s, \tag{4.25}$$

with the integration over the lateral area of BSCCO mesa. From Eq. (4.25) it is clear that the π phase kink arises at the node of cavity electric field [8, 27].

The I-V characteristic obtained by simulation for rectangular mesa with lateral size 80μm under perfect magnetic conductor boundary condition is shown in Figure 4.3, and the corresponding π phase kink is displayed in Figure 4.4. As seen by Figure 4.3, there are current steps at the cavity frequencies, which indicates that large energy has been pumped into the cavity modes beside the ohmic dissipation and strong radiation can be excepted for this π phase kink state.

The proposal of the π phase kink state arises intense discussions. The stability of the π phase kink solution was studied and it is found that the π phase kink state is stable against various distortions, such as small perturbations both in the lateral direction and stack direction, weak external magnetic field and modulation of critical current [28, 29]. The π phase kink state was also observed numerically in a more realistic model where the effects of normal electrodes and the nearby vacuum environment are taken into consideration with using a multi-scale simulation method [30, 31]. The role of surface impedance for the π phase kink state was investigated, it was found the π phase kink state is even stable for a large impedance $Z = 1$ [32].

4.3.1 Radiation pattern associated with π phase kink state

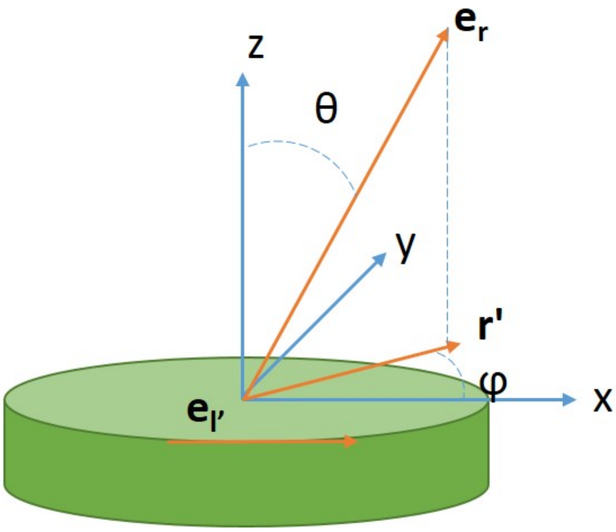

Figure 4.5: Coordinate system for the calculation of radiation pattern.

We calculate the far-field radiation pattern of cylindrical mesa in this subsection, which is useful for applications [37].

To calculate the radiation pattern, we resort to the Huygens principle where the pattern is given by the oscillation of the electromagnetic field at the edges of the samples, which can be calculated equivalently by the edge electric current and magnetic current [89]. The equivalent magnetic current $\mathbf{M}_e$ in the dimensionless units is given by

$$\mathbf{M}_e = \mathbf{E}_e \times \mathbf{n}, \tag{4.26}$$

where $\mathbf{E}_e$ is the oscillating electric field at the edges of BSCCO cylinder and the vector $\mathbf{n}$ is perpendicular to the edges. The coordinates system is plotted in Figure 4.5. As we are focusing on uniform state, $k_\omega = \omega/c$. In this situation, the Poynting vector in the dimensionless unit is

$$\mathbf{S}_= \frac{\omega^2 L_z^2}{32\pi^2\rho^2\varepsilon^{3/2}}|\mathbf{G}|^2\mathbf{e}_r \tag{4.27}$$

with

$$\mathbf{G} = \oint_{\text{edges}} M_e(r')\exp(-i\frac{\omega}{\sqrt{\varepsilon}\mathbf{r}'\mathbf{e}_\mathbf{r}})(\mathbf{e}_\mathbf{r}\times\mathbf{e}_{l'})d\mathbf{l}' \tag{4.28}$$

where the integral is taken over the circumference of the BSCCO cylinder.

For a cylindrical geometry, the oscillation of the electric field in the z direction can be given as

$$E_z = A\omega J_{mn}(k_{mn}\rho)\cos(m\phi). \tag{4.29}$$

Based on Eqs. (4.27) to (4.29) the far-field radiation patterns of cylindrical cavity can be calculated which are displayed in Figure 4.6. For PMC-like (1,1) mode, the radiation power is maximal at the top the cylinder $\theta = 0$, and it has a maximum at y direction while a minimum at the x direction. For the PMC-like (2,1) the radiation power has a minimum at the top of cylinder and maximums at the directions of x and y.

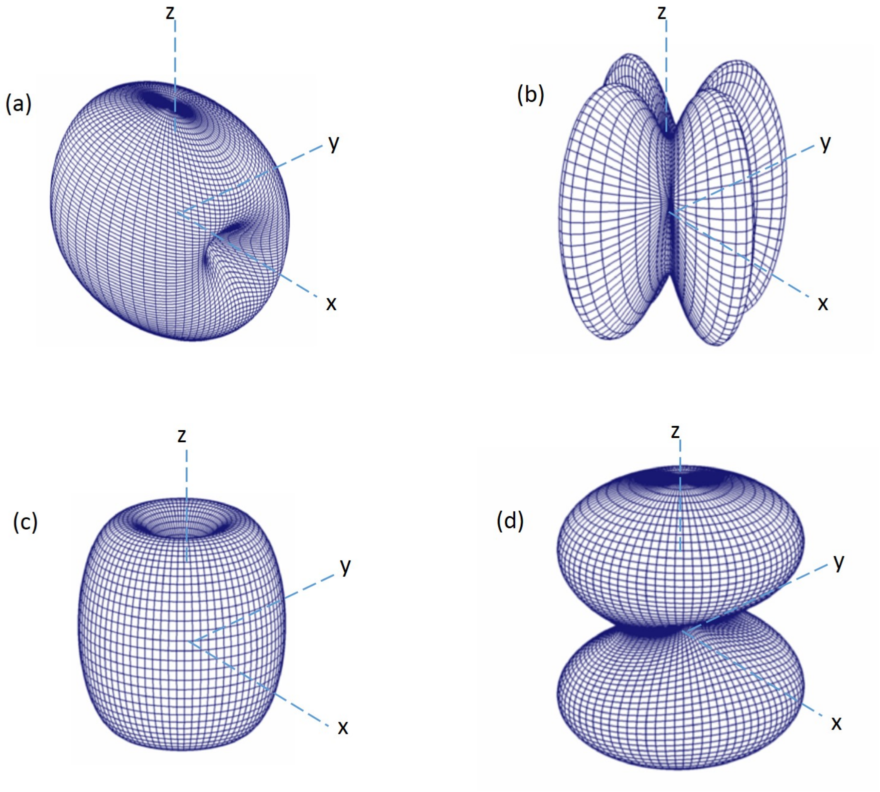

Figure 4.6: Radiation patterns for (a) PMC-like (1,1) mode, (b) PMC-like (2,1) mode, (c)PMC-like (0,1) mode and (d) PMC-like (1,2) mode of cylindrical BSCCO single crystal at the respective resonance frequency. The radius of the cylinder is $100\mu m$.

4.4 Strong radiation with spatial modulations of critical current

Beside the π phase kink state, Koshelev and Bulaevskii [33] proposed that the strong radiation at resonance frequencies can be achieved by introducing spatial modulations of Josephson critical current in IJJs. Decades ago it was first discussed that the inhomogeneity can cause resonance in conventional Josephson junctions [34, 35]. For a uniform state like McCumber state given in Eq. (4.20), the coupled sine-Gordon equations are decoupled and can be written as

$$\partial_t^2\gamma + \beta\partial_t\gamma + g(x)\sin\gamma - J_{\text{ext}} = \partial_x^2\gamma, \tag{4.30}$$

where $g(x)$ is the spatial modulation of Josephson critical current. If we consider the uniform state near the cavity mode $\cos(m\pi x/L_x)$ like

$$\gamma = \omega t + A_0\theta(x)e^{-i\omega t} \tag{4.31}$$

with $\theta(x) = cos(m\pi x/L_x)$, the expression for the amplitude A_0 can be obtained as

$$A_0 = \frac{ig_m}{\omega^2 - k^2 + i\beta\omega}, \tag{4.32}$$

where

$$g_m = \frac{2}{L_x}\int_0^{L_x} dx \cos\left(\frac{m\pi x}{L_x}\right) g(x). \tag{4.33}$$

As seen from Eqs. (4.32) and (4.33), the cavity amplitude A_0 is zero for a uniform critical current, and the spatial modulation of critical current plays a similar role to the π phase kink for pumping energy in this scheme. Similar to the π phase kink state, the dc current with spatial modulation of critical current for McCumber state is given by

$$J_{ext} = \beta\omega + \frac{1}{4}\frac{g_m^2\beta\omega}{(\omega^2 - k^2)^2 + \beta^2\omega^2}. \tag{4.34}$$

Figure 4.7 shows several realizations of spatial modulation of the critical current. To realize the modulation of critical current, one may apply a weak external magnetic field as discussed in Ref. [36].

However, compared with the naturally formed π phase kink state, it is difficult to realize the same spatial modulations of critical current in all the junctions and this mechanism cannot explain the radiation from high cavity modes as the integration in Eq. (4.33) gives zero for high cavity modes. Furthermore, as the equations are decoupled for the solution given by Eq. (4.31), the superconducting phases in different junctions are hard to be synchronized and out-phase state without radiations may develop in this situation.

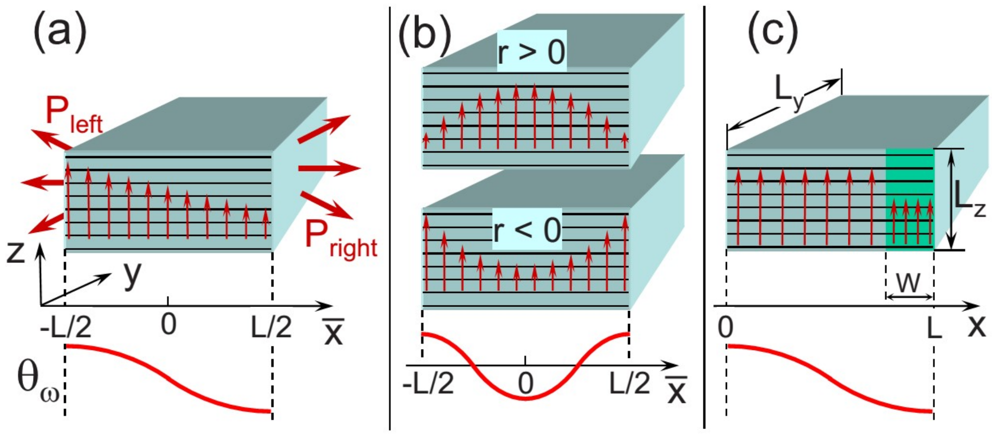

Figure 4.7: Mesas with various modulations of the Josephson critical current density: (a) linear modulation, (b)parabolic modulation, and (c) steplike suppression of the critical current near the edge. the lower plots illustrate the shapes of lowest excited Fiske-resonance modes. [After A. E Koshelev and L. N. Bulaevskii, Phy. Rev. B 77, 014530 (2008)]

5 Synchronization of IJJs

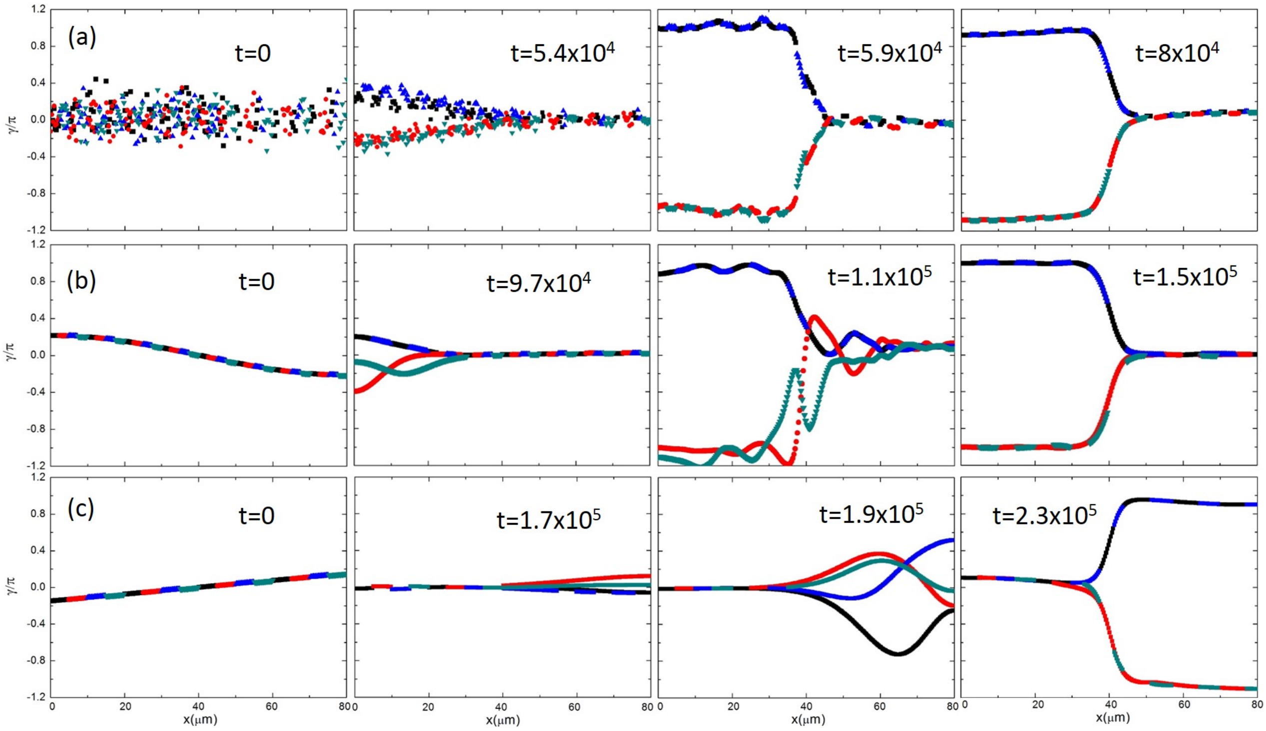

Figure 5.1: Snapshots of simulated phase dynamics starting from initial phase configurations: (a) random distribution with $\sigma = 0.5$; (b) $\gamma_l(x, t = 0) = 0.3\pi \cos(\pi x/L)$ and (c) $\gamma_l(x, t = 0) = 0.28\pi(x/L - 1/2)$. Starting from these three types of phase configurations the system can be driven into the π phase kink state. The blue and the black (the green and the red) colors represent the odd (even) junction indices in c direction. The temporal linear part in phase determined by the bias voltage has been removed for clarity. The bias voltage is set as 1.2mV corresponding to the (1,0) mode. The time is in units of $1/\omega_p$.

The π phase kink state offers us a possible picture for the synchronization of IJJs. However how to drive the system into the π phase kink state efficiently still remains unclear. The observed radiation power in present experiments is not large enough for practical applications, one possible reason is that the system is not driven into a uniform state fully. We propose to synchronize the system to the π phase kink state by preparing initial phases, which can be done by applying non-uniform voltages or making use of thermal fluctuations. Several initial phase configurations are studied, such as random and some typical regular distributions. It is found that the system can be driven into the π phase kink states in several cases. The time before entering the π phase kink states is shorter when the initial phase configuration is further away from uniform phase configuration. The effects of non-uniform distributions of conductance along c direction and critical current on the synchronization of the system are also discussed.

5.1 Random initial phase configurations

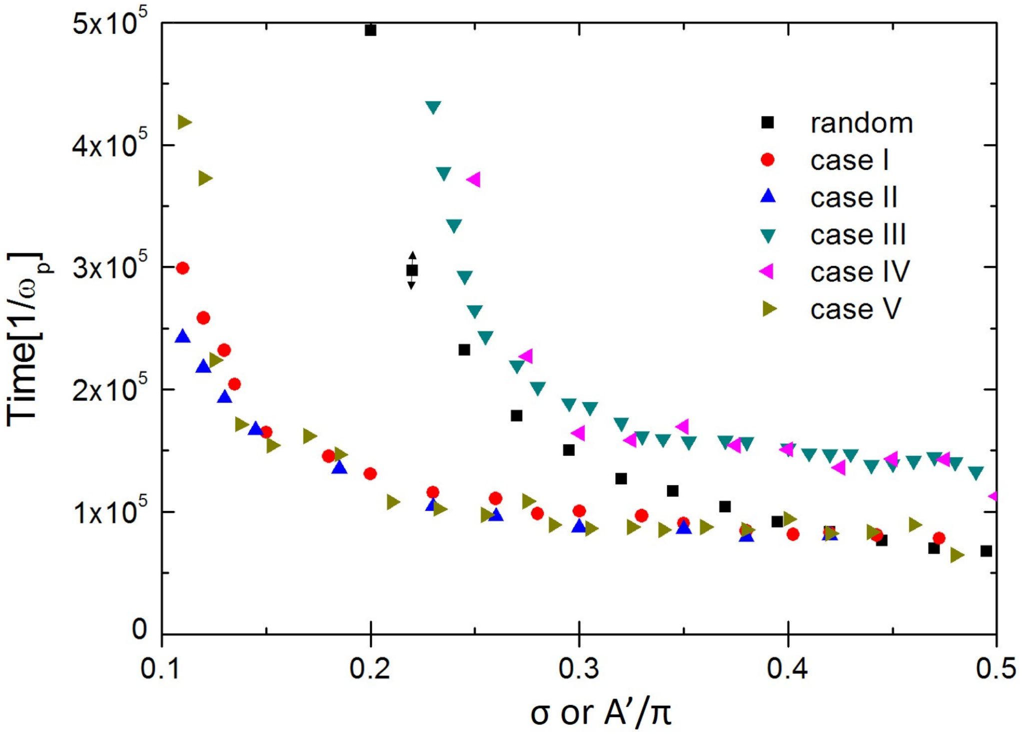

Figure 5.2: Standard deviation σ or amplitude of ordered initial phase configuration A' dependence of time that the system spends before entering the π phase kink state for various initial configurations. For random initial distribution the time is evaluated by averaging on 600 samples and the error bar is about 5%. For distributions of ordered initial phase configuration please refer to the text.

To reveal the phase dynamics of IJJs We resort to computer simulation first and it is performed by integrating Eq. (4.12) with the leapfrog algorithm [8, 27]. Here we focus on the (1,0) cavity mode. A bias current is taken during the simulation. Parameters are taken as: $\zeta = 7 \times 10^4$, $\beta = 0.02$, $\lambda_c = 200\mu m$, $L_x = 80\mu$m, $\varepsilon_c = 16$ and $J_{\text{ext}} = 0.157$ which corresponds 1.2mV near the eigen frequency of (1,0) cavity mode. The initial phase configuration is given randomly between $-\pi$ and π as

$$f(\gamma_l, \sigma) = \frac{1}{\sigma\sqrt{2\pi}} e^{-(\gamma_l/\sqrt{2}\sigma)^2} \tag{5.1}$$

with σ the standard derivation. The simulation snapshots of phase dynamics from random configuration of initial phase is shown in Figure 5.1(a), where one sees that the system can be synchronized into the π phase kink state under the driving of a bias current.

There is another typical state that the system can be driven into, the McCumber state, which is almost a uniform state and no cavity resonance phenomena can be expected as discussed above. To understand the relation between the initial phase configuration and the final stable state, we investigate 600 independent samples and then count the time that the system spends before entering the π phase kink state. The criterion for formation of the π phase kink state is that there should be $(2n + 1)\pi$ phase kinks in the phase at the nodes of the electric field in c direction with n an integer. For the initial configurations with which the system falls into the McCumber state, the consuming time is taken as infinitely long. The average time that the system spends before entering π phase kink states is displayed in Figure. 5.2 when the standard deviation σ is varied. As one can see from Figure 2, the average time is shorter when σ is larger, which suggests thermal fluctuations can help synchronize the system.

5.2 Typical ordered initial phase configurations

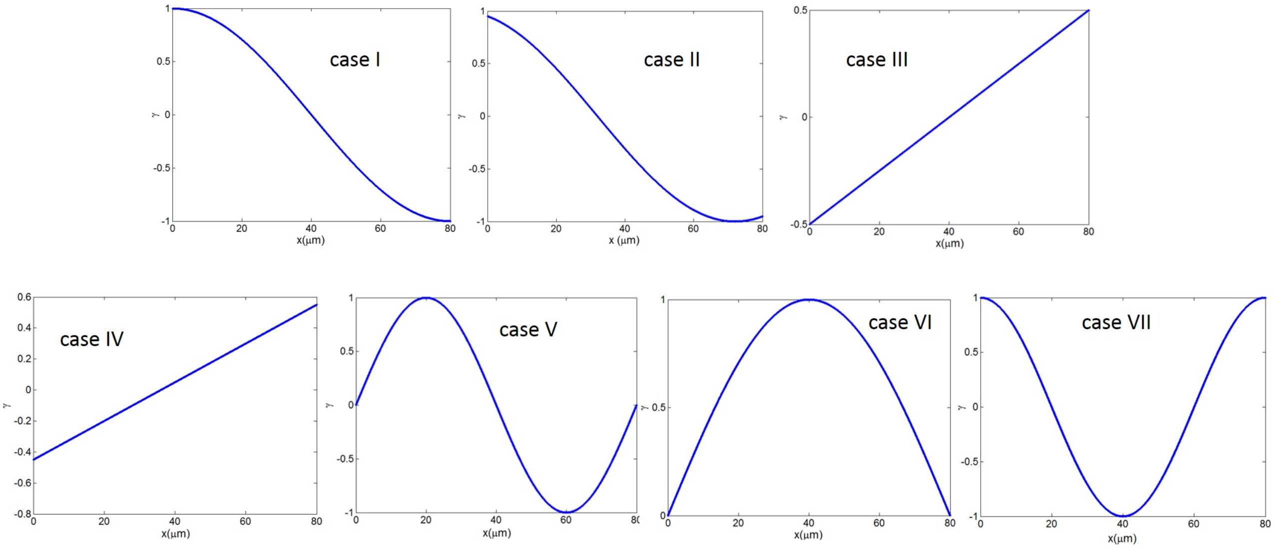

Figure 5.3: Several typical ordered initial phase configurations.

In order to make comparison, several typical ordered initial phase configurations are also studied, such as case I: $\gamma_l(x, t = 0) = A' \cos(\pi x/L_x)$; case II: $\gamma_l(x, t = 0) = A' \cos(\pi x/L_x + 0.1\pi)$; case III: $\gamma_l(x, t = 0) = A'(x/L_x - 1/2)$; case IV: $\gamma_l(x, t = 0) = A'(x/L_x - 0.45)$ and case V: $\gamma_l(x, t = 0) = A' \sin(2\pi x/L_x)$. It is found that in all these cases, the system can be driven into the π phase kink state for large enough amplitudes. The minimal amplitude for case I is 0.11π, for case II is 0.1π, for case III is 0.23π, for case IV is 0.21π and for case V is 0.11π. Several snapshots of phase for $A' = 0.3\pi$ of case I and for $A' = 0.28\pi$ of case III are shown in Figure 5.1(b) and (c) respectively. The time spent before entering the π phase kink state is shown in Figure 5.2 when the amplitude A' is varied.

Some other ordered initial phase states are also studied such as case VI: $\gamma_l(x, t = 0) = A' \sin(\pi x/L_x)$ and case VII: $\gamma_l(x, t = 0) = A' \cos(2\pi x/L_x)$. We find that in these two cases, the system cannot be driven into the π phase kink states. This is because of that the distributions of phases in cases VI and VII are similar to the $(2, 0)$ mode, and thus the energy cannot be pumped into the system at the (1,0) mode frequency given by the bias voltage. The initial phase configurations for different ordered state are plotted in Figure 5.3.

5.3 Effects of non-uniform distributions of conductance and critical current

As the radiation happens at the place where Joule heating is sever, the thermal effects may play an important role in the synchronization of the system. Especially at the center of mesa, due to the injection of external current and the bad heat removal condition of the experimental setup, hot spot forms near the center of sample. In this situation, the properties of the BSCCO mesa like conductance and critical current density are not spatially uniform any more, one need to take the non-uniform distribution of these quantities into consideration. Here we set several typical distributions of conductance, which is shown in Figure 5.4. Then we count the possibility of entering the π phase kink state from different random initial phase configurations for these typical non-uniform conductance distributions. The result is displayed in Figure 5.5, one sees that when the distribution of conductance is similar to the corresponded π phase kink like the half case, the possibility of entering the π phase kink state is higher than other distributions, which suggests that the local thermal effects play an positive role in the synchronization of the system if one can control the hot spot in a proper position.

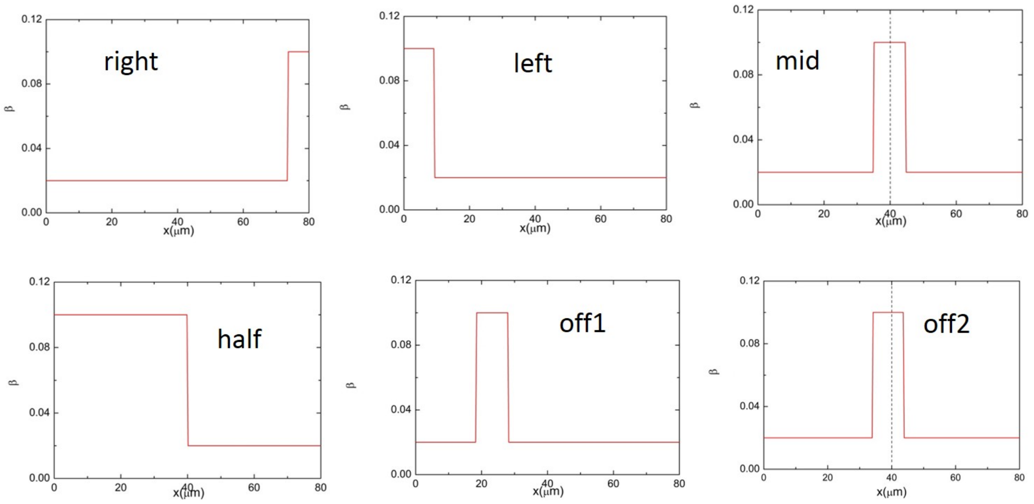

Figure 5.4: Several typical non-uniform distributions of conductance $\beta(x)$ along c direction.

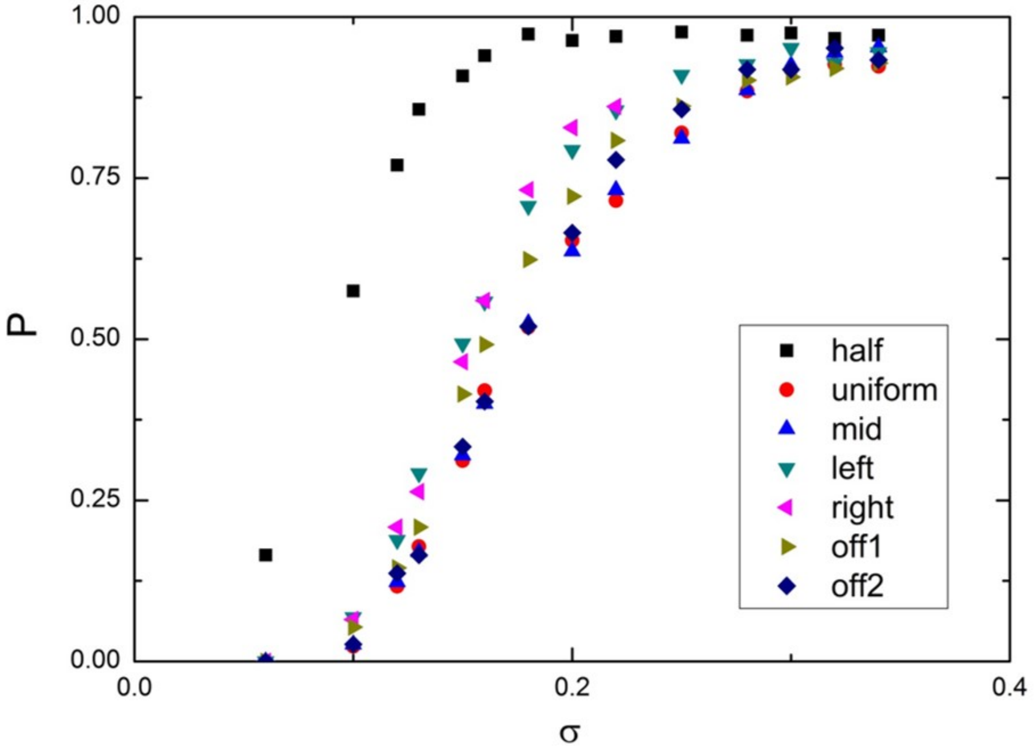

Figure 5.5: Probabilities of entering the π phase kink state (first mode) with different $\beta(x)$s from initial states in Gaussian distribution. σ is the standard deviation, the sample number N=600 with a error bar about 5%. When $\beta(x)$ is closer to the corresponded π phase kink state, the positive effect is more obvious.

Another quantity affect by the hot spot is critical current density. For critical current density we consider two kinds of distributions which are shown Figure 5.6(a) and (b). We focus on their effects on I-V characteristics which is displayed in Figure 5.6(c), where they coincide well with the uniform case.

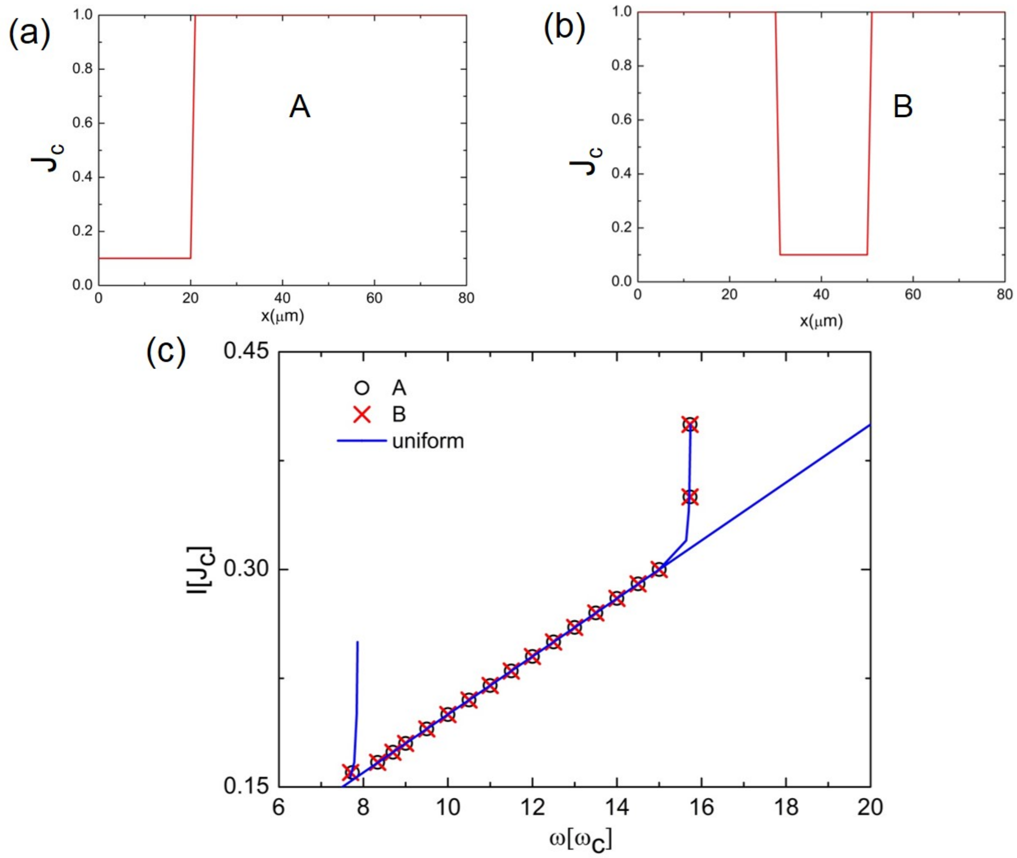

Figure 5.6: (a) and (b) Two kinds of non-uniform distributions of critical current density; I-V characteristic for non-uniform and uniform distributions of critical current. These three cases coincides well with each other.

5.4 Comparisons with experimental results

In above discussion, we find that the system can be driven into the π phase kink state from a random initial phase configuration and the consuming time for entering the π phase kink state is shorter if the standard deviation of the random configuration is larger. As a larger standard deviation corresponds to a higher temperature of the system, this result suggests that the thermal effects play a positive role during the synchronization process of IJJs. Several experiments also explore the thermal effects on the THz radiation from IJJs and it is meaningful to compare our simulation result with the experimental ones. Kakeya *et al*. investigated the THz radiation from the BSCCO mesas with thick (400 nm) and thin (<100 nm) electrodes and they found that only for the sample with thin electrodes the THz radiation could be detected, which suggests that the thin electrodes help excite the Josephson plasma as a result of the poor heat flow through the thin electrodes [45]. Comparing with our simulation result, the samples with thick and thin electrodes correspond the random initial phase configurations with small and large σs in our simulation. As one sees from Figure 5.2, the system is difficult to be driven into the π phase kink state especially $\sigma < 0.2$, which is consistent with Kakeya's experimental result that no radiation can be detected for samples with thick electrodes. Another interesting experiment is to tune the emission power from IJJs with a focused laser beam. Figure 5.7 displays the experimental data for the emission powers when the laser beam focus on different position of the sample [47]. As one sees from

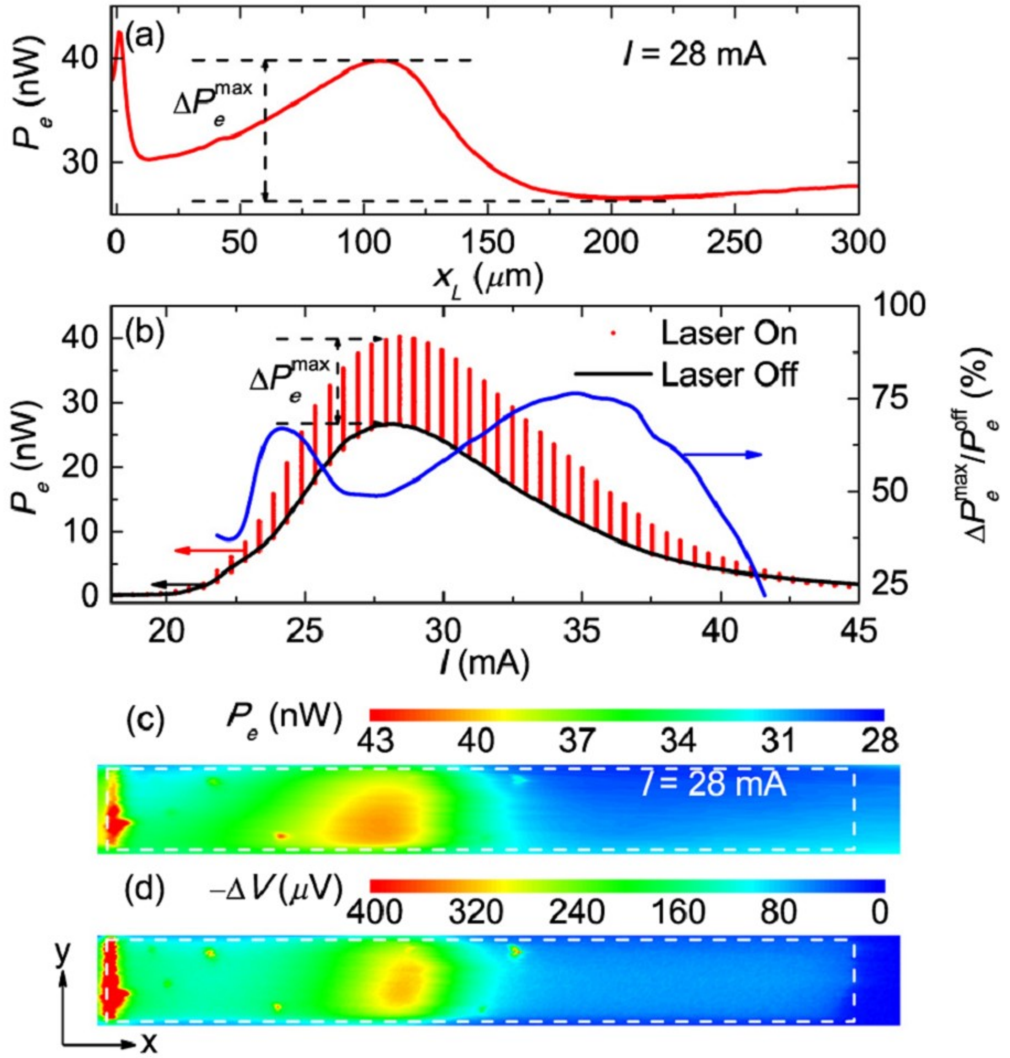

Figure 5.7: (a) Emission power with laser positioned at coordinate x_L for a bias current of 28 mA. (b) P_e vs bias current while sweeping the laser, for discrete values of I, from $x_L = 10\mu$m to $x_L = 300\mu$m (left scale). The black line indicates P_e^{off} vs I, as measured for the laser turned off; thus, the vertical red lines indicate, for each current, the maximum laser-induced change $\Delta P_e^{\max}$. Right-hand scale, blue curve: ratio $\Delta P_e^{\max} = P_e^{\text{off}}$ vs I. For $I = 28mA$, (c) shows a 2D plot of P_e vs laser position $(x_L; y_L)$ and (d) shows a 2D LTSLM image $-\Delta V$ vs $(x_L; y_L)$. In (c) and (d), the boundaries of the stack are indicated by the dashed boxes. The bath temperature is 22 K. [After Zhou *et al.*, Phys. Rev. Apl. 3, 044012 (2015)]

Figure 5.7, the emission power is enhanced when the laser is on due to increasing of the average temperature of the sample and the emission power is enhanced most when the position of the laser beam is close to the middle of BSCCO sample ($x_L = 145\mu$m). From Figure 5.7 (d) we see that this most enhanced case is actually similar to the π-phase-kink-like distribution (half case) of non-uniform conductivity in our simulation as displayed in Figure 5.4, where the non-uniform distribution of conductivity in half case improves the possibility of the junctions entering the phase kink state from random initial phase configuration. For example the possibility of entering the π phase kink state for $\sigma = 0.2$ is increasing from 0.63 to 0.9 from the uniform case to the half case and the radiation power in the experiment is enhanced from 26nW to 42nW when the laser is focused on the different locations of the sample for bath temperature near 22K [47].

6 General solution at small and medium inductive couplings

In above discussion, the phase dynamics of IJJs associated with the π phase kink state is discussed. One necessary condition for the establishment of alternating π phase kinks is the large inductive coupling among junctions, which is usually of order of 10^5. The large inductive coupling requirement narrows one's vision for choosing potential materials for powerful THz radiation and the study of phase dynamics in IJJs for small and medium inductive couplings is desirable. As discussed in what follows, a general solution valid for high cavity modes and weak or moderate inductive couplings is proposed based on numerical simulation and analytical analysis [50]. This new solution develops a structure in form of cavity mode in lateral directions and characterized by an alternating configuration in c direction similar to the π phase kink. The present state can enhance dc energy injection into the system at cavity resonance and convert it to EM radiation. Increasing the inductive coupling, this new solution evolves into the π phase kink state smoothly.

6.1 General solution

To reveal the phase dynamics of IJJs at small and medium inductive couplings, computer simulation of Eq. (4.12) is performed. Initial phase difference is assigned between $-\pi$ and π randomly in the in-plane directions and over all junctions. The parameters for the simulation are taken the same as those in Figure 4.3 except for that a medium $\zeta = 230$ is used here. The simulation result for cavity (1,0) mode is shown in the first column of Figure 6.1 by the black square.

Similar to the case of strong inductive coupling, the solution of Eq. (4.12) at small and medium values of ζ can be summarized into an identical form as Eq. (4.21). The difference focus on the static term γ^s, whose equation is given as

$$\partial_x^2 \gamma^s(x) = 2\zeta' \cos\left(\frac{n\pi x}{L_x}\right) \sin\gamma^s(x), \tag{6.1}$$

where $\zeta' = \zeta A \cos\varphi$. The solution of Eq. (6.1) is plotted in Figure 6.1 for a moderate inductive coupling $\zeta' = 198$ and several typical cavity modes. One finds that to a good approximation, the static γ^s term can be written as

$$\gamma^s(x) = \frac{\pi}{2} - B\cos\left(\frac{n\pi x}{L_x}\right), \tag{6.2}$$

where B is to be determined.

Substituting Eq. (6.1) into Eqs. (4.24) and (4.25) one arrives at

$$A = \frac{2J_1(B)}{\sqrt{(\beta\omega)^2 + (\omega^2 - k^2)^2}}, \tag{6.3}$$

$$Bk^2 = 2\zeta A \cos\varphi[J_0(B) - J_2(B)], \tag{6.4}$$

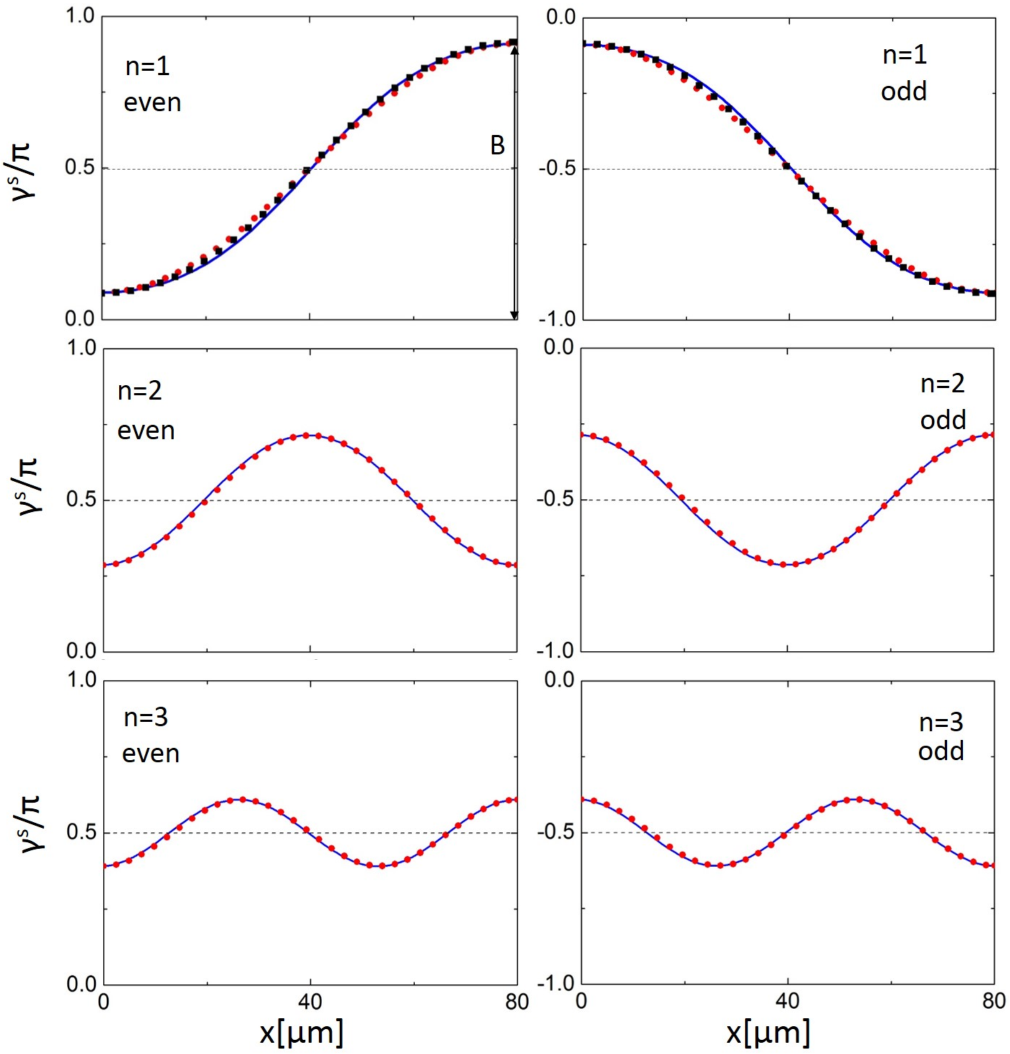

Figure 6.1: Static term γ^s in solution (4.21) at moderate inductive coupling and several cavity modes with left/right row for the junction with even/odd index. Red dot is the numerical result of Eq. (6.1) with $\zeta' = 198$, blue solid curve is the analytic solution given in Eq. (6.2) with $B = 0.41\pi$, 0.21π and 0.11π for $n = 1$, 2 and 3 respectively, and black square is the simulation result of Eq. (4.12) with $\zeta = 230$ and $J_{\text{ext}} = 0.16$ for the (1,0) cavity mode. Other parameters are taken same as those of figure 1. These three solutions are in good agreement with each other and the differences among them are less than 3% in the whole space.

where $k = n\pi/L_x$ is the cavity wave number and $\tan\varphi = \beta\omega/(\omega^2 - k^2)$.

Solving Eqs. (6.3) and (6.4) one obtains the inductive coupling ζ and frequency ω dependencies of A and B defined in Eqs. (3) and (23) for the (1,0) cavity mode, which is displayed by Figure 6.2. As seen from Figure 6.2, A and B grow continuously from zero at a bifurcation point of the system. Below this point, the system takes the McCumber state [8]. Simultaneously with Eqs. (6.3) and (6.4) one obtains the external current analogous to Eq. (4.25) [8,27]

$$J_{\text{ext}} = \beta\omega + \frac{A\sin\varphi}{2L_x}\int_0^{L_x}\cos(kx)\cos\gamma^s dx. \tag{6.5}$$

It is clear that the cavity mode and the uniform external current are coupled by the γ^s term, a scheme akin to the π kink state. The I-V characteristics of the present solution is plotted in Figure 6.3 for $\zeta = 230$, where large supercurrent flows into the system at the resonance voltage of (1,0) cavity mode $\omega_{\text{cav}} = 7.85$ which corresponds

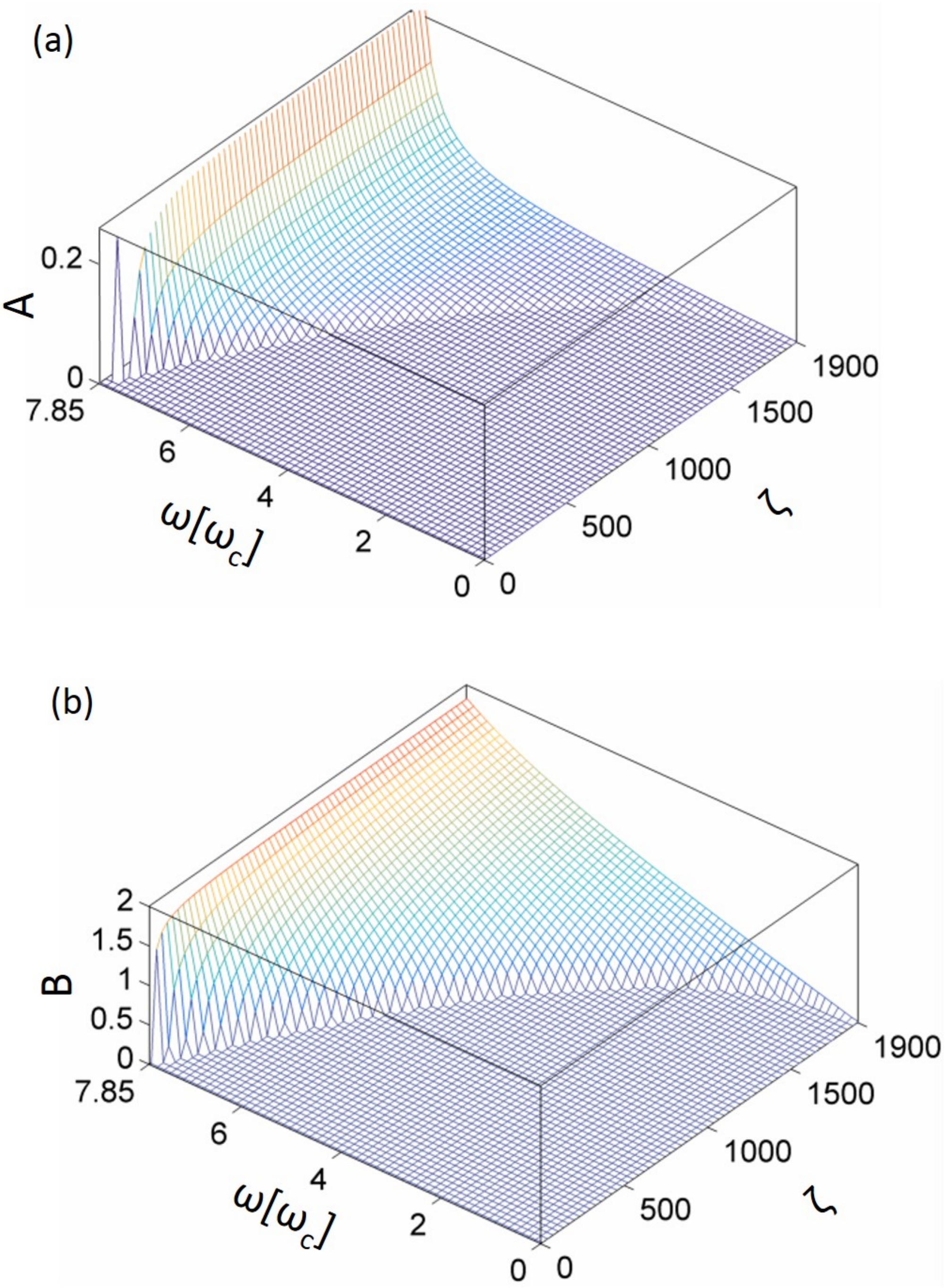

Figure 6.2: (a) and (b): Inductive coupling ζ and frequency ω dependencies of A and B defined in Eqs. (4.12) and (6.2) for the (1,0) cavity mode. Parameters are taken same as those in Figure 6.1.

to 1.2mV. Thus, this state is expected to be useful for the realization of powerful radiation. The detailed shape of I-V characteristics does not depend on the value of ζ sensitively.

6.2 Relation with the π phase kink state

There are many similarities between the π phase kink state and the present state. One may naturally ask the the relationship between them. To answer this, the typical length of π phase kink is estimated. From Eq. (6.1) the

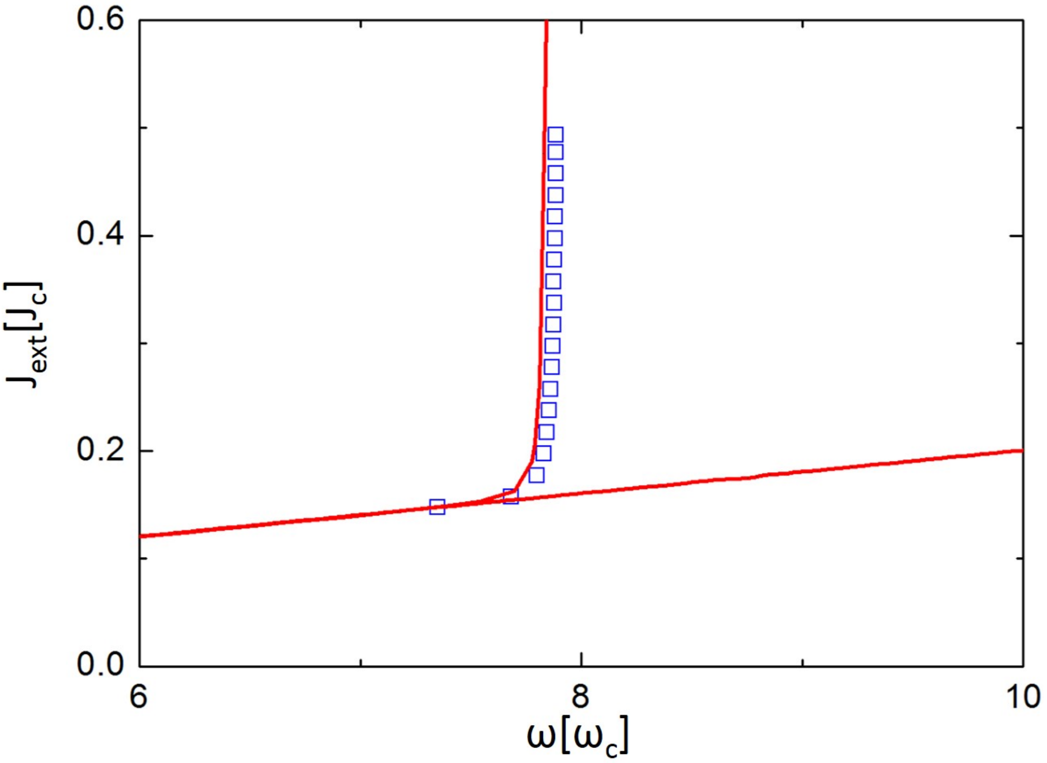

Figure 6.3: I-V characteristics of the (1,0) cavity mode for $\zeta = 230$. Solid curve represents the analytic result of Eqs. (6.3) to (6.5) and square is the simulation result of Eq. (4.12). Other parameters are taken same as those in Figure 6.1.

typical length of the π phase kink state is obtained as

$$\lambda_\pi = \left(2\zeta' \frac{n\pi}{L_x}\right)^{-1/3}. \tag{6.6}$$

When $n\pi\lambda_\pi > L_x$ the lateral size of IJJs cannot hold enough π kinks for the corresponding cavity mode. Rephrasing this condition in terms of ζ' and n based on Eq. (6.6)

$$2\zeta' < \left(\frac{n\pi}{L_x}\right)^2, \tag{6.7}$$

it becomes clear that when the inductive coupling is small and/or the cavity mode is high, the π phase kink state becomes unstable. In this case the π phase kink state deforms into the present state, where the the static phase term does not reach π and 0 at sample edges.

In Figure 6.4 the magnetic energy per junction given as $E_{B_s} = \left\langle \partial_x \boldsymbol{\gamma}^{sT} \mathbf{M}^{-1} \boldsymbol{\gamma}^s \right\rangle_x /N$ with $\boldsymbol{\gamma}^s = \gamma^s \mathbf{I}_2$ and N the number of junctions is plotted for ζ ranging from 10 to 10^5. One sees that the static magnetic energy is $E_{B_s} \sim 1/\sqrt{\zeta}$ in the whole range of ζ, which suggests that the present state continuously evolves into the π phase kink state as ζ increases. As a matter of fact, when the inductive coupling ζ increases from 10 to 10^5, the γ^s term evolves into the π phase kink gradually as seen in the inset of Figure 6.4.

6.3 Other cavity modes

So far we concentrate on (1,0) cavity mode. One can extend the discussion to other cavity modes. Here we show (1,1) mode in a rectangular mesa as an example. Based on simulation on Eq. (4.12), the γ^s term for (1,1)

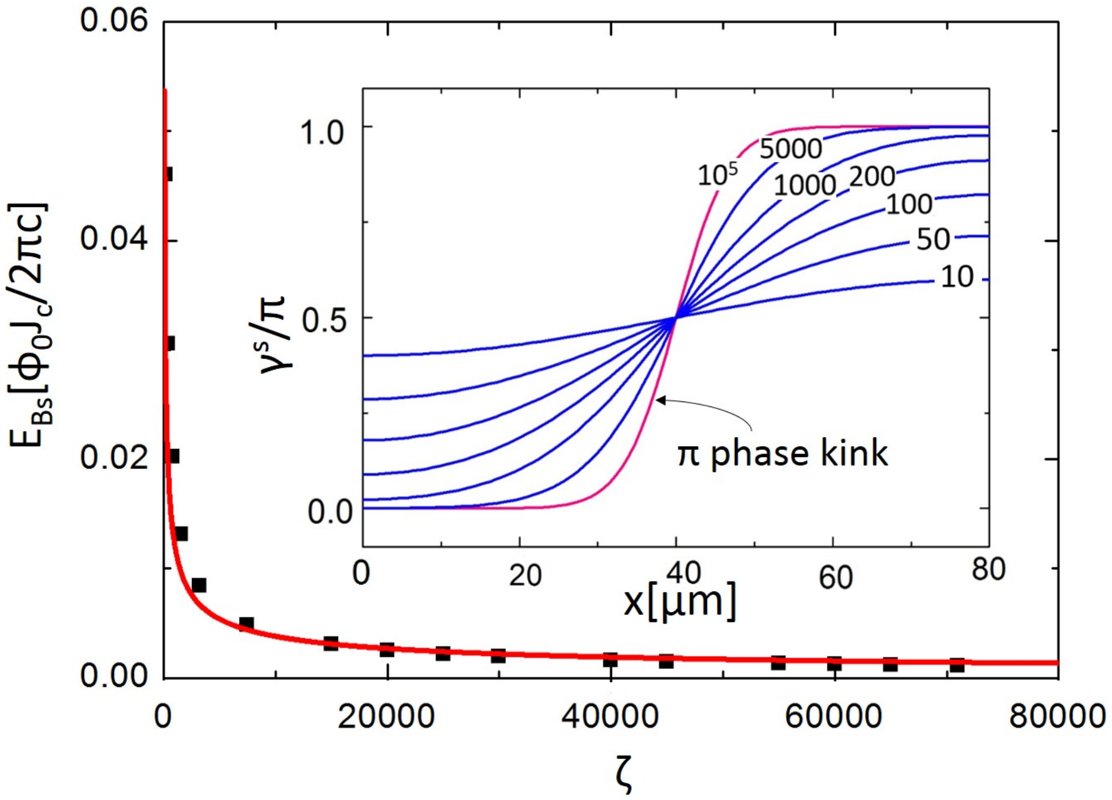

Figure 6.4: Inductive coupling ζ dependence of static magnetic energy E_{Bs} obtained by the simulation on Eq. (4.12) at $J_{\mathrm{ext}} = 0.4$. The red curve is for $E_{\mathrm{Bs}} \sim 1/\sqrt{\zeta}$. The inset shows the evolution process of the present state to the π phase kink state when the inductive coupling ζ increases obtained by the simulation of Eq. (4.12). Other parameters are taken same as those in Figure 6.1.

cavity mode can be written as

$$\gamma^s = \frac{\pi}{2} - B\cos\left(\frac{\pi x}{L_x}\right)\cos\left(\frac{\pi y}{L_y}\right), \tag{6.8}$$

where $L_y = 200\mu m$ is the mesa size in y direction. The term $\gamma^s(x, y)$ and I-V characteristics of the (1,1) mode are displayed in Figure 6.5. For clarity we only show the simulation result of Eq. (4.12) for $\zeta = 230$ and $J_{\mathrm{ext}} = 0.19$, noticing that the differences among simulation result of Eq. (1), numerical solution of Eq. (3) for $\zeta' = 198$ and the analytic solution Eq. (6.2) with $B = 0.46\pi$ are less than 5% in the whole space.

6.3.1 Cylindrical geometry

One can also extend this general solution to other geometry like cylindrical mesa. As the distribution of EM standing wave can be observed directly in experiments [86], we plot them out explicitly for the lowest two cavity modes of cylindrical mesa. The eigen mode (m,n) of cylindrical mesa is given as the first kind Bessel function $J_m(\chi_{mn} r/R_0)\cos(m\varphi)$. The distributions of static phase, supercurrent, the spatial part of the oscillating electric and magnetic field for (1,1) mode of cylindrical mesa are displayed in Figure 6.6 with radius of cylinder $R_0 = 100\mu m$. As seen by Figure 6.6, the magnetic field is always zero at the edge of cylinder, which is imposed by the boundary condition. The electric field takes its maximal absolute value at the left- and right-most parts, while is reduced to zero along the diameter at $\varphi = \pm\pi/2$. For the distribution of supercurrent it is positive over the cylinder as the associated cavity mode and the γ^s term are coupled together, which permit large external

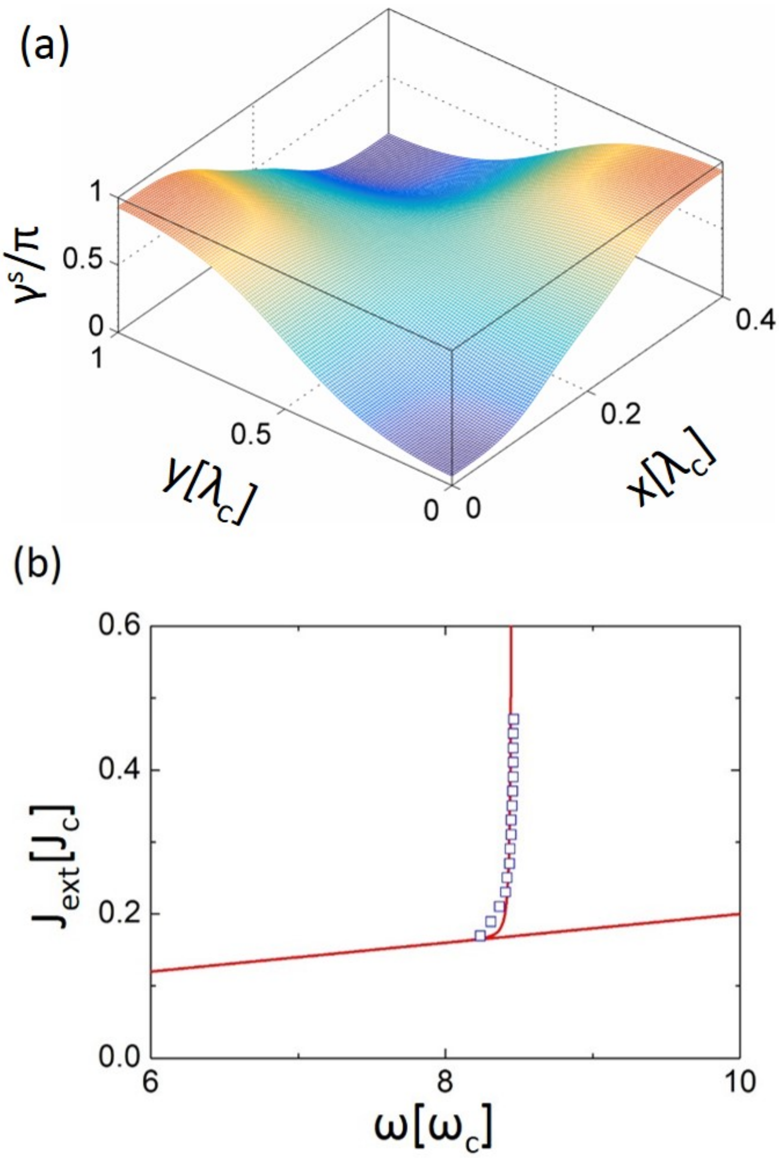

Figure 6.5: (a): Spatial distribution of γ^s term for (1,1) cavity mode given by the simulation on Eq. (4.12) for $J_{\text{ext}} = 0.19$; (b): I-V characteristics of the (1,1) cavity mode. Solid curve represents the analytic result of Eqs. (5) to (7) and square is the simulation result of Eq. (4.12). Here $\zeta = 230$, $L_y = 200\mu m$, and other parameters are taken same as those for Figure 6.1.

current when the system is at resonance frequency. For cylindrical (1,1) mode the wave number $\chi_{11} = 1.84$. Figure 6.6 displays the electric and magnetic field, the static γ^s term and the supercurrent distributions of (2,1) mode for cylindrical mesa. For (2,1) cylindrical mode, the magnetic field penetrates into the cylinder along two directions, $\varphi = 3\pi/4$ and $\varphi = -\pi/4$, and flows away along the two orthogonal directions, $\varphi = \pi/4$ and $\varphi = -3\pi/4$, where the absolute value of magnetic field assumes its maximum. The electric field and the supercurrent become maximall at the directions of multiples of $\varphi = \pi$'s. The (2,1) mode for cylinder geometry looks similar to the (1,1) mode of rectangular geometry. For (2,1) mode of cylindrical mesa $\chi_{21} = 3.05$.

The I-V characteristics of cylindrical mesa can be obtained by solving Eq. (4.23) to Eq. (4.25) numerical, which are shown in Figure 6.8 for the cavity (1,1) and (2,1) modes. As seen by Figure 6.8, there are two large currents step at the cavity resonances of cylinder, which suggests large supercurrent is pumped into the system

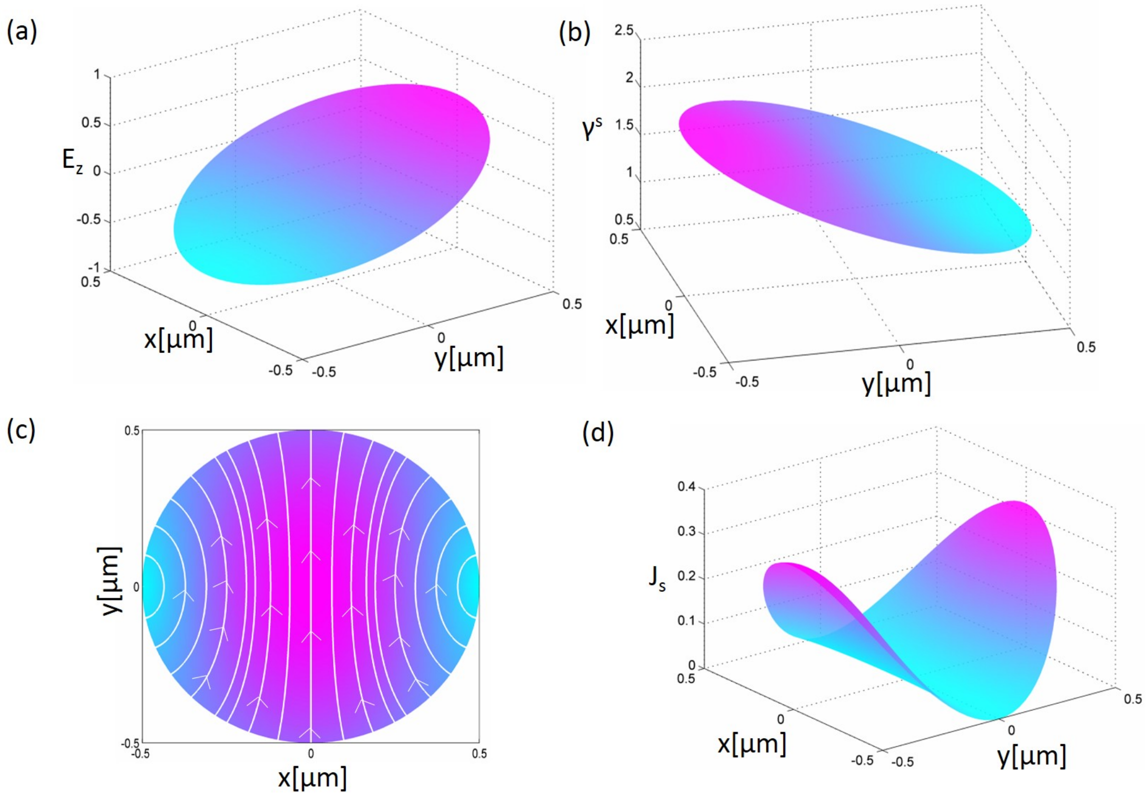

Figure 6.6: Spatial distribution of (a) standing electric field, (b) the static phase term γ^s, (c) the magnetic field and (d) the supercurrent for the (1,1) mode of cylindrical mesa. Here $\zeta' = 200$ is taken for Eq. (4.25). The lateral coordinates are normalized by the radius of the cylinder. The quantities except the phase difference γ^s are up to the plasma amplitude A.

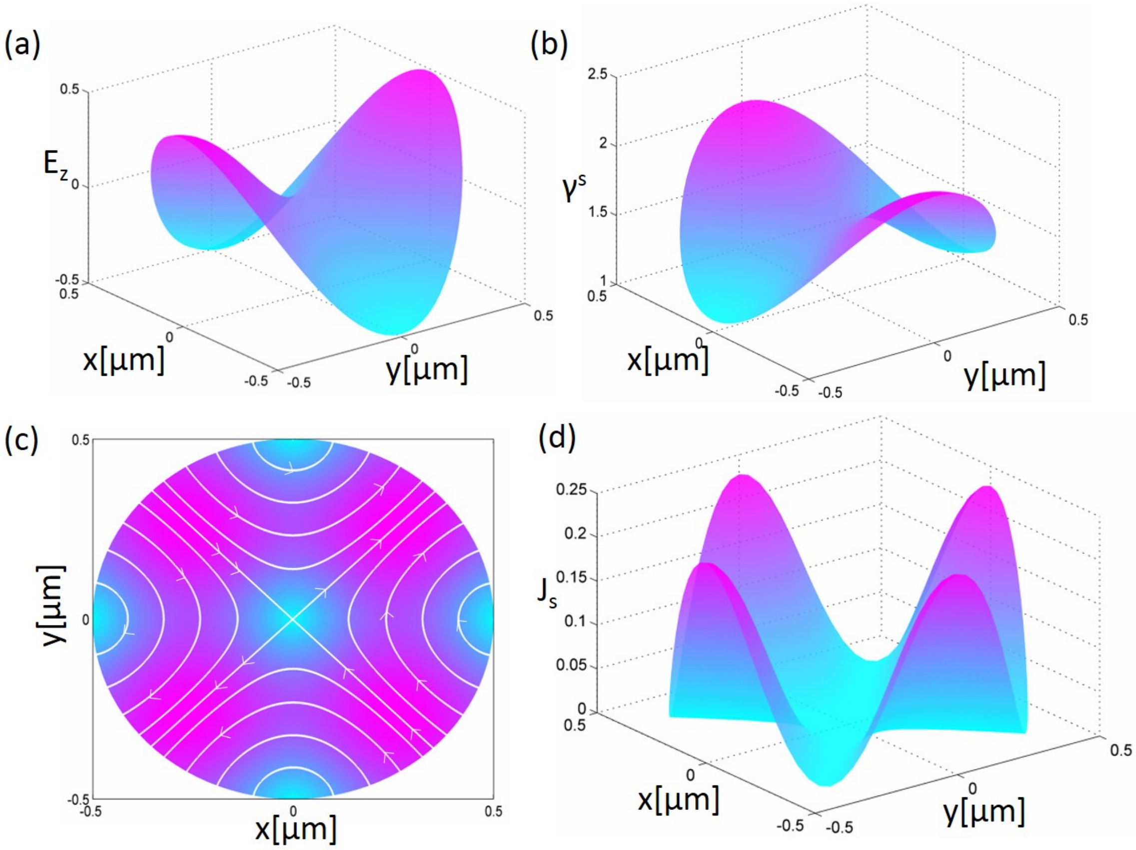

Figure 6.7: Same as Figure 6.6 for the (2,1) mode of cylindrical mesa.

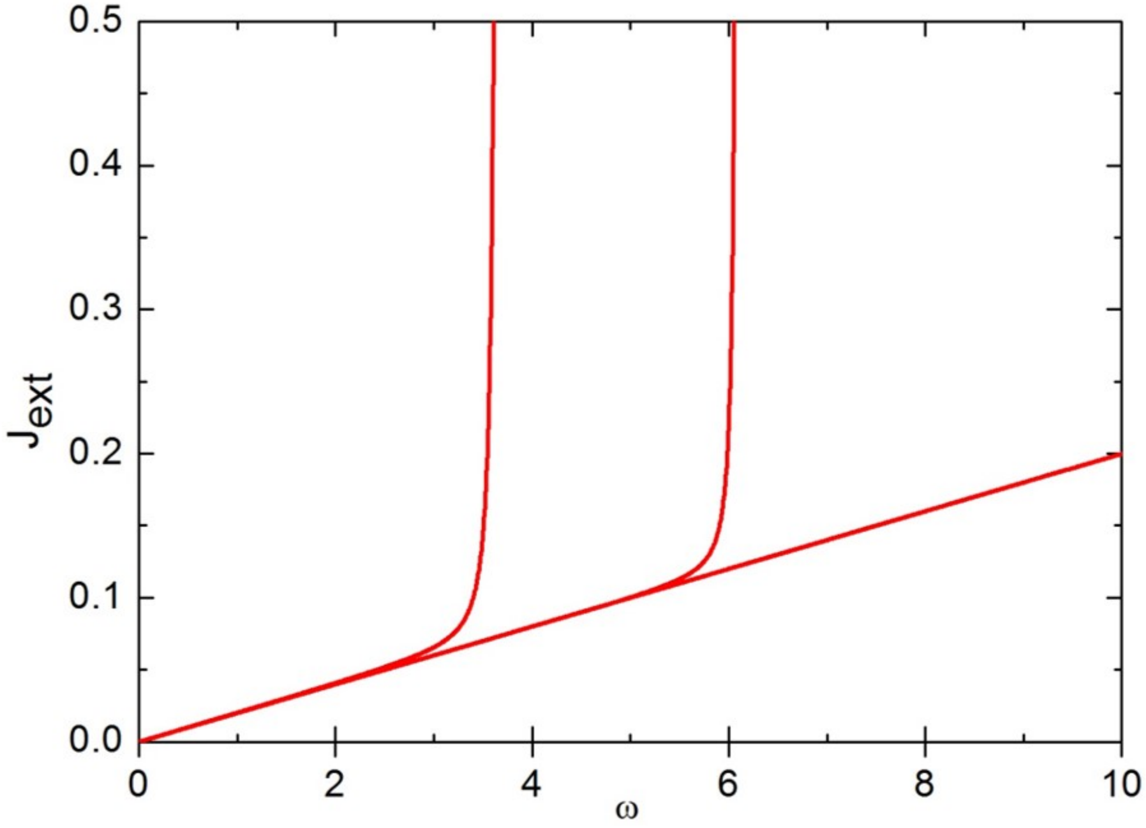

Figure 6.8: I-V characteristic for the cylindrical mesa including the two lowest modes. The dimensionless or equivalently the wave number and frequency, is given by $\omega = \chi/R_0$ with $\chi = 1.84, 3.05$ for the (1,1) and (2,1) mode respectively. The radius of the cylinder $R_0 = 100\mu m$.

and strong radiation can be expected.

6.4 Comparison with the breather solution

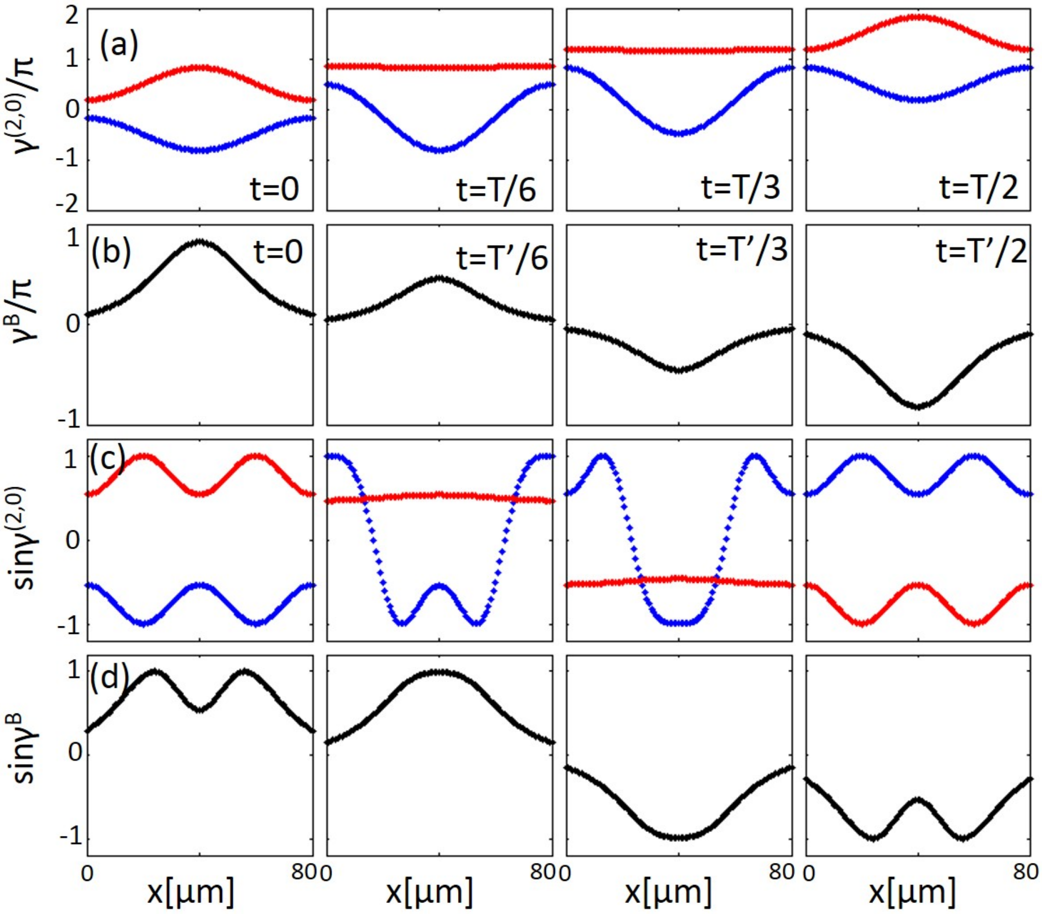

Figure 6.9: (a) and (b): Snapshots of time evolution of the present state for (2,0) cavity mode and breather state in a half period respectively, the red/blue color represents the junction with even/odd index in the c direction; (c) and (d): snapshots of time evolution of $\sin\gamma$ for (2,0) cavity mode and $\sin\gamma^B$ respectively in a half period. Here $T = 2\pi/\omega$ with $\omega = 15.7$ and $T' = 2\pi/\omega'$ with $\omega' = 0.8$.

Krasnov studied the phase dynamics of IJJs especially for high cavity modes and discussed that a breather-like solution may be stabilized. [84] Here we discuss the relation between the present solution and the breather solution [85]

$$\gamma^B = 4\text{atan}\left[\frac{\sqrt{1-\omega'^2}\cos\omega' t}{\omega'\cosh(\sqrt{1-\omega'^2}x)}\right] \tag{6.9}$$

with $\omega' \leq 1$. Compared with the present solution discussed above, first we notice that the frequency ω' in breather solution has a different meaning, which is determined by the eigen values of related inverse scattering problems to the sine-Gordon equation [85], and not directly related to the applied voltage like ω in the present solution. Secondly the peak value of the breather solution becomes smaller when ω' is approaching unity, while in the present solution both the amplitudes of cavity mode and static term become larger when ω is closer to the resonance one. The snapshots of time evolution of present solution for (2,0) cavity mode, γ^B, $\sin\gamma$ for

(2,0) cavity mode and $\sin \gamma^B$ are shown in Figure 6.9 in half period. To make the comparison apparent, we set the maximal value of breather solution similar to the one of present solution for (2,0) cavity mode near resonance by choosing $\omega' = 0.8$ in Figure 6.9. As seen in Figure 6.9(a) and (b), although the even branch of present solution and breather solution have a similar shape at $t = 0$, they become different during the time evolution, for example the even branch of present solution becomes flat at $t = T/6$ and $t = T/3$ while the shape of breather solution remains domed at $t = T'/6$ and $t = T'/3$. For the supercurrent distributions of the present solution and breather solution displayed in Figure 6.9(c) and (d), we can see that although the supercurrent of breather solution has a similar shape to the supercurrent of even branch of the present solution at $t = 0$ and $t = T/2$ ($t = T'/2$), their time evolutions are different. According to our study, what was seen in simulations by Krasnov [84] is actually the solution revealed in the present work.

7 Optimal Condition for Strong Radiation from IJJs

7.1 Proposed device

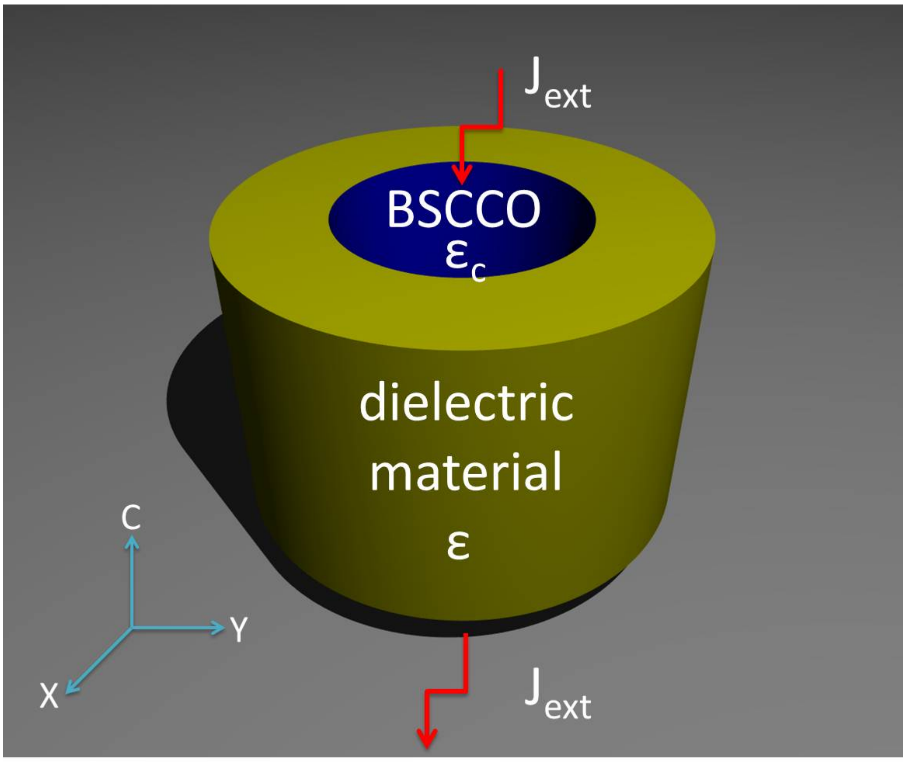

Figure 7.1: Schematic view of proposed device with a thick BSCCO cylinder embedded in a dielectric material. The surrounding dielectric material is considered as infinitely thick.

Even with the novel π kink state, the radiation power based on IJJs is still not sufficient due to the small radiation area limited by the mesa thickness ($\sim 1\mu m$), and enhancement of the radiation power remains a problem. Here we propose to use a long cylindrical BSCCO single crystal embedded in a dielectric material as shown schematically in Figure 7.1. In this way, on one hand one can increase the radiation area, and on the other hand one can form a cavity. Then there is a question: what is the optimal dielectric material for active radiation?

By answering this question, the cavity modes and quality factor through are solved by Maxwell's equations and the phase dynamics in IJJs are analyzed according to the coupled sine-Gordon equations. We find that the radiation power has a maximum when the dielectric constant of wrapping material is adjusted. It is found that the maximum is realized when the radiation power equals the dissipation of Josephson plasma. This gives us the optimal dielectric constant of surrounding material in terms of the property of the superconductive single crystal. The maximal radiation power is proportional to the typical superconducting current squared and the typical normal resistance, or the gap energy squared divided by the typical normal resistance.

7.2 Cavity mode

The cavity modes and quality factor are solved through Maxwells equations to find the optimal dielectric constant of wrapping material. A long BSCCO cylinder wrapped by a dielectric material is considered. One can take the system as infinite in the c direction as a reasonable approximation when the thickness of the BSCCO cylinder is several wavelengths, i.e. several millimeters. The dielectric constant of wrapping material should be larger than that of BSCCO sample to ensure the existence of radiating modes. We consider the EM fields is uniform along the c direction as we are interested in coherent radiations.

For a radiating (or an open) system, the EM waves should be described by complex electromagnetic waves. By considering the Helmholtz wave equation and the continuity conditions of EM wave at the interface between BSCCO single crystal and surrounding material, the complex eigen wave number k_{mn} can be given by [88]

$$(J_m' H_m)^2 + \varepsilon_r \left(J_m H_m'\right)^2 + (1+\varepsilon_r) J_m' J_m H_m H_m' = 0, \tag{7.1}$$

where $J_m(\sqrt{\varepsilon_c} k_{mn} R)$ and $H_m(\sqrt{\varepsilon} k_{mn} R)$ are the first kind of Bessel and Hankel functions with R the radius of BSCCO cylinder, $\varepsilon_r = \varepsilon/\varepsilon_c$ (for BSCCO we take $\varepsilon_c = 16$) is the ratio between dielectric constants of wrapping material and BSCCO single crystal; “prime”s denote the derivatives with respect to R.

The derivation of eigen equation can be obtained by considering the continuities of electromagnetic fields at the boundary of BSCCO cylinder, which is given as follows. The electric field and magnetic field in the z direction of the system can be written as

$$E_z = \begin{cases} A_e\, J_m\left(\sqrt{\varepsilon_c} k_{mn} \rho\right) \cos(m\phi) & \rho \le R \\ C_e\, H_m\left(\sqrt{\varepsilon_d} k_{mn} \rho\right) \cos(m\phi) & \rho > R \end{cases}, H_z = \begin{cases} A_h\, J_m\left(\sqrt{\varepsilon_c} k_{mn} \rho\right) \cos(m\phi) & \rho \le R \\ C_h\, H_m\left(\sqrt{\varepsilon_d} k_{mn} \rho\right) \cos(m\phi) & \rho > R \end{cases} \tag{7.2}$$

With A_e (A_h) and C_e (C_h) the amplitude of electric (magnetic) field inside and outside the BSCCO cylinder to be determined. From the Maxwell equations we have relation between the electromagnetic fields in z direction and the electromagnetic fields in later direction as

$$\mathbf{H}_t = \frac{ik_z}{\varepsilon_c \omega^2} \nabla_t H_z + \frac{i\varepsilon_0}{\omega} \hat{\mathbf{z}} \times \nabla_t E_z \tag{7.3}$$

$$\mathbf{E}_t = \frac{ik_z}{\varepsilon_c \omega^2} \nabla_t E_z - \frac{i\mu_0}{\omega \varepsilon_p} \hat{\mathbf{z}} \times \nabla_t H_z, \tag{7.4}$$

where ∇_t refers to take derivatives in lateral directions. Considering the continuity of electric field at the edge of BSCCO cylinder, one has the following boundary condition

$$\begin{gathered} E_\phi(R^+) = E_\phi(R^-), E_z(a^+) = E_z(R^-), \\ H_\phi(R^+) = H_\phi(R^-), H_z(a^+) = H_z(R^-). \end{gathered} \tag{7.5}$$

Substitute Eqs. (7.2) to (7.4) into the above boundary condition, one obtains the following relation

$$\begin{bmatrix} \left(\frac{1}{\varepsilon_c} + \frac{1}{\varepsilon}\right) \frac{mk_z}{\omega^2 a} & -\left(\frac{mu_0}{\sqrt{\varepsilon_c}} \frac{J_m'}{J_m} + \frac{\mu_0}{\sqrt{\varepsilon}} \frac{H_m'}{H_m}\right) \\ \sqrt{\varepsilon_c} \frac{J_m'}{J_m} + \sqrt{\varepsilon} \frac{H_m'}{H_m} & -\left(\frac{1}{\varepsilon_c} + \frac{1}{\varepsilon}\right) \frac{mk_z}{\omega^2 a} \end{bmatrix} \begin{bmatrix} A_e \\ \\ A_h \end{bmatrix} = 0. \tag{7.6}$$

Then in order to get non-trivial solution of A_e and A_h, the determinant of Eq. (7.6) should be zero and considering that we are focusing on uniform modes with $k_z \equiv 0$, one obtains the eigen equation given by Eq. (7.1).

Solving Eq. (7.1) one obtains two kinds of cavity modes, namely perfect magnetic conductor (PMC) like one, and perfect electric conductor (PEC) like one [88]. Here we take the PMC-like (1,1) mode as an example, and the extension for other modes is straightforward. The spatial part of the electric field in the z (or c) direction for PMC-like (1,1) mode inside the BSCCO cylinder is given by [41]

$$g_{11}(\mathbf{r}) = J_1(\sqrt{\varepsilon_c} k_{11}\rho)\cos\phi \tag{7.7}$$

with the cylindrical coordinate $\mathbf{r} = (\rho, \phi)$, k_{11} the eigen wave number of PMC-like (1,1) mode, as shown in Figure 7.2.

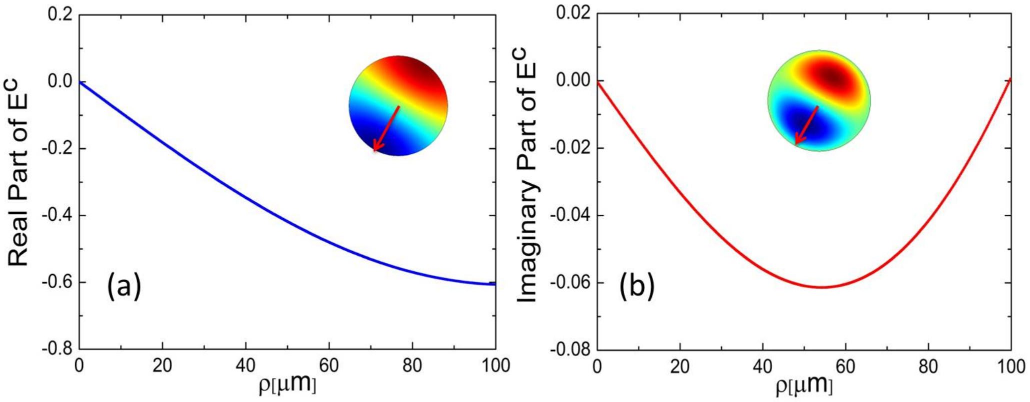

Figure 7.2: Distribution of (a) the real part and (b) the imaginary part of electric field in the c direction for PMC-like (1,1) mode.

The angular eigen frequency, or equivalently the real part of eigen wave number k_{11} in a dimensionless form, is given by

$$\omega_0 = \frac{\chi_{11} c}{R\sqrt{\varepsilon_c}} \tag{7.8}$$

with $\chi_{11} \approx 1.84$ standing for the first node of J_1'. For $R = 100\mu m$ and $\varepsilon_c = 16$, $f_0 = \omega_0/2\pi = 0.22$THz. The eigen frequency will not change with the dielectric constant of wrapping material as far as it is larger than the one of BSCCO sample.

7.3 Quality factor

The quality factor is given by the ratio between the stored energy and the power loss multiplying an applied frequency. There are two sources of power loss in the system: one comes from the radiation, and the other is the dissipation due to ohmic heating. In order to characterize the radiation energy from the open system, only the radiation power is considered in the quality factor and the ohmic dissipations are taken into account in the phase dynamic part as discussed later. In this way, the quality factor accounting for radiation is given by

$$Q \equiv \omega_0 \frac{\text{Energy} \quad \text{Stored}}{\text{Radiation} \quad \text{Power}}. \tag{7.9}$$

Considering that a cavity mode oscillates harmonically with time, the radiation part of quality factor can be rewritten as

$$Q = \frac{k_\mathrm{r}}{2k_\mathrm{i}}, \tag{7.10}$$

where k_r and k_i are the real and imaginary parts of wave number respectively. The ε_r dependence of Q can be evaluated by Eqs. (4) and (7). As displayed by figure 5, the Q increases with ε_r approximately in the form:

$$Q \approx 0.66\sqrt{\varepsilon_r} - 0.13. \tag{7.11}$$

$$Q \approx 0.66\sqrt{\varepsilon_r} - 0.13. \tag{7.12}$$

As seen in Eq. (9), Q diverges at infinite ε_r because only the radiation part of quality factor is considered here.

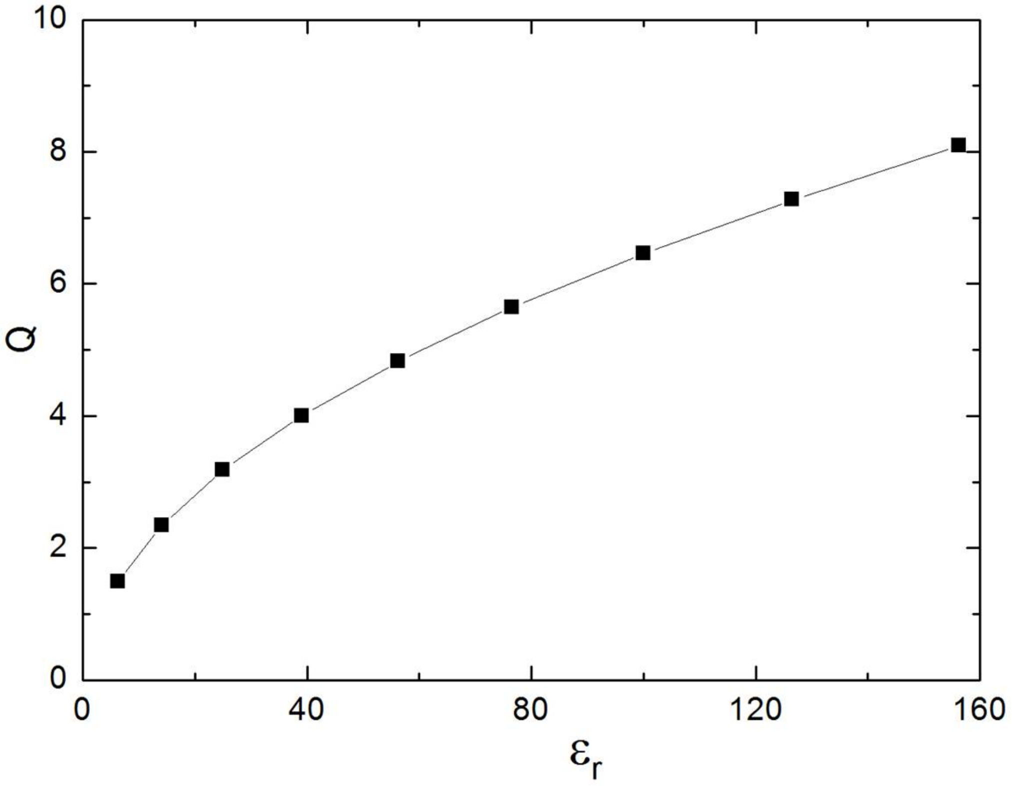

Figure 7.3: Dependence of the quality factor on the ratio of dielectric constants between wrapping material and BSCCO single crystal for PMC-like (1,1) mode.

Q increases as the dielectric constant of wrapping material increases, and finally a perfect cavity is formed where emission is reduced to vanishingly small.

7.3.1 Quality factor for rectangular geometry

By solving the eigen value equations for plane wave, we can obtain the expression of quality factor for rectangular BSCCO single crystal wrapped by a dielectric material explicitly.

The electric field in c direction in the BSCCO and dielectric material can be given respectively by

$$E_c = \frac{A_1}{\sqrt{\varepsilon_c}} exp[i(\sqrt{\varepsilon_c}ky + \omega t)] - \frac{A_2}{\sqrt{\varepsilon_c}} exp[i(-\sqrt{\varepsilon_c}ky + \omega t)], \tag{7.13}$$

$$E_c = \frac{C_1}{\sqrt{\varepsilon_d}} exp[i(\sqrt{\varepsilon_c}ky + \omega t)] - \frac{A_2}{\sqrt{\varepsilon_d}} exp[i(-\sqrt{\varepsilon_c}ky + \omega t)], \tag{7.14}$$

where ε_c and ε_d are the dielectric constants in the BSCCO and the dielectric material. Then from the Maxwell's equations, the magnetic fields in the BSCCO and the dielectric material can be given by

$$B_x = A_1 exp[i(\sqrt{\varepsilon_c ky + \omega t})] + A_2 exp[i(-\sqrt{\varepsilon_c}ky + \omega t)], \tag{7.15}$$

$$B_x = C_1 exp[i(\sqrt{\varepsilon_d ky + \omega t})] + C_2 exp[i(-\sqrt{\varepsilon_d}ky + \omega t)]. \tag{7.16}$$

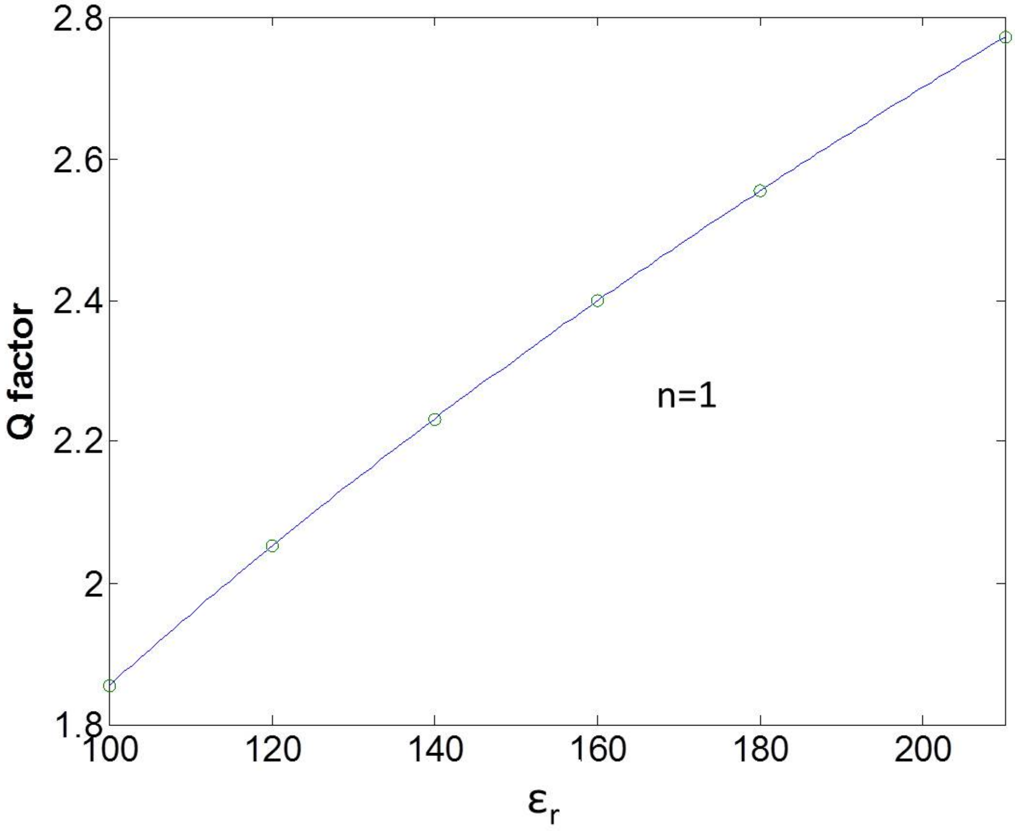

Figure 7.4: Dependence of the quality factor on the ratio of dielectric constants between wrapping material and BSCCO single crystal for rectangular BSCCO single crystal surrounded by a dielectric material. The line and dot denote the analytical result of Eq. (7.18) and the numerical result obtained by finite element method package COMSOL.

On the the left boundary where $y = 0$ we have

$$B_x(0^+) = B_x(0^-) \tag{7.17}$$

$$E_z(0^+) = E_z(0^-) \tag{7.18}$$

with $C_1 = 0$, and on right boundary where $y = L$ we have

$$B_x(L^+) = B_x(L^-) \tag{7.19}$$

$$E_z(L^+) = E_z(L^-) \tag{7.20}$$

with $C_2 = 0$. After a straight calculation and eliminating C_1 and C_2 we obtain the equations for A_1 and A_2

$$\begin{pmatrix} 1+\sqrt{\varepsilon_r} & 1-\sqrt{\varepsilon_r} \\ \left(1-\sqrt{\varepsilon_r}\right) exp\left(i\sqrt{\varepsilon_c}kL\right) & \left(1+\sqrt{\varepsilon_r}\right) exp\left(-i\sqrt{\varepsilon_c}kL\right) \end{pmatrix} \begin{pmatrix} A_1 \\ A_2 \end{pmatrix} = 0. \tag{7.21}$$

In order to obtain non-trivial solutions, the determinant should be zero, the we obtain

$$exp\left(2\sqrt{\varepsilon_c}i(k_r+ik_i)L\right) = \left(\frac{1+\sqrt{\varepsilon_r}}{1-\sqrt{\varepsilon_r}}\right)^2, \tag{7.22}$$

where k_r and k_i are the real and imaginary parts of wave number. Solving this complex equation we have

$$k_r = \frac{n\pi}{\sqrt{\varepsilon_c}L} \quad , \quad k_i = \frac{1}{\sqrt{\varepsilon_c}L} \ln \frac{\sqrt{\varepsilon_r} - 1}{\sqrt{\varepsilon_r} + 1}. \tag{7.23}$$

Then we can calculate the quality factor straightforwardly from Eq. (7.5)

$$Q = \frac{k_r}{2k_i} = \frac{n\pi}{2 \ln \frac{\sqrt{\varepsilon_r}+1}{\sqrt{\varepsilon_r}-1}}. \tag{7.24}$$

For the fundamental cavity mode $n = 1$ the ε_r dependence of Q is shown in Figure 7.4.

7.4 Phase dynamics in the proposed device

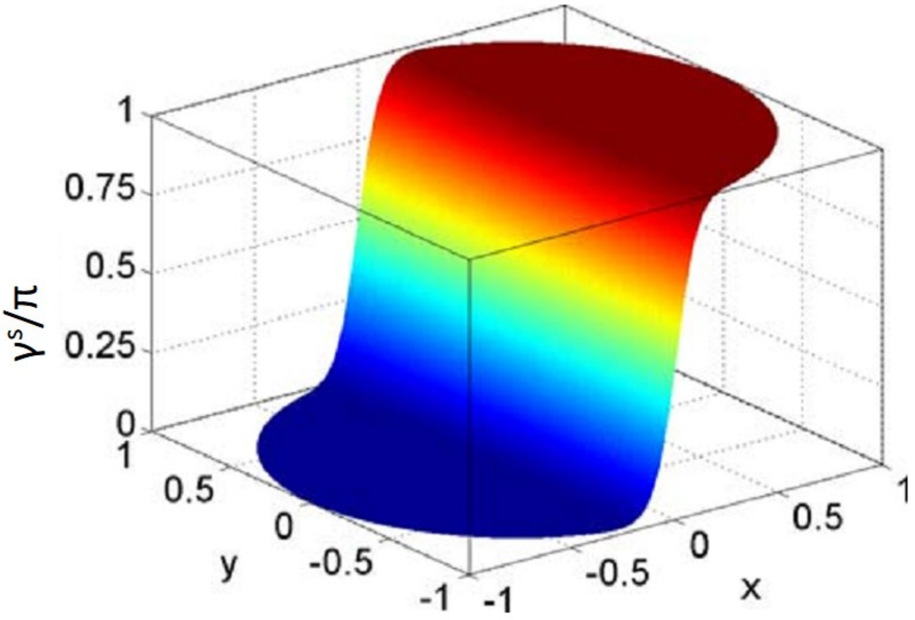

Figure 7.5: Corresponded π phase kink for the PMC-like (1,1) of BSCCO cylinder wrapped by a dielectric material.

The π kink solution can also be applied to the cylindrical geometry. The solution of kink state can be constructed as follows. First one finds the cavity mode by solving the Maxwell equations for the BSCCO cylinder embedded in a dielectric material as we have already done in the previous section. One then substitutes the resulting cavity mode in the coupled sine-Gordon equation to find the solution for phase kinks and amplitude of the plasma oscillations. The corresponded π phase kink state for cylindrical (1,1) mode is displayed in Figure 7.5.

The radiation power and plasma dissipation per unit length in the c direction can be given respectively by

$$P_{\mathrm{r}} = \frac{\omega}{2Q} \int |E|^2 d\Omega, \quad P_{\mathrm{dp}} = \frac{\beta}{2} \int |E|^2 d\Omega, \tag{7.25}$$

where $E = i\omega A g$ is the spatial part of electric field in the c direction.

For a given Q factor, or equivalently a given dielectric constant (see Eq. (7.12)), the voltage dependence of current injection and radiation power can be evaluated by solving Eqs.(4.23) to (4.25). The result for $Q = 73.73$ (or $\varepsilon = 2.01 \times 10^5$) is displayed in Figure 7.4.

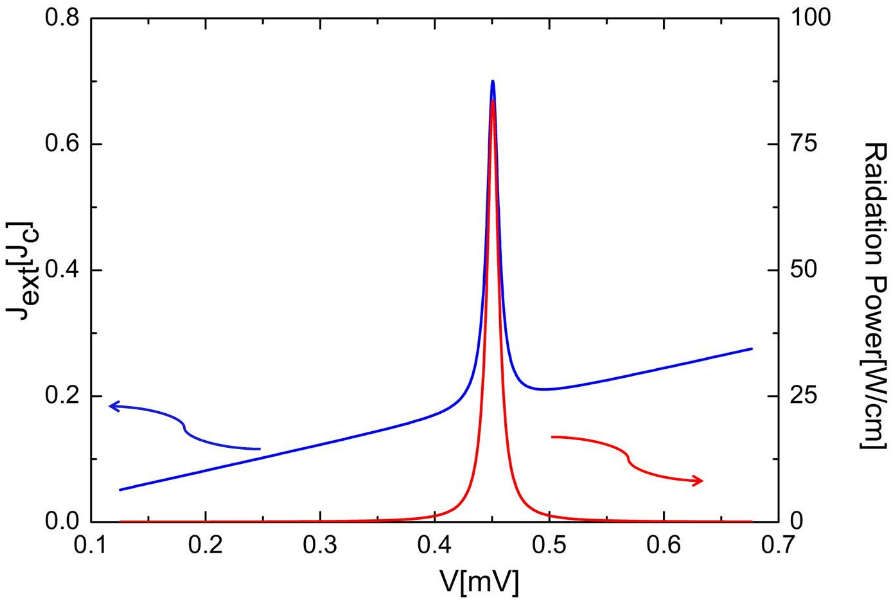

Figure 7.6: Dependence of current injection and radiation power on the bias voltage for Q=73.72 and β =0.05. The resonance takes place at V=0.45mV, which corresponds to the eigen frequency 0.22 THz of the PMC-like (1,1) mode for R=100μm.

7.5 Optimal radiation power

Now we investigate the Q-dependence of the radiation power and the dissipation caused by plasma oscillation. As shown in Figure 7.7, the radiation power reaches its maximum when it equals the plasma dissipation. The reason for the existence of a maximal radiation power is that there exist two competing factors in the system: a good cavity associated with large Q makes a strong resonance on one hand, but it suppresses energy leak on the other hand.

In order to understand the optimal condition for radiation power, we check the relations between radiation power and plasma dissipation. The ratio between them is given by

$$\frac{P_{\mathrm{r}}}{P_{\mathrm{dp}}} = \frac{\omega}{Q\beta}. \tag{7.26}$$

From the energy conservation we have

$$P_{\mathrm{r}} + P_{\mathrm{dp}} = \frac{S}{2}\omega(J_{\mathrm{ext}} - \omega\beta), \tag{7.27}$$

where S is the lateral area of BSCCO cylinder and $\omega\beta$ is the normal ohmic current.

From Eqs.(4.23) and (4.24) the supercurrent density is given by

$$J_{\mathrm{ext}} - \beta\omega = \frac{\nu}{S}\mathrm{Re}\left[\frac{1}{\mathrm{i}(\omega^2 - \mathrm{k}^2 - \mathrm{i}\omega\beta)}\right], \tag{7.28}$$

with

$$\nu = \frac{\left(\int g_{\mathrm{r}} \cos\gamma^s d\Omega\right)^2 + \left(\int g_{\mathrm{i}} \cos\gamma^s d\Omega\right)^2}{4\int |g|^2 d\Omega}, \tag{7.29}$$

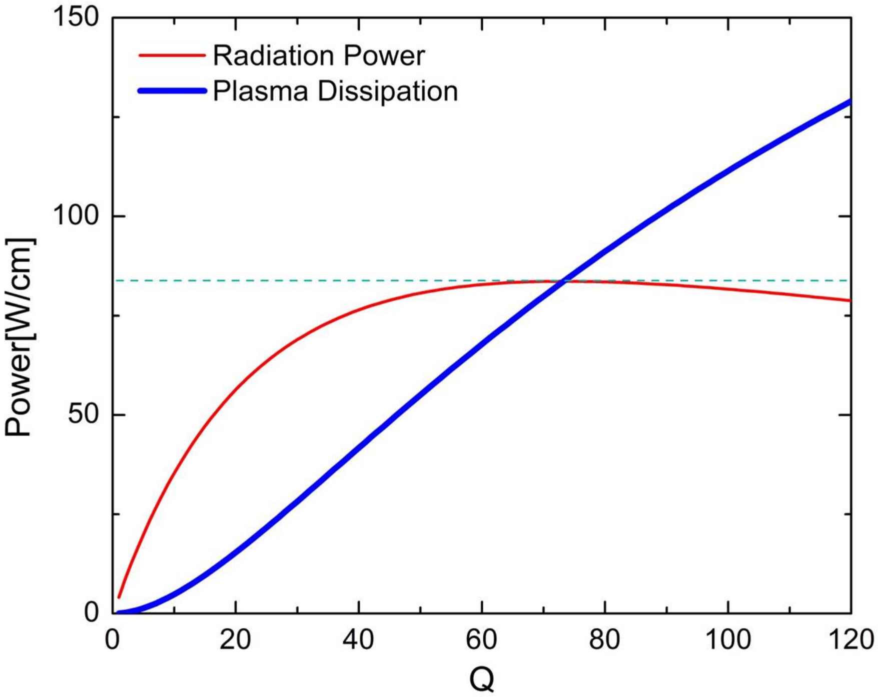

Figure 7.7: Q-factor dependence of radiation power and plasma dissipation at resonance for the PMC-like (1,1) mode with $\beta = 0.05$ and $R = 100\mu m$. The radiation power reaches its maximum when it equals plasma dissipation.

where g_r and g_i are the real and imaginary parts of cavity mode. From Eqs.(7.26) to (7.28), the radiation power at resonance where $\omega = k_\mathrm{r} = \omega_0$ can be given by

$$P_\mathrm{r} = \frac{\nu\omega_0/Q}{2(\omega_0/Q + \beta)^2}. \tag{7.30}$$

It is then clear that P_r reaches the maximal value at

$$Q = \frac{\omega_0}{\beta}, \tag{7.31}$$

where $P_\mathrm{r} = P_\mathrm{dp}$ from Eq. (7.26).

By substituting Eq. (7.12) into Eq. (7.31), the optimal dielectric constant of wrapping material for strong radiation can be obtained

$$\frac{\varepsilon}{\varepsilon_c} \approx \left(\frac{\chi_{11} c\sqrt{\varepsilon_c}}{2.64\pi R\sigma_c} + 0.20\right)^2. \tag{7.32}$$

In Gaussian units, Eqs.(7.30) and (7.31) give

$$P_\mathrm{r} = \frac{\nu}{8} I_\mathrm{c}^2 R_c, \tag{7.33}$$

where $I_\mathrm{c} \equiv J_\mathrm{c}\lambda_c^2 = c\phi_0/8\pi^2 s$ is the typical superconducting current with ϕ_0 the magnetic flux quantum, $R_c \equiv 1/\sigma_c\lambda_c^2$ is the typical c-axis resistance per unit length of BSCCO sample. This expression looks like the Ohm's law but we should notice that I_c is the typical superconducting current.

The Eq. (7.33) can also be written as:

$$P_\mathrm{r} = \frac{\nu\pi^2\Delta^2}{32 R_\mathrm{c} s^2 e^2}, \tag{7.34}$$

where $\Delta = ec\phi_0/4\pi^3\lambda_c^2\sigma_c$ is the superconducting gap energy.

For the PMC-like (1,1) mode $\nu \approx 0.15$. Taking $I_c = 0.22$A, $R_c = 0.95 \times 10^5\Omega$/cm, typical values for BSCCO, [26] the maximal radiation power is evaluated as 85W/cm.

7.5.1 Other cavity modes

In above discussion we take PMC-like (1,1) mode as an example. From Eq. (7.20) one sees that the optimal condition dose not depend on the specific cavity modes or geometries, all the couplings between the cavity mode and the phase kink manifests itself through the geometric factor *nu*. Here we show the case for PMC-like (2,1) mode, which is displayed in Figure 7.8. As shown in Figure 7.8, the radiation power reaches its maximum when it equations the dissipation caused by Josephson plasma, which is the same as the PMC-like (1,1) mode.

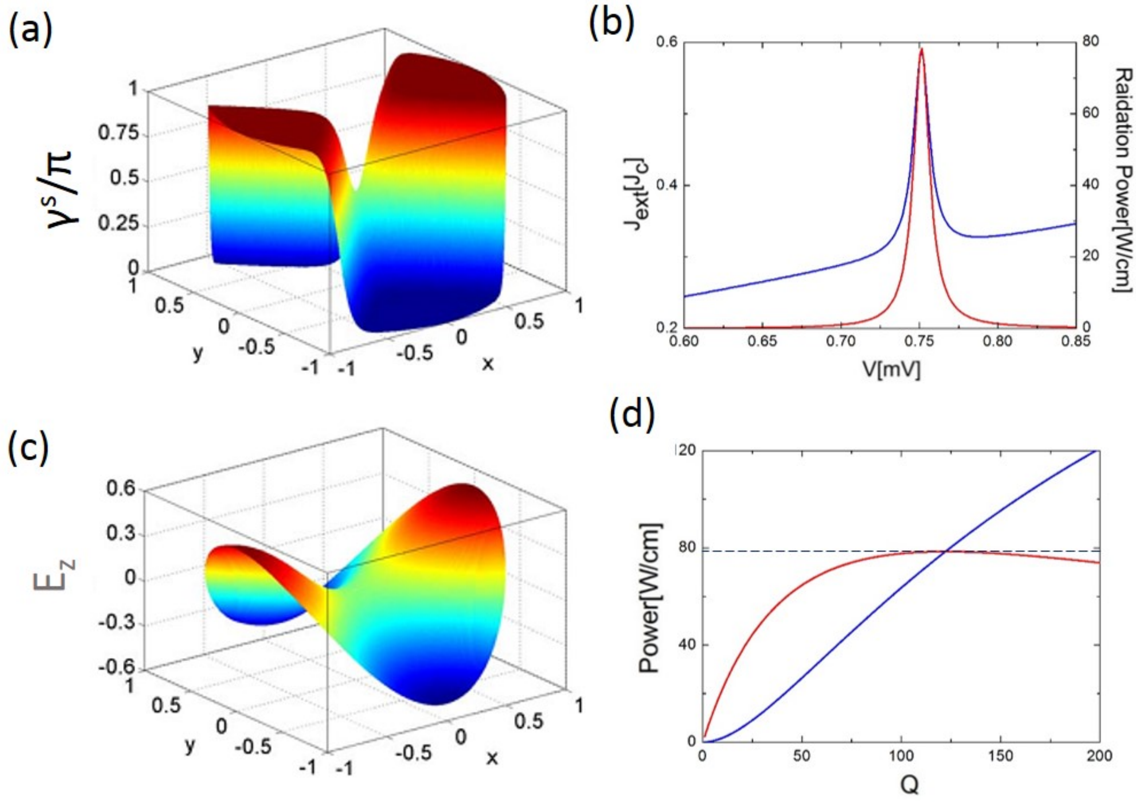

Figure 7.8: (a) spatial distribution of phase difference, (b) I-V characteristic, (c) standing electric field, (d) Q dependences of radiation power and plasma dissipation for PMC-like (2,1) cavity mode of BSCCO cylinder surrounded by a dielectric material with $R_0 = 100\mu m$.

7.6 Verification of energy conservation

During the derivation of the optimal condition for radiation power we apply the energy conservation law and we treat the radiation part as a perturbation in the coupled sine-Gordon equations. Here we verify the energy conservation law at the resonance to justify the approximation used above. The radiation power per unit length can be written as the integration of Poynting vector over the edge of BSCCO cylinder

$$\begin{aligned} P_r &= \mathrm{Re}\left[-\frac{1}{2}\int_0^{2\pi} E_z^* B_\phi R_0 d\phi\right] = \int_0^{2\pi} \mathrm{Re}\left[i\omega k R_0 |A|^2 J_n^*(kR_0) J_n'(kR_0)\cos^2(m\phi)\right] d\phi \\ &= \mathrm{Re}\left[i\pi |A|^2 \omega k R_0 J_n^*(k_{mn}R_0) J_n'(k_{mn}R_0)/2\right]. \end{aligned} \tag{7.35}$$

Here we take PEC-like (1,1) mode as an example and use the relation $Q = k_r/2k_i$, the radiation power at resonance place can cast into

$$P_r = \frac{\pi |A|^2 \omega_0^3 r_0^2}{4Q} |J_1'(\chi_{11})|^2, \tag{7.36}$$

where the approximation $J_1^*(k_r(1 + i/2Q)r_0) = J_1^*(\chi_{11}) - J_1'^*(\chi_{11}) i k_r r_0/2Q$ is applied for $Q \gg 1$. The Joule heating can be given as

$$\begin{aligned} P_{\mathrm{dis}} &= \frac{\beta}{2}\int_S |E_z|^2 d\Omega = \beta \int_0^{2\pi} \cos^2\phi d\theta \int_0^{R_0} \rho d\rho (\omega_0^2 + \omega_0^2 |A|^2 |J_1(k_{11}\rho)|^2) \\ &= \frac{S}{2}\beta\omega_0^2 + \frac{\pi}{2}\beta\omega_0^2 |A|^2 \int_0^{R_0} |J_1(k_{11}\rho)|^2 \rho d\rho = \frac{S}{2}\beta\omega_0^2 + \frac{\pi\beta\omega_0^2 |A|^2 R_0^2}{4} |J_1'(\chi_{11})|^2, \end{aligned} \tag{7.37}$$

where the relation $\int_0^1 x J_1(x\chi_{11}) J_1(x\chi_{11}) = [J_1'(\chi_{11})]^2/2$ is used. Then we take the Eq. (4.24) into Eq. (7.36) and obtain

$$P_r = \frac{\pi\omega_0^3 r_0^2}{4Q} |J'(\chi_{11})|^2 \frac{|\int g^* \cos\gamma^s d\Omega|^2}{4(\omega_0^2/Q + \omega_0\beta)^2 (\int |g|^2 d\Omega)^2} = \frac{\nu\omega_0/Q}{2(\omega_0/Q + \beta)} \tag{7.38}$$

with ν the geometric factor defined in Equation (7.29). Similarly we have the expression for the Joule heating

$$P_{\mathrm{dis}} = \frac{S}{2}\beta\omega_0^2 + \frac{\nu\beta}{2(\omega_0/Q + \beta)^2}. \tag{7.39}$$

The total energy is given then

$$P_{\mathrm{total}} = P_r + P_{\mathrm{dis}} = \frac{S}{2}\beta\omega_0^2 + \frac{\nu}{2(\omega_0/Q + \beta)}, \tag{7.40}$$

which is just the $S J_{\mathrm{ext}}\omega$ followed Equation. (7.28).

7.7 Setup with anti-reflection coating

In the above discussion we focus on the simple case in which the thickness of wrapping material is infinite, where the only one reflection of EM wave at the interface between BSCCO and the dielectric material determines the cavity frequency. In what following, we show that two wrapping layers with finite thicknesses can work in the same way (Figure 7.9), when the dielectric constant and thickness of the outside layer are tuned appropriately such that the two reflections at the interfaces between the two wrapping layers and between the outer layer and vacuum cancel each other totally.

The ratio between ingoing and outgoing of electric fields at the interface between two dielectric layers is given by

$$r = \frac{M_{11} H_m^{(1)}(k_{\mathrm{L}}a_1) H_m^{(1)\prime}(k_{\mathrm{R}}a_2) + M_{12} H_m^{(1)\prime}(k_{\mathrm{L}}a_1) H^{(1)\prime}(k_{\mathrm{R}}a_2) - M_{21} H_m^{(1)}(k_{\mathrm{L}}a_1) H_m^{(1)}(k_{\mathrm{R}}a_2) - M_{22} H_m^{(1)\prime}(k_{\mathrm{L}}a_1) H_m^{(1)}(k_{\mathrm{R}}a_2)}{M_{21} H_m^{(2)}(k_{\mathrm{L}}a_1) H_m^{(1)}(k_{\mathrm{R}}a_2) + M_{22} H_m^{(2)\prime}(k_{\mathrm{L}}a_1) H_m^{(1)}(k_{\mathrm{R}}a_2) - M_{11} H_m^{(2)}(k_{\mathrm{L}}a_1) H_m^{(1)\prime}(k_{\mathrm{R}}a_2) - M_{12} H_m^{(2)\prime}(k_{\mathrm{L}}a_1) H_m^{(1)\prime}(k_{\mathrm{R}}a_2)}, \tag{7.41}$$

with the transfer matrix

$$\mathbf{M} = \begin{pmatrix} H_m^{(1)}(k_M a_2) & -H_m^{(2)}(k_M a_2) \\ H_m^{(1)\prime}(k_M a_2) & -H_m^{(2)\prime}(k_M a_2) \end{pmatrix} \begin{pmatrix} H_m^{(1)}(k_M a_1) & -H_m^{(2)}(k_M a_1) \\ H_m^{(1)\prime}(k_M a_1) & -H_m^{(2)\prime}(k_M a_1) \end{pmatrix}^{-1}, \tag{7.42}$$

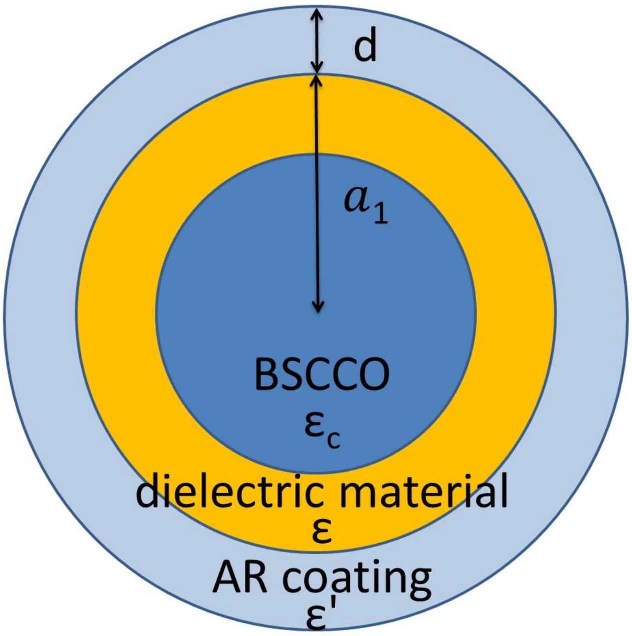

Figure 7.9: Schematic view of the proposed device with anti-reflection coating.

where k_L, k_M and k_R are the wave numbers in the inner wrapping layer, the AR coating and vacuum respectively, and $a_2 = a_1 + d$ (for definition see Figure 7.9); "prime"s denote the derivatives with respect to a_1 or a_2. Solving the equation $r = 0$ the dielectric constant and thickness of AR coating can be determined as functions of ε and a_1. Numerical results for typical parameters are displayed in Figure 7.10.

7.7.1 AR coating for cylindrical wave

For cylindrical propagation wave the electric field in the c direction can be written by

$$E_c(k,\rho) = A_1 H_m^{(1)}(k\rho) - A_2 H_m^{(2)}(k\rho), \tag{7.43}$$

where $H_m^{(1)}$ and $H_m^{(2)}$ are the first and the second kind of Hankel function, presenting the outgoing and ingoing cylindrical waves. From Maxwell's equations, the magnetic field in the angular direction is given by

$$B_\theta(k,\rho) = \frac{1}{i\omega}\left[A_1 H_m^{(1)\prime}(k\rho) - A_2 H_m^{(2)\prime}(k\rho)\right] \tag{7.44}$$

with "prime" denoting the derivative with respect to ρ.

Considering the continuity of E_c and B_θ at the interfaces between the inner wrapping layer and the AR coating and between the AR coating and vacuum (Figure. 7.9), we obtain

$$\begin{pmatrix} H_m^{(1)}(k_L a_1) & -H_m^{(2)}(k_L a_1) \\ H_m^{(1)\prime}(k_L a_1) & -H_m^{(2)\prime}(k_L a_1) \end{pmatrix}\begin{pmatrix} A_{L1} \\ A_{L2} \end{pmatrix} = \begin{pmatrix} H_m^{(1)}(k_M a_1) & -H_m^{(2)}(k_M a_1) \\ H_m^{(1)\prime}(k_M a_1) & -H_m^{(2)\prime}(k_M a_1) \end{pmatrix}\begin{pmatrix} A_{M1} \\ A_{M2} \end{pmatrix}, \tag{7.45}$$

$$\begin{pmatrix} H_m^{(1)}(k_M a_2) & -H_m^{(2)}(k_M a_2) \\ H_m^{(1)\prime}(k_M a_2) & -H_m^{(2)\prime}(k_M a_2) \end{pmatrix}\begin{pmatrix} A_{M1} \\ A_{M2} \end{pmatrix} = \begin{pmatrix} H_m^{(1)}(k_R a_2) \\ H_m^{(1)\prime}(k_R a_2) \end{pmatrix} A_{R1}, \tag{7.46}$$

where k_L, k_M, and k_R are the wave vectors, A_{L1}, A_{L2}, and A_{M1}, A_{M2}, and A_{R1} are the amplitudes of electric field in the inner wrapping layer, the AR coating and the vacuum respectively. Eliminating A_{M1} and A_{M2} in

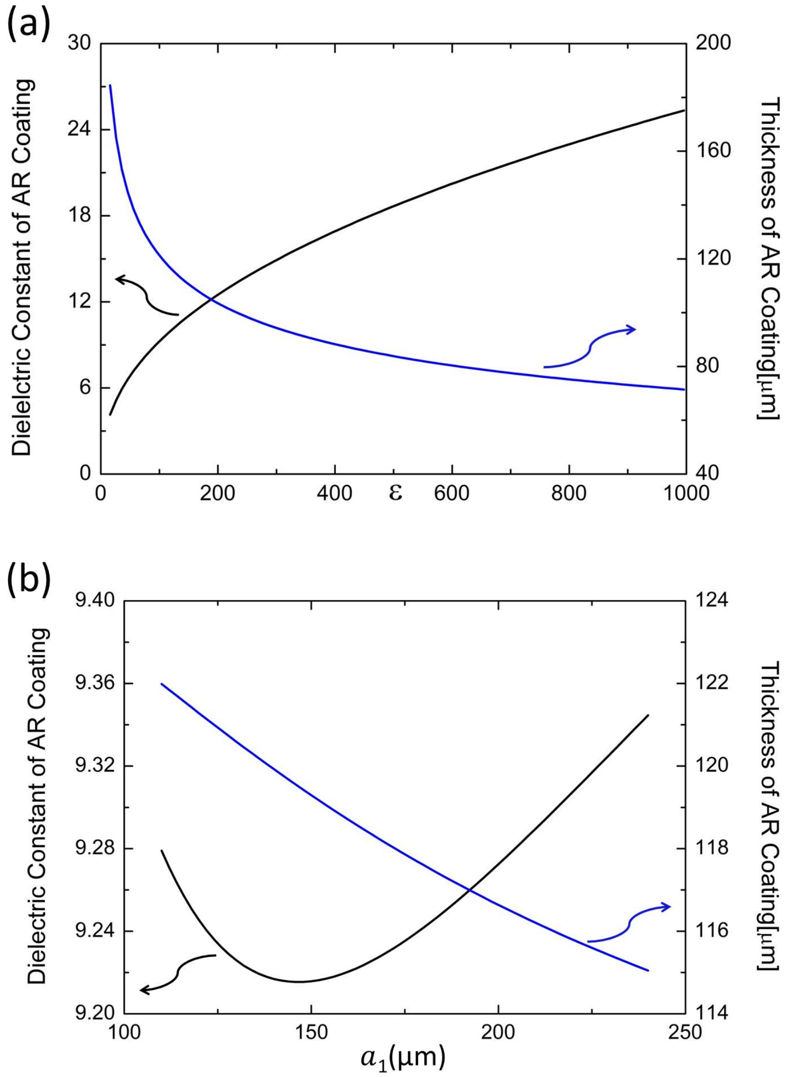

Figure 7.10: Dependence of dielectric constant and thickness of anti-reflection coating on (a) the dielectric constant of the inner wrapping layer with $a_1 = 120\mu$m, (b) the thickness of the inner wrapping layer with $\varepsilon = 100$ of PMC-like (1,1) mode with eigen frequency 0.22THz.

Eqs. (7.45) and (7.46) we have

$$\mathbf{M}\begin{pmatrix} H_m^{(1)}(k_\mathrm{L}a_1) & -H_m^{(2)}(k_\mathrm{L}a_1) \\ H_m^{(1)\prime}(k_\mathrm{L}a_1) & -H_m^{(2)\prime}(k_\mathrm{L}a_1) \end{pmatrix}\begin{pmatrix} A_\mathrm{L1} \\ A_\mathrm{L2} \end{pmatrix} = \begin{pmatrix} H_m^{(1)}(k_\mathrm{R}a_2) \\ H_m^{(1)\prime}(k_\mathrm{R}a_2) \end{pmatrix} A_\mathrm{R1}. \tag{7.47}$$

Then we obtain the reflectance $r \equiv A_\mathrm{L2}/A_\mathrm{L1}$ as given in Eq. (7.41) and the transmittance $t \equiv A_\mathrm{R1}/A_\mathrm{L1}$ as

$$t = \frac{4i/\pi a_2}{M_{21}H_m^{(2)}(k_\mathrm{L}a_1)H_m^{(1)}(k_\mathrm{R}a_2) + M_{22}H_m^{(2)\prime}(k_\mathrm{L}a_1)H_m^{(1)}(k_\mathrm{R}a_2) - M_{11}H_m^{(2)}(k_\mathrm{L}a_1)H_m^{(1)\prime}(k_\mathrm{R}a_2) - M_{12}H_m^{(2)\prime}(k_\mathrm{L}a_1)H_m^{(1)\prime}(k_\mathrm{R}a_2)}, \tag{7.48}$$

where the Wronskian formula

$$H_m^{(1)}(x)H_m^{(2)\prime}(x) - H_m^{(1)\prime}(x)H_m^{(2)}(x) = \frac{-4i}{\pi x}, \tag{7.49}$$

has been used in order to obtain Equation (7.48).

7.8 Discussions

The maximal radiation power is not affected by the radius of the BSCCO cylinder. The reason for this is that when the radius of the BSCCO cylinder increases, more current can be injected in, but the eigen frequency will decrease (proportional to the inverse of radius), with these two factors canceling each other. The optimal radiation power Eq. (7.33) is apparently similar to the result in Ref. [13], but there the discussion was limited to nonresonant junctions.

The result that the radiation power is maximal when it equals the dissipation can be considered as a case of Jacobi's law. Krasnov reached numerically at a similar result for radiation in finite magnetic fields [87]. This result does not depend on the geometry of BSCCO single crystal which can be seen from Eq. (7.3).

In the present work, we focus on the case that the Josephson plasma is uniform along a long crystal as established by the cavity formed by the dielectric material. The maximal radiation power is therefore given by power per unit length. Bulaevskii and Koshelev discussed the case that synchronization is achieved by the coupling between Josephson plasma and EM wave [25]. Therefore, their maximal radiation power is achieved when the length of BSCCO single crystal at *c*-axis equals the EM wave length.

8 Summary

In this thesis, the dynamics of the gauge invariant phase difference in a stack of coupled IJJs are investigated by the inductively coupled sine-Gordon equations, which is useful for the development of an efficient and compact device for electromagnetic wave radiation in terahertz band. Three aspects of phase dynamics of IJJs toward terahertz radiations are discussed including an efficient way to synchronize the system to the π phase kink state, a general solution at small and medium inductive coupling and an optimal condition for radiation power in a long stack of IJJs in a cylindrical geometry.

In order to reveal the way to synchronize efficiently the IJJs to the π phase states, we have studied phase dynamics starting from random and several typical ordered initial phase configurations by numerical simulations. It is found that for random initial phase configurations the system can be driven into the phase kink states. The average time spent before entering the π phase kink states is shorter when the standard deviation of random distribution is larger corresponding to higher temperature. The system can be driven into the π phase kink state staring from several typical initial phase configurations, which can be done by applying a non-uniform bias voltage.

By computer simulations, we solve coupled sine-Gordon equations with weak and moderate inductive couplings under current driving and dissipations for the phase dynamics of IJJs. We find a general solution characterized by a static term γ^s in gauge-invariant phase differences in IJJs, which is distributed around $\pm\pi/2$ in form of cavity mode in in-plane directions and arranged alternatingly along c direction. This solution is stable at small and moderate inductive couplings and high cavity modes, and evolves into the π phase kink state at large inductive coupling. Calculating the I-V characteristics of this solution, we show that large energy can be pumped into the cavity modes at the resonance voltages, which is useful for strong terahertz electromagnetic radiation. This state may hopefully trigger a search for source of strong terahertz electromagnetic wave in a broader class of superconducting materials.

In order to enhance the radiation power in the terahertz band we embed a long $Bi_2Sr_2CaCu_2O_{8+\delta}$ cylinder in a dielectric material to increase the radiation area and simultaneously form a cavity. We find that the radiation power has a maximum when the dielectric constant is tuned. The maximum is achieved when the radiation power equals the dissipation caused by the ac voltage associated with plasma oscillation, which yields the optimal dielectric constant of the wrapping material in terms of the properties of the superconducting single crystal. The maximal radiation is proportional to the critical superconducting current squared and the typical normal resistance, which offers a guideline for choosing superconductors as a source of strong radiation. Adding an anti-reflection coating, we can build a compact device with the $Bi_2Sr_2CaCu_2O_{8+\delta}$ cylinder and two wrapping dielectric layers with finite thicknesses.

9 Acknowledgements

First of all, I would like to thank my supervisor Prof. Xiao Hu sincerely for bringing me into such an interesting field, for his precious direction and strong support in my research activity at every moment.

I am also grateful to other members in the group, Dr. T. Kawakami, Dr. B. Xi, Dr. R. Yu. I benefited a lot from their weekly group seminar and the discussions with them. I am also grateful to the group sectaries Mrs. Akemi for their kind assistances.

At last I want to thank my family especially my wife Ms. F. Fang for her kind understanding and patience.

Bibliography

[1] B. Ferguson and X.-C. Zhang, "Material for terhertz science and technology," Nature Mater. **1**, 26 (2002).

[2] M. Tonouchi, "Cutting-edge terahertz technology," Nat. Photonics **1**, 97 (2007).

[3] B. D. Josephson, "Possible New Effects in Superconductive Tunnelling," Phys. Lett. **1**, 251 (1962).

[4] B. D. Josephson, "Coupled Superconcutors," Rev. Mod. Phys. **36**, 216 (1964).

[5] B. D. Josephson, "Supercurrents throuhg Barriers," Adv. Phys. **14**, 419 (1965).

[6] P. W. Anderson and J. M. Rowell, "Probable Observations of the Josephson Superconducting Tunneling Effect," Phys. Rev. Lett. **10**, 230 (1963).

[7] A. Barone and G. Paterno, *Physics and Applications of the Josephson Effect* (John Wiley&Sons, 1982)

[8] X. Hu and S.-Z. Lin, "Phase dynamics in a stack of inductively coupled intrinsic Josephson junctions and terahertz electromagnetic radiation," Supercond. Sci. Technol. **23**, 053001 (2010).

[9] U. Welp, K. Kadowaki and R. Kleiner, "Superconducting emitters of THz radiation," Nature Photon. **7**, 702 (2013).

[10] T. Finnegan and S. Wahlsten, "Observation of Coherent Microwave Radiation Emitted by Coupled Josephson Junctions," Appl. Phys. Lett. **21**, 541 (1972).

[11] N. F. Pedersen, O. H. Soerensen, J. Mygind, P. E. Lindelof, M. T. Levinsen, and T. D. Clark, "Experiments on Coupled Josephson Junctions," Appl. Phys. Lett. **28** 562 (1976).

[12] A.K. Jain, K.K. Likharev, J.E. Lukens and J.E. Sauvageau, "Mutual Phase-Locking in Josephson Junctions Arrays" Phys. Rep. **109**, 309 (1984).

[13] K. Wiesenfeld, S. P. Benz and P. A. A. Booi, "Phase-locked oscillator optimization for arrays of Josephson junctions," J. Appl. Phys. **76**, 3835 (1994).

[14] M. Darula, T. Doderer, and S. beuven, "Millimetre and sub0mm wavelength radiation sources based on discrete Josephson junctions arrays," Supercond. Sci. Technol. **12**, R1 (1999).

[15] P. Barbara, A. B. Cawthorne, S. V. Shitov, and C. J. Lobb, "Stimulated emission and amplification in Josephson junction arrays," Phys. Rev. Lett. **82**, 1963 (1999).

[16] A. V. Ustinov, H. Kohlstedt, M. Cirillo, N. F. Pedersen, G. Hallmanns, and C. Heiden, "Coupled Fluxon Modes in Stacked Nb/AlO$_x$/Nb Long Josephson Junctions," Phys. Rev. B **48**, 10614 (1993).

[17] R. Kleiner, F. Steinmeyer, G. Kunkel, and P. Müller, "Intrinsic Josephson Effects in $Bi_2Sr_2CaCu_2O_{8+\delta}$ Single-Crystal," Phys. Rev. Lett. **68**, 2394 (1992).

[18] E. Kume, I. Iguchi, and H. Takahashi, "On-chip spectroscopic detection of terahertz radiation emitted from a quasiparticle-injected nonequilibrium superconductor using a high-T$_c$ Josephson junction," Appl. Phys. Lett. **75**, 2809 (1999).

[19] K. Lee, W. Wang, I. Iguchi, M. Tachiki, K. Hirata, T. Mochiku, ”Josephson plasma emission from $Bi_2Sr_2CaCu_2O_y$ intrinsic junctions due to quasiparticle injection,” Phys. Rev. B **61**, 3616 (2000).

[20] I. E. Batov, X. Y. Jin, S. V. Shitov, Y. Koval, P. Müller, and A. V. Ustinov, ”Detection of 0.5 THz radiation from intrinsic $Bi_2Sr_2CaCu_2O_8$ Josephson junctions,” Appl. Phys. Lett. **88**, 262504 (2006).

[21] S. Sakai, P. Bodin and N. F. Pedersen, ”Fluxons in Thin-Film Superconductor-Insulator Superlattices,” J. Appl. Phys. **73**, 2411 (1993).

[22] M. Tachiki, T. Koyama, S. Takahashi, ”Electromagnetic phenomena related to a low-frequency plasma in cuprate superconductors,” Phys. Rev. B **50**, 7065 (1994).

[23] R. Kleiner, T. Gaber, G. Hechtfischer, ”Stacked long Josephson junctions in zero magnetic field: A numerical study of coupled one-dimensional sine-Gordon equations,” Phys. Rev. B **62**, 4086 (2000).

[24] S.-Z. Lin, X. Hu, and M. Tachiki, ”Computer simulation on terahertz emission from intrinsic Josephson junctions of high-T_c superconductors,” Phys. Rev. B **77**, 014507 (2008).

[25] L. N. Bulaevskii, and A. E. Koshelev, ”Radiation from a single Josephson junction into free space due to Josephson oscillations,” Phys. Rev. Lett. **99**, 057002 (2007).

[26] L. Ozyuzer, A. E. Koshelev, C. Kurter, N. Gopalsami, Q. Li, M. Tachiki, K. Kadowaki, T. Yamamoto, H. Minami, H. Yamaguchi, T. Tachiki, K. E. Gray, W.-K. Kwok, and U. Welp, ”Emission of Coherent THz Radiation from Superconductors, ”Science **318**, 1291 (2007).

[27] S.-Z. Lin and X. Hu, ”Possible dynamic states in inductively coupled intrinsic Josephson junctions of layered high-Tc superconductors,” Phys. Rev. Lett. **100**, 247006 (2008).

[28] A. E. Koshelev, ”Stability of dynamic coherent states in intrinsic Josephson-junction stacks near internal cavity resonance”, Phys. Rev. B **82**,174512 (2010).

[29] S.-Z. Lin and X. Hu, ”Stability of the kink state in a stack of intrinsic Josephson junctions”, Physica C **470**, S201 (2010).

[30] , T. Koyama, H. Matsumoto and M. Machida, ”Numerical simulation for THz wave emission from high-Tc intrinsic Josephson junctions”, Physica C **470**, S230 (2010).

[31] T. koyama, H. Matsumoto, Y. Ota and M. Machida, ”Numerical study for electromagnetic wave emission from intrinsic Josephson junction stacks with a dielectric cover”, Physica C **491**, 20 (2013).

[32] Y. Nonomura, ”Stationary phase-kink states and dynamical phase transitions controlled by surface impedance in terahertz wave emission from intrinsic Josephson junctions”, Phys. Rev. B 80, 140506(2009).

[33] A. E. Koshelev, and L. N. Bulaevskii, ”Resonant electromagnetic emission from intrinsic Josephson-junction stacks with laterally modulated Josephson critical current,” Phys. Rev. B **77**, 014530 (2008).

[34] J. Matisoo, ”Zero-Field Resonancesin Oxide Josephson JUnctions,” Physics Letters A **29**, 473(1969).

[35] M. Russo and R. Vaglio, ”Self-Resonant Modes in Josephson Junctions Exhibiting a Nonuniform Maximum Current Distribution”, Phys. Rev. B **17**, 2171 (1978).

[36] A. L. Rakhmanov, S. E. Savel’ev and F. Nori, ”Resonant electromagnetic emission from intrinsic Josephson-junctions stacks in a magnetic field”, Phy. Rev. B **79**, 184504 (2009).

[37] X. Hu and S.-Z. Lin, ”Three-dimensional phase-kink state in a thick stack of Josephson junctions and terahertz radiation,” Phys. Rev. B **78**, 134510 (2008).

[38] A. E. Koshelev, ”Alternating dynamic state self-generated by internal resonance in stacks of intrinsic Josephson junctions,” Phys. Rev. B **78**, 174509 (2008).

[39] S.-Z. Lin and X. Hu, ”Phase dynamics in intrinsic Josephson junctions and their electrodynamics,” Phys. Rev. B **79**, 104507 (2009).

[40] T. Koyama, H. Matsumoto, M. Machida and K. Kadowaki, ”In-phase electrodynamics and terahertz wave emission in extended intrinsic Josephson junctions,” Phys. Rev. B **79**, 104522 (2009).

[41] X. Hu and S.-Z. Lin, ”Cavity phenomena in mesas of cuprate high-Tc superconductors under voltage bias,” Phys. Rev. B **80**, 064516 (2009).

[42] M. Tsujimoto, K. Yamaki, K. Deguchi, T. Yamamoto, T. Kashiwagi,H. Minami, M. Tachiki, K. Kadowaki, and R. A. Klemm, ”Geometrical Resonance Conditions for THz Radiation from the Intrinsic Josephson Junctions in $Bi_2Sr_2CaCu_2O_{8+\delta}$,” Phys. Rev. Lett. **105**, 037005 (2010).

[43] H. B. Wang, S. Guénon, B. Gross, J. Yuan, Z. G. Jiang, Y. Y. Zhong, M. Grunzweig, A. Iishi, P. H. Wu, T. Hatano, D. Koelle, R. Kleiner, ”Hot Spots and Waves in $Bi_2Sr_2CaCu_2O_8$ Intrinsic Josephson Junction Stacks: A Study by Low Temperature Scanning Laser Microscopy,” Phys. Rev. Lett. **105**, 057002 (2010).

[44] M. Y. Li, J. Yuan, N. Kinev, J. Li, B. Gross, S. Guónon, A. Ishii, K. Hirata, T. Hatano, D. Koell, R. Kleiner, V. P. Kosheltes, H. Wang and P. H. Wu, ”Linewidth dependence of coherent terahertz emission from $Bi_2Sr_2CaCu_2O_8$ intrinsic Josephson junction stacks in the hot-spot regime,” Phys. Rev. B **86**, 060505 (2012).

[45] I. Kakeya, Y. Omukai, T. Yamomoto, K. Kadowaki and M. Suzuki, ”Effect of thermal inhomogeneity for terahertz radiation from intrinsic Josephson junction stacks of $Bi_2Sr_2CaCu_2O_{8+\delta}$,”Appl. Phys. Lett. **100**, 242603 (2012).

[46] M. Tsujimoto, H. Kambara, Y. Maeda, Y. Yoshika, Y. Nakagawa and I. Kakeya, ”Dynamic Control of Temperature Distributions in Stacks of Intrinsic Josephson Junctions in $Bi_2Sr_2CaCu_2O_8 + \delta$ for Intense Terahertz Radiation,” Phys. Rev. Appl. **2**, 044016 (2014).

[47] X. J. Zhou,J. Yuan, H. Wu, Z. S. Gao, M. Ji, D. Y. An,Y. Huang, F. Rudau, R. Wieland, B. Gross, N. Kinev, J. Li, A. Ishii, T. Hatano, V. P. Koshelets, D. Koelle, R. Kleiner, H. B. Wang and P. H. Wu, ”Tuning the Terahertz Emission Power of an Intrinsic Josephson-Junction Stack with a Focused Laser Beam”, Phys. Rev. Apl. **3**, 044012 (2015).

[48] F. Liu, S.-Z. Lin and X. Hu, ”Cavity phenomenon and terahertz radiation of a tall stack of intrinsic Josephson junctions wrapped by a dielectric material,” Supercond. Sci. Technol. 26, 025003 (2013).

[49] F. Liu and X. Hu, ”Possible ways to synchronize phase dynamics in intrinsic josephson junctions for terahertz radiation,” Int. J. Mod. Phys. B. (in press).

[50] F. Liu and X. Hu, ”Solution of Sine-Gordon Equations with Weak and Moderate Inductive Couplings under Bias Current and Dissipations” J. Phys. Soc. Jpn. 84, 064719 (2015).

[51] H. Kammerlingh Onnes, ”The Supercondctivity of Mercury,” Comm. Phys. Lab. Univ. Leiden, **122**, 124 (1911).

[52] W. Meissner and R. Ochsenfeld, ”Ein neuer Effekt bei Eintritt der Supraleitfähikeit,” Naturwissenschaften **21**, 787 (1933).

[53] P. F. Dahl, *Superconductivity: Its Historical Roots and Development from Mercury to the Ceramic Oxides* (American Instiute of Physics, New York, 1992).

[54] J. G. Bednorz and K. A. Müller, ”Possible High-Tc Superconductivity in the Ba-La-Cu-O System,” Zeitschrift Fur Physik B-Condensed Matter **64**, 189 (1986).

[55] M. K. Wu, J. R. Ashburn, C. J. Torng, P. H. Hor, R. L. Meng, L. Gao, Z. J. Huang, Y. Q. Wang, and C. W. Chu, ”Superconductivity at 93 K in a new mixed-phase Y-Ba-Cu-O compound system at ambient pressure,” Phys. Rev. Lett. **58**, 908 (1987)

[56] H. Maeda, Y. Tanaka, M. Fukututomi and T. Asano, ”New high-T_c superconductors without rare earth element,” Physica C **153**, 602 (1988).

[57] A. Schilling, M. Cantoni, J.D. Guo and H. R. Ott, ”Superconductivity above 130 K in the HgCBaCCaC-CuCO system,” Nature **363**, 56 (1993).

[58] F. Chen, Z. J. Huang, R. L. Meng, C. W. Chu, L. Gao and Y. Y. Xue, ”Superconductivity above 150 K in $HgBa_2Ca_2Cu_3O_8 + \delta$ at high pressures,” Nature **365**, 323 (1993).

[59] T. Muranaka Y. Zenitani J. Nagamatsu, N. Nakagawa and J. Akimitsu, ”Superconductivity at 39 K in magnesium diboride,” Nature **410**, 63 (2001).

[60] M. Hirano Y. Kamihara, T. Watanabe and Hosono, ”Iron-Based Layered Superconductor $La[O_{1-x}F_x]FeAs$ ($x = 0.05 - 0.12$) with $T_c = 26$ K,”J. Am. Chem. Soc. **130**, 3296 (2008).

[61] F. London and H. London, ”The Electromagnetic Equations of the supraconductor,” Proc. Roy. Soc. **A149**, 71 (1935).

[62] F. London, ”Macroscopical interpretation of superconductivity,” Proc. Roy. Soc. **152**, 24 (1935).

[63] V. L Ginzburg and L. D. Landau, Zh. Eksp. Teor. Fiz, **20**, 1064 (1950).

[64] L. N. Cooper, ”Bound electron pairs in a degnerate Fermi gas,” Phys. Rev. **104**, 1189 (1956).

[65] L. N. Cooper J. Bardenn and J. R. Schrieffer, ”Theory of Superconductivity,” Phys. Rev. **108**, 1175 (1957).

[66] L. P. Gor’kov, Zh. Eksperim. i Teor. Fiz **36**, 1918 (1959).

[67] S. Shapiro, S. Holly and A. R. Janus, ”Effect of Microwaves on Josephson Currents in Superconducting Tunneling,” Rev. Mod. Phys. **36**, 223 (1964).

[68] R. L. Kautz, ”Noise, chaos, and the Josephson voltage standard,” Rep. Prog. Phys. **59**, 935 (1996).

[69] V. Amebegaokar and A. Baratoff, ”Tunneling between Superconductors,” Phys. Rev. Letts. **10**, 486 (1963).

[70] A. I. Larkin and Ovchinni. Yn, Soviet Physics Jetp-Ussr **24**,1035 (1967).

[71] J. C. Swihart, ”Field Solution for a Thin-Film Superconducting Strip Transmission Line,” J. Appl. Phys. **32**, 461 (1961).

[72] I. O. Kulik, ”Theory of Resonance Phenomena in Superconducting Tunneling,” Sov. Phys. Tech. Phys-U **12**, 111 (1967).

[73] I. O. Kulik, ”Wave Propagation in a Josephson Tunnel Junction in Presence of Vortices and Electrodynamics of Weak Superconductivity,” Soviet Physics Jetp-Ussr **24**, 1307 (1967).

[74] A. C. Scott, Bull. ”Steady propagation of long Josephson junctions,” Am. Phys. Soc. **12**, 308 (1967).

[75] , M. D. Fiske, ”Temperature and Magnetic Field Dependences of Josephson Tunneling Current,” Rev. Mod. Phys. **36**, 211 (1964).

[76] I. K. Yanson, Svistuno. Vm, and Dmitrenk. Im, ”Experimental Observation of Tunnel Effect for Cooper Pairs with Emission of Photons,” Soviet Physics Jetp-Ussr **21**, 650 (1965).

[77] D. N. Langenberg, D. J. Scalapino, B. N. Taylor and R. E. Eck, ”Investigation of Microwave Radiation Emitted by Josephson Junctions,” Phys. Rev. Lett. **15**, 294 (1965).

[78] O. A. Levring, J. Mygind, N. F.Pedersen, O. H. Soerensen and M. Cirillo, ”Multisoliton Excitations in Long Josephson-Junctions,” Phys. Rev. Lett. **46**, 1299 (1981).

[79] R. Kleiner and P. Müller, ”Intrinsic Josephson effects in high-T_c superconductors,” Phys. Rev. B **49**, 1327 (1994)

[80] K. Delfanazari, H. Asai, M. Tsujimoto, T. Kwashiwagi, T. Kitamura, T. Yamamoto. M. Sawamura, K. Ishida, M. Tachiki, R. A. Klemm T. Hattori, K. Kadowaki, ”Study of coherent and continuous terahertz wave emission in equilateral triangular mesas of superconducting $Bi_2Sr_2CaCu_2O_{8+\delta}$ intrinsic Josephson junctions” Physica C 491, 16 (2013)

[81] K. Delfananzari, H. Asai, M. Tsujimoto, T. Kashiwagi, T. Yamamoto, M. Sawamura, K. Ishida, C. Watanabe, S. Sekimoto, H. Minami, M.tachiki, R. A. Klemm, T. Hattori and K. Kadowaki, Opt. Exress **21**, 2171 (2013).

[82] W. E Lawrence and S. Doniach, ”Theory of layer-structure superconductors,” in Proc. 12th Int. Conf. Low Temp. Phys, E. Kanda, ed. (Kyoto, 1971), p. 361.

[83] R. Kleiner, ”2-Dimensional Resonant Modes in Stacked Josephson-Junctions,” Phys. Rev. B **50**, 6919 (1998).

[84] V. M Krasnov, ”Terahertz electromagnetic radiation from intrinsic Josephson junctions at zero magnetic field via breather-type self-oscillations,” Phys. Rev. B **83**, 174517 (2011).

[85] M. J Ablowitz, A. C. Newell and H. Segur, ”Method for Solving the Sine-Gordon Equation,” Phys. Rev. Lett. **30**, 1262 (1973).

[86] H. B. Wang, S. Guenon, J. Yuan, A. Iishi, S.arisawa, T. Hatano, T. Yamashita, D. Koelle and R. Kleiner, ”Hot Spots and Waves in $Bi_2Sr_2CaCu_2O_8$ Intrinsic Josephson Junction Stacks: A Study by Low Temperature Scanning Laser Microscopy,” Phys. Rev. Lett. **102**, 017006 (2009).

[87] V. M. Krasonov, ”Coherent flux-flow emission from stacked Josephson junctions: Nonlocal radiative boundary conditions and the role of geometrical resonances,” Phys. Rev. B **82**, 134524 (2010).

[88] J. D Jackson, *Classical Electrodynamics Third Edition* (Wiley, New York, 1998).

[89] W. L. Stutzman and G. A. Thiele, *Antenna Theory and Design* (Wiley, New York, 1998).

[90] M. Leone, IEEE Tansactions on Electromagnetic Compatibility **45**, 486 (2003).